SÉRIE III NÚMERO 15 MARÇO 2021

rpee

revista portuguesa de engenharia de estruturas

portuguese journal of ***structural engineering***

Diretor: José Manuel Catarino

http://rpee.lnec.pt/

número temático / *thematic issue*:

alkali aggregate reaction

ISSN: 2183-8488

LABORATÓRIO NACIONAL DE ENGENHARIA CIVIL

Associação Portuguesa de Engenharia de Estruturas

Grupo Português de Betão Estrutural

SOCIEDADE PORTUGUESA DE ENGENHARIA SÍSMICA

rpee
revista portuguesa de engenharia de estruturas

série III número 15 março 2021

Revista quadrimestral – gratuita Diretor: José Manuel Catarino

índice

Conteúdo sujeito a revisão por pares académicos

rpee
revista portuguesa de engenharia de estruturas

Diretor

José Manuel Catarino

Administração

José Manuel Catarino
(LNEC - Laboratório Nacional de Engenharia Civil)

João Almeida Fernandes
(APEE - Associação Portuguesa de Engenharia de Estruturas)

Eduardo Júlio
(GPBE - Grupo Português de Betão Estrutural)

João Azevedo
(SPES - Sociedade Portuguesa de Engenharia Sísmica)

Coordenação Científica

Humberto Varum
(FEUP - Faculdade de Engenharia da Universidade do Porto)

Luís Oliveira Santos
(LNEC - Laboratório Nacional de Engenharia Civil)

Direção Executiva: Sandra Neves
Secretariado: Marta Rodrigues
Design Gráfico: Helder David

Fotografia da Capa
Barragem de Pracana, no rio Ocreza
(Fotografia cedida pelo Departamento de Barragens de Betão do LNEC)

Proprietário

LABORATÓRIO NACIONAL DE ENGENHARIA CIVIL, I. P.
Departamento de Estruturas
Av. Brasil 101 | 1700-066 LISBOA
tel: (+351) 21 844 32 60 | fax: (+351) 21 844 30 25
rpee@lnec.pt | http://rpee.lnec.pt

Edição, redação e divulgação eletrónica

LNEC | Divisão de Divulgação Científica e Técnica
Av. Brasil 101 | 1700-066 LISBOA
NIPC: 501 389 660
tel: (+351) 21 844 36 95 | fax: (+351) 21 844 30 18
livraria@lnec.pt | www.lnec.pt

ISSN 2183-8488

nota prévia

Este número da série III da Revista Portuguesa de Engenharia de Estruturas (**rpee**) é dedicado ao tema das reações expansivas de origem interna do betão, divulgando um conjunto de artigos submetidos à "16th International Conference on Alkali-Aggregate Reaction in Concrete (ICAAR 2020-2022)", que irá ocorrer no Laboratório Nacional de Engenharia Civil (LNEC) em 2022, embora estivesse inicialmente prevista para 2020. Tal como aconteceu no número de julho de 2020, a conjuntura de pandemia conduziu à opção de divulgação antecipada na **rpee** de artigos científicos preparados para esta conferência. A Administração da **rpee** e a Comissão Organizadora do ICAAR 2020-2022 entenderam assim manter o acordo para dedicar o número de março de 2021 a este evento, o que também foi consentido pelos autores dos artigos que agora se publicam. A qualidade científica deste número temático é assegurada pela Coordenação Científica da rpee em articulação com as Comissões Organizadora e Científica do ICAAR 2020-2022, representadas por António Lopes Batista e Bruno Godart. Fica aqui expresso o reconhecimento da Administração da **rpee** pelo excelente trabalho por eles desenvolvido.

*This issue of series III of the Revista Portuguesa de Engenharia de Estruturas (***rpee***) is devoted to the theme of swelling reactions of internal origin in concrete, disclosing a set of papers submitted to the "16th International Conference on Alkali-Aggregate Reaction in Concrete (ICAAR 2020- 2022)", which will take place at the National Civil Engineering Laboratory (LNEC) in 2022, although initially scheduled for 2020. As in the July 2020 issue, the pandemic situation led to the option of early disclosure in* **rpee** *of scientific papers prepared for this conference. The* **rpee***'s Board of Directors and the Organizing Committee of ICAAR 2020-2022 have decided to maintain the agreement to dedicate the March 2021 issue to this event, also consented by the authors of the papers now being published. The scientific quality of this thematic issue is ensured by the Scientific Coordination of rpee in conjunction with the Organizing and Scientific Committees of ICAAR 2020-2022, represented by António Lopes Batista and Bruno Godart. Here we express the recognition of the* **rpee***'s Board of Directors for the excellent work developed by both.*

A administração da **rpee**
The Board of Directors
José Manuel Catarino (LNEC)
João Almeida Fernandes (APEE)
Eduardo Júlio (GPBE)
João Azevedo (SPES)

editorial

O décimo quinto número da série III da Revista Portuguesa de Engenharia de Estruturas é dedicado ao tema das reações expansivas de origem interna do betão, divulgando à comunidade técnica e científica um conjunto de trabalhos selecionados entre os submetidos à 16th International Conference on Alkali-Aggregate Reaction in Concrete (ICAAR 2020-2022). A realização da conferência, no Laboratório Nacional de Engenharia Civil (LNEC), estava prevista para junho de 2020, mas devido à crise pandémica de Covid-19 que tem assolado o mundo, a sua concretização presencial foi adiada para 2022. Contudo, os trabalhos submetidos e revistos, até 2020, tiveram publicação "online" em 2021.

As conferências ICAAR têm uma periodicidade quadrienal, visando reunir investigadores, académicos e profissionais de todo o mundo, para partilhar e discutir os conhecimentos, perspetivas, experiências e inovações, considerando as vertentes físicas, químicas e estruturais das reações expansivas do betão.

Os dez artigos apresentados foram selecionados pelas comissões organizadora e científica da ICAAR 2020-2022, tendo-se procurado que cobrissem um conjunto alargado de temas, para dar uma panorâmica atual da problemática associada às reações expansivas do betão e dos seus efeitos estruturais nas obras.

The fifteenth issue of series III of the Revista Portuguesa de Engenharia de Estruturas is devoted to the theme of swelling reactions of internal origin in concrete, disclosing to the technical and scientific community a set of papers selected from those submitted to the 16th International Conference on Alkali-Aggregate Reaction in Concrete (ICAAR 2020-2022). The conference was scheduled for June 2020 at the National Civil Engineering Laboratory (LNEC) but due to the Covid-19 pandemic crisis that has been plaguing the world, it was postponed to 2022 and maintained as a face-to-face event. However, it was decided to publish in 2021 the papers that were submitted and reviewed until 2020.

The ICAAR conferences are held every four years, gathering together researchers, academics and professionals from all over the world, to share and discuss knowledge, perspectives, experiences and innovations, considering the physical, chemical and structural aspects of the swelling reactions of concrete.

The ten papers presented were selected by the organizing and scientific committees of ICAAR 2020-2022, with an attempt being made to cover a wide range of topics, in order to give a current overview of the problems associated with the swelling reactions of concrete and their structural effects in the works.

António Lopes Batista
Bruno Godart

Coordenadores do número temático
Coordinators of the thematic issue
reações álcalis-agregado
alkali aggregate reaction

Prevention of ASR by use of low alkali OPC and silica fume. Field and lab studies from the Maridal culvert and the Storo bridge in Oslo, incl. assessment of residual expansion

Prevenção da RAS usando cimentos Portland de baixo teor de álcalis e sílica de fumo. Estudos em laboratório e em condições naturais para a Passagem Maridal e Ponte Storo, em Oslo, incluindo a avaliação da expansão residual

Bård M. Pedersen
Eva Rodum
Marit Haugen
Jan Lindgård

Abstract

In 1999, the Maridal concrete culvert was built in Oslo, Norway. Natural aggregates known to be moderately alkali reactive according to laboratory and field experience were used.

Field survey combined with microstructural analyses of drilled cores have confirmed that the use of OPC with relatively low alkali content (0.53 % Na_2O eq.) combined with addition of 5% silica fume have prevented development of ASR. By corresponding field survey and microstructural analyses, it has also been verified that a similar aggregate combination has caused ASR in the nearby Storo bridge which was built in 1994.

18 years of service is too short time to conclude whether the concrete composition used in the Maridal culvert has a potential to develop ASR or not. To assess the long-term potential of ASR, residual expansion testing was performed. The conclusion from this testing is that the potential for further reaction and expansion is limited.

Resumo

Em 1999 foi construída a passagem de betão Maridal, em Oslo, na Noruega. Foram usados na composição do betão agregados naturais, conhecidos por serem moderadamente reativos aos álcalis, de acordo com a experiência de laboratório e de campo.

Levantamentos de campo combinados com análises microestruturais em carotes extraídas confirmaram que o uso de cimentos Portland com teor de álcalis relativamente baixo (0,53% Na_2O eq.), combinada com a adição de 5% de sílica de fumo, preveniu o desenvolvimento da RAS. A partir de levantamentos de campo e de análises microestruturais, foi verificado que uma combinação semelhante de agregados originou a RAS na ponte Storo, próxima, construída em 1994.

Os 18 anos de vida são um período de tempo pequeno para concluir se a composição do betão da passagem Maridal tem potencial para desenvolver RAS. Para avaliar o potencial da RAS, a longo prazo, realizou-se o ensaio de expansão residual. A conclusão deste ensaio é que o potencial de reação e expansão é limitado.

Keywords: Alkali content / Cold water extraction / Preventive measures / Residual expansion

Palavras-chave: Teor de álcalis / Extração com água fria / Medidas preventivas / / Expansão residual

Bård M. Pedersen

Norwegian Public Roads Administration
Bergen, Norway
baard.pedersen@vegvesen.no

Eva Rodum

Norwegian Public Roads Administration
Trondheim, Norway
eva.rodum@vegvesen.no

Marit Haugen

SINTEF Community
Trondheim, Norway
marit.haugen@sintef.no

Jan Lindgård

SINTEF Community
Trondheim, Norway
jan.lindgard@sintef.no

PEDERSEN, B. [*et al.*] – Prevention of ASR by use of low alkali OPC and silica fume. Field and lab studies from the Maridal culvert and the Storo bridge in Oslo, incl. assessment of residual expansion. **Revista Portuguesa de Engenharia de Estruturas**. Ed. LNEC. Série III. n.º 15. ISSN 2183-8488. (março 2021) 7-14.

1 Introduction

In 1999, the Maridal concrete box culvert with a total length of 340 m was built as part of the Tåsen tunnel in Oslo, Norway. The construction of the concrete culvert was closely followed up as part of the IPACS-project on early age concrete crack prediction, funded by the Brite Eu-Ram III program. Hence, the concrete mixture, construction and development of early age cracks are well documented [1]. Natural aggregates from the Oslo area, known to be alkali reactive according to Norwegian ASR methods [2] (petrographic examinations, mortar bar test results and concrete prism test results) and field experience, were used. At the time of construction, the knowledge on ASR was established in Norway, and the concrete mix design was in accordance with the Norwegian ASR regulations [3], allowing the use of any alkali reactive aggregates in combination with OPC for alkali levels up to 3.0 kg/m^3 (Na_2O eq.). The cement used for the culvert was an OPC with a relatively low alkali content of 0.53% Na_2O eq., in combination with 5% silica fume.

Figure 1 Outer wall and top slab during construction of the Maridal culvert in Oslo, Norway [1]

Figure 2 The Storo bridge, southern side [4]

The nearby structure Storo bridge was renovated and enlarged in 1994. The new structural parts were cast by use of a concrete with similar aggregate composition as the Maridal culvert. The exact concrete composition including type of cement is not known for this structure. However, it has been substantiated through this study that the alkali content is significantly higher than in the Maridal culvert. In 2016 and 2017, both structures were visited and surveyed, and cores were sampled for microstructural and chemical analyses. For the Maridal culvert also residual expansion testing was carried out on some of the extracted cores. This paper describes the results and discusses the performance of the two structures.

2 Materials and mix design

2.1 The Maridal culvert built in 1999

The concrete mixture used for construction of the culvert is shown in Table 1. The concrete requirements were in accordance with the Norwegian Public Road Administration (NPRA) Handbook "General specifications 2. Standard specification texts for bridges and quays" [5], prescribing a water binder ratio ≤ 0.40 (calculated using an efficiency factor of 2 for silica fume), 3-5% silica fume and 5 ± 1.5% air content.

Table 1 Concrete mixture from the construction of the Maridal culvert [1]

Materials	Content kg/m³
Norcem Anleggsement, OPC CEM I 52.5 (0.53 Na_2O eq.)	350
Silica fume	18
Plasticizer, Sika BV 40	4.0
Super plasticizer, Sikament 92	3.0
Air entraining agent, Sika AER	0.7
Natural sand 0/8 mm (absorbed water: 1.3%)	953
Natural gravel 8/14 mm (absorbed water: 1.1%)	206
Natural gravel 14/24 mm (absorbed water: 1.1%)	658
Total effective water content	154.4
Effective water binder ratio, w/(c + 2s)	0.40
Aimed air content (%)	5.0

The alkali content (alkalis from cement, admixtures and silica fume) is approximately 2.1 kg/m³ (Na_2O eq.) and hence well below the general limit of 3.0 kg/m³ Na_2O eq. valid at the time of construction (note: in 2017, the general limit was lowered to 2.5 kg/m³). The level of preventive measures for this culvert was even "safer" than the requirements in the national guidelines due to addition of 5% silica fume.

Microstructural analyses have shown that the sand and the coarse gravel both originates from the same gravel pit. A petrographic description and evaluation of the aggregate is as follows:

- The aggregate (sand and coarse gravel) is dominated by gneiss/granite, feldspathic rocks, dark rocks included volcanic rocks and siltstone/silt-claystone/marl. Sandstone and quartzite occur in less amounts. Mylonite, rhyolite, hornfels and limestone with and without impurities are represented as well.
- The *alkali reactive* rock types identified in the aggregate are siltstone, silt-claystone, marl, sandstone, mylonite and rhyolite, while hornfels and limestone with impurities are identified as *possible alkali reactive* rocks. The content of alkali reactive and possible alkali reactive rocks in the aggregate is about 30-35%.

This aggregate, in particular the coarse fraction, is previously documented to cause moderate damages in structures when the alkali content is high enough [6]. The following results were obtained in accelerated mortar bar testing and concrete prism testing:

- Both the fine and coarse fraction of this aggregate was tested in the EU "PARTNER" project, labelled "N6" in [7]. The 52 weeks expansion from testing according to the Norwegian 38 °C concrete prism test [2] was 0.076, considerably higher than the critical limit of 0.040% [7].
- A mortar bar test (1N NaOH, 80 °C, [2]) resulted in an expansion of 0.18% after 14 days of exposure, well above the critical limit of 0.11% that applies for mixtures of fine and coarse aggregates [8].

2.2 The Storo bridge built in 1994

As is often the case for old structures, it has not been possible to verify the cement type, the origin of the aggregate and mix design that were used in this structure. It has been claimed by people being involved with the construction works that the Storo bridge was built using a concrete mixture being similar to the concrete mixture of the Maridal culvert. The concrete requirements were most likely equal to that of the Maridal culvert, with one exception: In 1994 there were no national ASR regulations and hence no requirements on preventive measures in the form of low alkali cements or use of silica fume, fly ash or slag. Based on this, we can assume the following specifications:

- Effective water binder ratio, w/(c + 2S): maximum 0.40
- Silica fume: 3-5 weight% of cement
- Air content: 5% (±1.5%)

Aggregates: Based on microstructural analyses of the cores it has been verified that the aggregate used in this structure is of "similar rock types and with similar reactivity" as the aggregate used in the Maridal culvert. It has, however, not been verified whether these two aggregates are from the exact same gravel pit or not.

Cement type: It is not known which cement type that was used, but based on information about the Norwegian cement market in 1994 it is most likely an ordinary Portland cement (CEM I), either similar to the cement used in the Maridal culvert (with a Na_2O eq. of 0.53%) or a high-alkali cement with Na_2O eq. in the order of 1.2%. To gain more information regarding the alkali content of this concrete, chemical analyses were carried out both on cores extracted from the Maridal culvert and the Storo bridge, see Section 2.3.

2.3 Examination of alkali content by use of Cold Water Extraction (CWE)

Chemical analyses by use of Cold Water Extraction (CWE), as described by Plusquellec et al. 2017 [9], were performed for concrete extracted both from the Maridal culvert and the Storo bridge to compare these. The results are summarized in Table2. The measured alkali content of the samples is assumed to represent the available alkali content of the pore solution at the time of extraction. Note that the alkali content from the Tåsen culvert is almost identical to the theoretical value calculated from the concrete mixture (2.1 kg/m^3 Na_2O eq.). It is not known how much of the measured alkalis that originates from the cement, normally only 50-70% of these alkalis will be available in the pore solution according to Plusquellec et al. 2017 [9], depending on the type of binder (the highest level of alkalis, i.e. 70%, is expected available for OPC). It is thus likely that alkalis released from the aggregates have contributed to the measured alkali content. However, since the aggregates are similar in these two concretes, we can still compare the results. It is therefore reasonable to assume that the total alkali content for the Storo bridge is in the order of 90% higher than for the Maridal concrete, i.e. approx. 4.0 kg/m^3 (Na_2O eq.). This further implies that the cement used was an OPC with an alkali content of approximately 1.1% (Na_2O eq.). Since the Storo bridge also has developed some ASR (see 3.2), some alkalis have most likely been absorbed in the ASR gel. The original alkali content of the Storo bridge concrete is thus assumed to be a little higher than 4.0 kg/m^3 (Na_2O eq.).

Table 2 Measurement of alkali contents by the CWE-method. Mean values of four samples from two cores (Maridal) and two samples from one core (Storo) [10]

Structure	[Na] pore solution, mol/l	[K] pore solution, mol/l	Alkali content of the sample, kg/m^3, Na_2O eq.
Maridal culvert	0.34	0.30	2.3
Storo bridge	0.55	0.65	4.2

Based on the results and discussions in Sections 2.2 and 2.3 the following has been substantiated: The concrete used in the Storo bridge is rather similar to the concrete used in the Maridal culvert, with one important exception: The cement used in the Storo bridge had a significantly higher alkali content compared to the cement used in the Maridal culvert.

3 Field and microstructural evaluation of structures

3.1 The Maridal culvert after 18 years of service

3.1.1 Field survey

In June 2017, the Maridal culvert was visited and surveyed, and six cores were drilled from four different sections of the culvert. Typical crack patterns caused by early age hydration heat effects in a wall-on-slab structure are shown in Figures 3 and 4. Vertical cracks in the wall are caused by external restraint from the slab during the cooling phase of the wall. Cracks with crazing pattern (Figure 4) are caused by temperature gradients over the cross section of the (warm) wall shortly after demolding. Drying shrinkage may also produce (or further develop) the crazing, as can ASR if present. The crack widths varied from very fine cracks 0.03 mm up to 0.45 mm. These examples are typical for the initial state of cracking of a new structure, just a week or two after casting. The origin is cement hydration and subsequent heat generation.

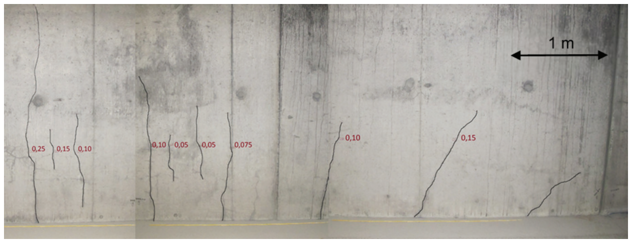

Figure 3 Visual assessment of wall in the Maridal culvert, right half of section 42. Main cracks intensified on the photo, crack widths (in mm) are drawn on the photo [11]

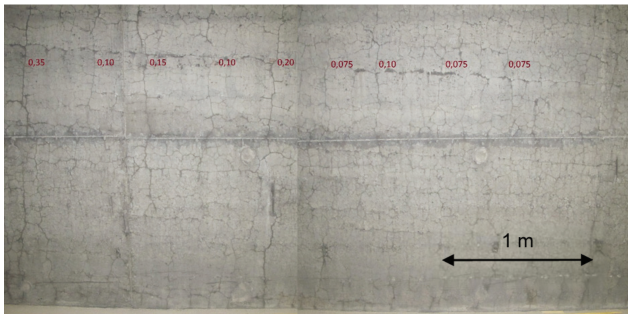

Figure 4 Visual assessment of wall in the Maridal culvert, part of section 38. Crack widths (in mm) are drawn on the photo [11]

3.1.2 Microstructural analyses

Visual examinations of the six drilled cores showed no signs of ASR. For one of the cores from section 42 further analyses were performed; microstructural analysis of one fluorescence impregnated plane polished section prepared from one half-core (after sawing one core into two parts) and of one thin section prepared from the other half-core. Two photos of the plane polished section, in ordinary and UV light, respectively, are shown in Figure 5, while two photos of the thin section are shown in Figure 6.

The results from the microstructural analyses can be summarized as follows [10]:

- Plane polished section (Figure 5): Some cracks in the cement paste, a few cracks in aggregates and very few cracks running from aggregates into the cement paste. No appreciable signs of ASR.

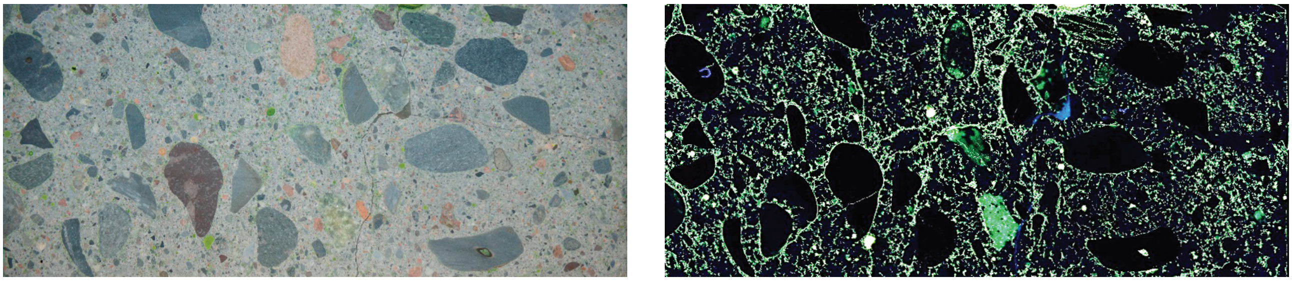

Figure 5 Plane polished section from wall section 42, in ordinary and UV-light. The length of the section is 200 mm, surface to the right. Comment: The core was drilled through a crack starting at the surface (crack width 0.25 mm), then turning parallel to the surface in a depth of about 80 mm. Due to this cracking, the outer part of the core was broken during the drilling process. The core was thus glued before preparing the polished section, with a non-fluorescence epoxy. These cracks can therefore only be observed in the left picture (but not in the right picture). [10]

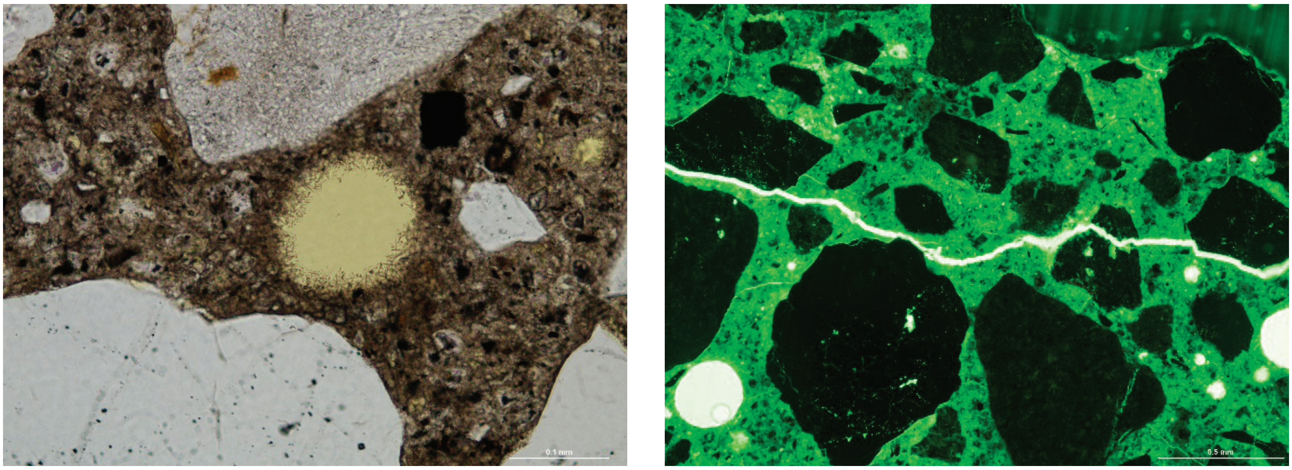

Figure 6 Thin section details. No signs of ASR were observed. Left: Ettringite in a small air void. Right: Crack in the cement paste. [10]

- Thin section (Figure 6): Some micro-cracking, no coarse cracks. Some ettringite and a few particles of undispersed silica fume were observed. No signs of ASR.

3.2 The Storo bridge after 22 years of service

3.2.1 Field survey

Parts of the Storo bridge in Oslo was built in 1994, including the railing structure. Due to suspected progressing ASR, this structure was visually examined in October 2016, and three cores were drilled. As can be seen in Figure 7 the surface cracking of the railing appears as crazing or map cracking. The crack widths varied between 0.03 and 0.15 mm. The cracking indexes, defined as "summarized crack widths along a line divided by the length" [4], varied between 0.041 and 0.062% for the different fields of the bridge railing. The calculated indexes were evaluated to be of low degradation grade according to a classification system developed within a Norwegian research project [12]. No significant differences between horizontal versus vertical lines were found.

Figure 7 Visual assessment of the railing of Storo bridge, phase to the north [4]

3.2.2 Microstructural analyses

By visual examination of the cores, two of the three cores showed signs of ASR. For one of the cores further analyses were performed; microstructural analysis of one fluorescens impregnated plane polished section prepared from one half-core and of one thin section prepared from the other half-core. Two photos of the plane polished section, in ordinary and UV light, respectively, are shown in Figure 8, while two photos of two thin sections are shown in Figure 9. The conclusions of the analyses can be summarized as follows [10]:

- Plane polished section (Figure 8): Cracks in some aggregate particles, some cracks running from the aggregate into the cement paste. A white precipitation product found in some air pores.
- Thin section (Figure 9): Many micro-cracks and fine cracks. Alkali-silica gel observed in several air pores and in cracks, both in the aggregate particles and in the cement paste. ASR has led to internal cracking of the concrete.

3.3 Conclusions based on field and microstructural examination

Based on the presented field survey and laboratory results (microstructural analyses in plane polished sections and thin sections) there are obviously differences in performance for the two structures: The Storo bridge built using an OPC with an alkali content of approximately 1.2% (Na_2O eq.) + 3-5% silica fume (assumed binder composition) shows clear signs of ASR after 22 years of service. On the other hand, the Maridal culvert built using an OPC with a much lower alkali content of 0.53% (Na_2O eq.) + 3-5% silica fume (known binder composition) shows no appreciable signs of ASR after 18 years of service. Both structures have cracks in field that look "suspicious". However, the cracks on the Maridal culvert were primarily developed at a very early age [1]. It should also be noted that the cores from the Maridal culvert was taken from the inner side of the culvert not exposed to direct rainfall, while the cores taken from the Storo bridge is from the railing directly exposed to rainfall.

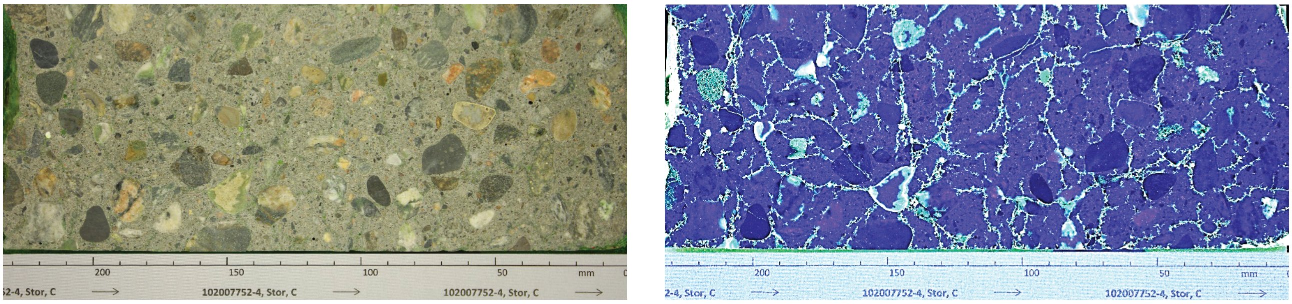

Figure 8 Plane polished section from Storo bridge, in ordinary and UV-light. The length of the section is 230 mm, surface to the right [10]

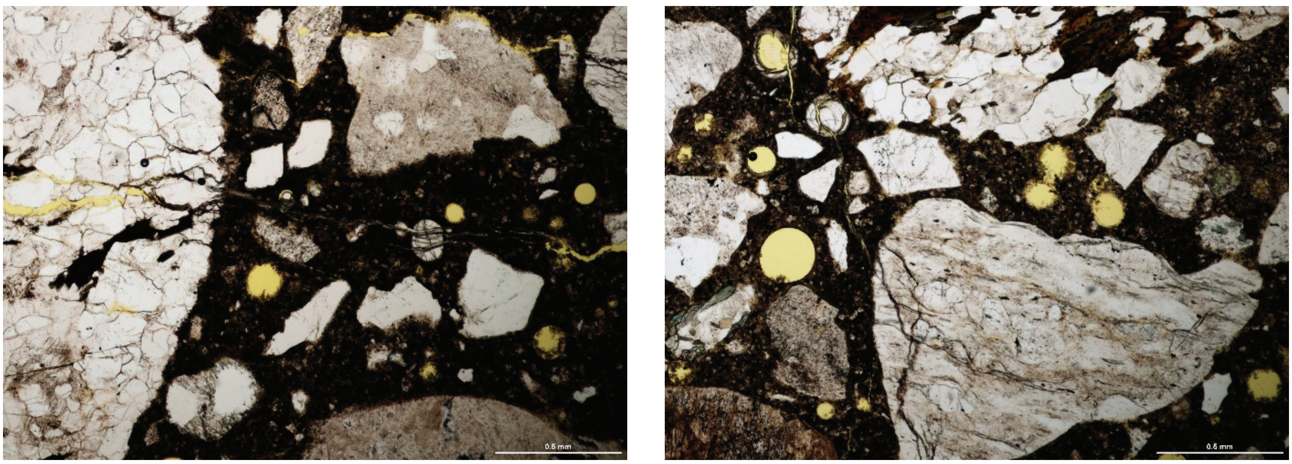

Figure 9 Thin section details. Left: Alkali-silica-gel in a crack running from a quartz-rich rock. Air void in crack filled with alkali-silica gel. Right: Alkali-silica gel in a crack running from a mylonite rock. Air void in crack filled with alkali-silica gel [10]

4 Accelerated residual expansion testing

4.1 Concrete from the Maridal culvert

18 years of service is a bit short time to conclude whether the concrete from the Maridal culvert has a potential to cause harmful ASR or not in the long run. To test the potential of ASR, residual expansion testing by the Canadian "UNB-CCT" method [13] on three cores (∅94 mm × 300 mm) was initiated in April 2018. In this method, the cores stored in sealed containers at 38 ºC, are "surrounded" by a "thin layer" of an alkaline solution simulating the pore water solution. The alkali concentration (Na and K) of this alkaline solution was calculated based on chemical analysis of extracted concrete by use of the CWE method described by Plusquellec et al. 2017 [9]. Ideally, this should result in a situation where the alkalinity of the pore water is in equilibrium with the liquid layer surrounding the specimens.

Expansion results up to 128 weeks of exposure are shown in Figure 10. As can be seen in the Figure, the specimens are expanding slowly at 38 ºC before levelling off after two years of exposure.

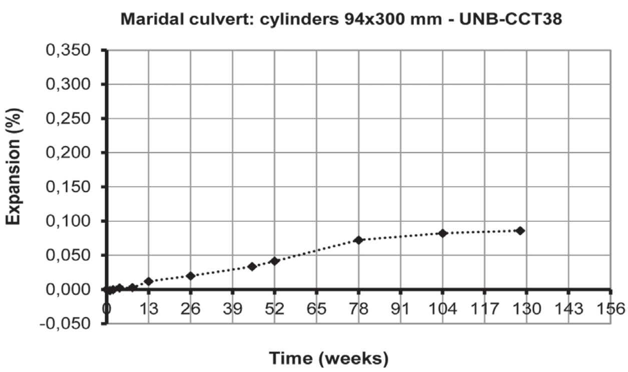

Figure 10 Residual expansion testing by the Canadian UNB-CCT test method. Mean values of three samples [12]

So, what can we learn from this plot? Should we expect that the concrete would react and expand in the long run or not? When exposed to 38 ºC and 100% RH there is obviously some potential for reaction. The expansion level at 52 weeks is above the border of the 0.030% limit given by the Norwegian regulations when running performance testing by use of the concrete prism test method [8]. However, the residual expansion test method is "more aggressive" than the CPT-method since there is no leaching of alkalis (or more likely a slight ingress of alkalis from the solution surrounding the sample). The results shown in Figure 10 have been compared with residual expansion results from another bridge with a more reactive concrete composition, see Section 4.2.

4.2 Comparison with the Nautesund bridge

The Nautesund bridge was built in 1959 and demolished in 2009, partly due to ASR. In connection to the demolition, a comprehensive R&D project was carried out, described in [14, 15]. Among other topics this included reconstruction of the concrete mixture (alkali content and aggregate type), residual expansion testing of extracted concrete from the bridge as well as concrete prism testing of freshly cast reconstructed concrete. Reconstruction of the old concrete was carried out according to the following procedure: a) separation of aggregate from concrete by use of liquid nitrogen and microwave, b) splitting into < 4 mm and > 8 mm fractions by sieving, c) petrographic analysis and identification of the aggregate origin and d) estimation of cement content by use of TGA. Concrete structures built up to 1990 was mainly built using ordinary Portland cement from the national cement supplier Norcem, and the alkali content can be estimated based on historical data from Norcem. A more detailed description of the reconstruction methodology can be found in [10, 15].

The alkali contribution from the OPC being used has been estimated to be between 4.8 and 5.3 kg/m^3 (Na_2O eq.) [15]. The separated aggregate (sand and coarse aggregate) is consistent with the aggregate found in a local pit close to the bridge. It is dominated by quartzite, gneiss/granite and metarhyolite, while dark rocks incl. volcanic rock, quartz rich rock, feldspathic rock, quartzite and metasandstone occur in less amounts. The alkali reactive rock types identified are metarhyolite and metasandstone, while quartzite and quartz rich rock are identified as possible alkali reactive rocks. The content of alkali reactive and possible reactive rocks is about 35%, i.e. at the same level as the aggregate used in the Storo bridge and the Maridal culvert [15].

Two freshly cast reconstructed concretes with OPC ("Mix 1" with 4.8 kg/m^3 (Na_2O eq.) and "Mix 2" with 5.3 kg/m^3 (Na_2O eq.)) and aggregates collected from the local pit used to cast the bridge, were tested according to the Norwegian CPT method (100 × 100 × 450 mm^3 prisms at 38 °C/100%RH) [2]. Testing of residual expansion of the original bridge concrete was performed by two 38°C CPT methods; 1) the Canadian "UNB-CCT" method with alkaline solution (as described in 4.1) and 2) the Norwegian CPT (samples stored on grids above water, labelled "100% RH") [2]. The latter included two series of specimens, i.e. sawn prisms (100 × 100 × 450 mm^3) and cored cylinders (∅145 mm × 300 mm). Some relevant results are plotted in Figure 11.

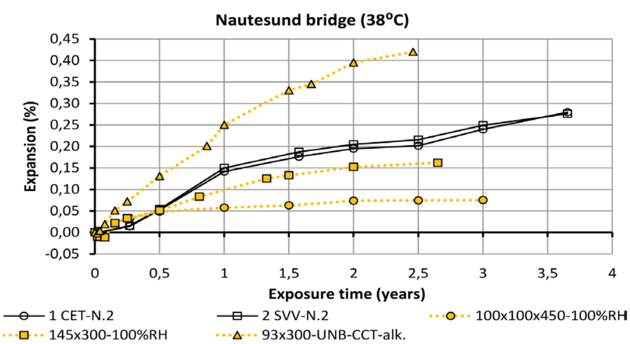

Figure 11 Test results from the Nautesund bridge, all samples exposed to 38 ºC. Black lines show results from accelerated testing of freshly cast reconstructed concretes, yellow dotted lines show results from residual expansion testing [12]

As seen from Figure 11, the accelerated residual expansion of the Canadian "UNB-CCT" cylinders (labelled "93 × 300-UNB-CCT-alk.") is 0.25% at 1 year and still increasing. Accelerated residual expansion of sawn 100 mm prisms (labelled "100 × 100 × 450-100%RH") and ø145 mm drilled cylinders (labelled "145 × 300-100%RH"), tested according to the Norwegian CPT-method, show significantly lower expansion levels at all ages. The sawn prisms (with highest area/volume-ratio) is levelling off after six months of exposure at a relatively low expansion level, most likely due to lack of alkalis caused by leaching combined with further consumption of alkalis by the ASR-gel developed during the testing. The expansion potential for the freshly cast reconstructed concrete (100 mm prisms labelled "Mix 1" and "Mix2") is significantly higher than the residual expansion of sawn prisms of original concrete (of same prism size), but much lower than the results of the "UNB-CCT" residual method with possibility of external alkali supply. The ø145 mm drilled cylinders are still expanding after two years of exposure but are tending to level off after 1-1.5 years of exposure.

It is interesting to note that the freshly cast reconstructed concretes and the two residual expansion test series, all exposed to 100% RH, obtain equal expansion (0.05%) after six months of exposure. After this point in time, the access to alkalis in the concrete pore water is controlling the further ASR expansion. Since the field concrete already (during 50 years of service) had developed ASR at the time of drilling, the "starting" alkali level in the pore water is lower (due to consumption of alkalis by the ASR-gel) compared with the freshly cast concrete. This is assumed to be the main cause for the earlier levelling off for the field concrete samples.

The comparison has shown that the "UNB-CCT" method, used for the Maridal culvert, most likely is somewhat "conservative". Hence, the probability for development of harmful ASR in the Maridal culvert is relatively low. Even though there might be a potential for long-term damages, it will be an extremely slow process due to the climatic conditions. The yearly average mean temperature in Oslo is only 7 ºC (with monthly average variations from -4 ºC to 18 ºC) and the average relative humidity (RH) is 74%. The access to rainfall / water is also limited in the Maridal culvert.

5 Conclusions

Investigations of the Maridal culvert after 18 years of service have shown that the combination of relatively low alkali content and 5% silica fume has prevented ASR, while a 90% higher alkali content as exemplified for the otherwise similar concrete in the Storo bridge has caused ASR. There are some uncertainties regarding the time factor for the Maridal culvert, since the age was only 18 years at the time of the investigation (i.e. one cannot conclude that ASR will not develop in the future). Therefore, accelerated residual expansion measurements have been performed. The results indicate that the potential for future harmful ASR is limited.

Acknowledgement

The authors gratefully acknowledge the financial support from the Norwegian Public Roads Administration and the Norwegian research project 236661 "Alkali-silica reaction in concrete – reliable concept for performance testing" (mainly funded by the Norwegian Research Council).

References

[1] Heimdal, E.; Kanstad, T.; Kompen, R. (2001) – Maridal culvert, Norway. Field test I. IPACS Report BE96-3843/2001:73-7.

[2] Norwegian Concrete Association, NB32, (2005) – Alkali aggregate reactions in concrete. Test methods and requirements to laboratories. NB publ. No. 32. Oslo (in Norwegian).

[3] Norwegian Concrete Association, NB, (1996) – Durable concrete with alkali reactive aggregates. NB publ. No. 21. Oslo (in Norwegian).

[4] Rodum, E. (2016) – Inspection of the Storo bridge. Internal memo, Norwegian Public Roads Administration (in Norwegian).

[5] Norwegian Public Roads Administration (1988) – Handbook 026: General Specifications 2. Standard specifications text for bridges and quays (in Norwegian).

[6] Lindgård, J.; Wigum, B.J. (2003) – Alkali aggregate reaction in concrete – field experiences. SINTEF report no. STF22 A02616, Trondheim, Norway. 127 p + appendices (in Norwegian).

[7] Lindgård, J.; Nixon, P.J.; Borchers, I.; Schouenborg, B.; Wigum, B.J.; Haugen, M.; Åkeson, U. (2010) – The EU "PARTNER" project – European standard tests to prevent alkali reactions in aggregates: Final results and recommendations. Cement and Concrete Research, Vol 40, pp 611-635.

[8] Norwegian Concrete Association, NB, (2017) – Durable concrete with alkali reactive aggregates. NB publ. No. 21. Oslo (in Norwegian).

[9] Plusquellec, G.; Geiker, M.R.; Lindgård, J.; Duchesne, J.; Fournier, B.; De Weerdt, K. (2017) – Determination of the pH and the free alkali metal content in the pore solution of concrete: Review and experimental comparison. Cement and Concrete Research, Vol 96, pp. 13-26.

[10] Lindgård, J.; Rodum, E. (2018) – KPN-ASR – Test report 2. SINTEF report 2018:00084-Restricted.

[11] Rodum, E. (2017) – Inspection of the Maridal culvert. Internal memo, Norwegian Public Roads Administration (in Norwegian).

[12] Lindgård, J.; Rodum, E.; Fournier, B. (2019) – KPN-ASR – Test report 3. SINTEF report 2019:00741-Restricted.

[13] Moffat, T. (2017) – Personal communication with Ted Moffatt at University of New Brunswick.

[14] Rodum, E.; Stemland, H. (2014) – Alkali-Silica reaction: Investigations of the Nautesund bridge after 50 years. Field and laboratory examinations and loading of large reinforced elements. Norwegian Public Roads Administration Report no. 309 (in Norwegian).

[15] Rodum, E.; Lindgård, J.; Skjølsvold, O. (2015) – Testing of materials from the Nautesund bridge: R&D Program Durable structures 2012-2015, Norwegian Public Roads Administration Report no. 469 (in Norwegian).

Experimental study of the effects of mechanical restraints on ASR expansions in concrete

Estudo experimental dos efeitos das restrições mecânicas nas expansões do betão devidas à RAS

Joaquín Liaudat
Carlos M. López
Ignacio Carol

Abstract

This paper summarizes an experimental campaign devoted to the study of the effect of (internal and external) mechanical restraints on Alkali-Silica Reaction (ASR) expansions in concrete made with soda-lime (SL) glass as reactive aggregate. The campaign included the development of two new experimental setups. The first setup made it possible to measure ASR expansion curves at the level of a single interface between a reactive aggregate and a cementitious matrix. For this purpose, small sandwich-like specimens, with cement paste or mortar on top and bottom of a disc of SL glass in the middle, were used. For the second experimental setup, a true-triaxial machine was used to obtain ASR expansion curves of concrete cubical specimens subjected to three different triaxial stress states. Based on the results obtained, a reaction-expansion mechanism is proposed that might explain the effects of the stress state on the ASR expansions of concrete.

Resumo

Este artigo resume uma campanha experimental dedicada ao estudo dos efeitos das restrições mecânicas (internas e externas) nas expansões devidas à reação álcalis-sílica (RAS) num betão fabricado com vidro comum (SL) como agregado reativo. A campanha incluiu o desenvolvimento de duas novas configurações experimentais. A primeira configuração possibilitou a medição das curvas de expansão devidas à RAS ao nível de uma única interface entre o agregado reativo e a matriz cimentícia. Para tal foram utilizados pequenos provetes do tipo sanduíche, com a pasta de cimento ou a argamassa na parte superior e inferior de um disco de vidro SL intercalado. Na segunda configuração experimental, foi usada uma máquina triaxial para obter as curvas de expansão devidas à RAS em provetes cúbicos de betão submetidos a três diferentes estados de tensão triaxial. Com base nos resultados obtidos, propõe-se um mecanismo de reação-expansão que pode explicar os efeitos do estado de tensão nas expansões do betão devidas à RAS.

Keywords: Concrete / ASR / Stress state / Glass / Interface

Palavras-chave: Betão / RAS / Estado de tensão / vidro / Interface

Joaquín Liaudat

School of Civil Engineering of Barcelona (ETSECCPB)
Universitat Politècnica de Catalunya (UPC)
Spain
joaquin.liaudat@upc.edu

Carlos M. López

School of Civil Engineering of Barcelona (ETSECCPB)
Universitat Politècnica de Catalunya (UPC)
Spain
carlos.maria.lopez@upc.edu

Ignacio Carol

School of Civil Engineering of Barcelona (ETSECCPB)
Universitat Politècnica de Catalunya (UPC)
Spain
ignacio.carol@upc.edu

LIAUDAT, J. [*et al*.] – Experimental study of the effects of mechanical restraints on ASR expansions in concrete. **Revista Portuguesa de Engenharia de Estruturas**. Ed. LNEC. Série III. n.º 15. ISSN 2183-8488. (março 2021) 15-24.

1 Introduction

Alkali-Silica Reaction (ASR) can be described as a particular type of chemical reaction in concrete involving the alkaline pore solution of the Hydrated Cement Paste (HCP) and various metastable forms of silica present in many natural and synthetic aggregate particles used in concrete [1, 2]. The silica structure is dissolved by the attack of hydroxyl anions, passing to the pore solution in aqueous forms which later recombine with calcium and alkali cations (always present in concrete pore solution) to form silicate hydrates of variable stoichiometric composition, the so-called 'ASR gel'. This reaction product is usually hygroscopic and swells as it absorbs water. The degree of hygroscopy and the associated volume change of the ASR gel depends mainly on its chemical composition and the Relative Humidity (RH) in the concrete pores. If the space available at the reaction site, i.e. pores, cracks, etc., is not enough to allocate the ASR gel, the 'swelling pressures produced by the gel induce the formation of microcracks close to the reaction sites, and these propagate and coalesce to produce cracking within the fabric of the concrete and overall expansion of the structural element affected' [3]. Since ASR was first identified in the late 1930s by T.E. Stanton [4, 5], extensive knowledge has been accumulated 'regarding the mechanisms of the reactions, the aggregate constituents that may react deleteriously, and precautions that can be taken to avoid resulting distress' [6]. However, the ASR expansion of concrete is a complex phenomenon and some aspects of it are still a matter of controversy. One of these aspects is the influence of the stress state of concrete on the development of the ASR expansions, as well as the underlying mechanisms that determine this influence.

Since the early investigations, it was noticed that the stress state has an influence on the kinetics and distribution of ASR-induced cracking and expansions [7]. However, it was not until recent years that this topic became of particular interest for researchers and practitioners. This interest is motivated by the need of introducing the effect of the stress state in the numerical models used for the prediction of the evolution of the serviceability and strength of ASR-affected concrete structures. In the last 20 years a number of experimental studies on the effect of the stress state on ASR concrete expansions have been published [e.g. 8-13], but, nevertheless, the nature and magnitude of these effects, as well as the basic mechanisms behind them, have not been totally clarified.

In this context, a combined experimental-numerical study has been undertaken with the purpose of deepening in the understanding of the mechanisms by which the stress state affects the development of ASR concrete expansions. For the experimental part of the study, two new experimental setups have been developed and used in an extensive experimental campaign. The first one for studying ASR expansions at the level of a single aggregate-cementitious matrix (HCP or mortar) interface, and the second one for studying ASR expansions of concrete specimens under triaxial stress states. Based on the results obtained in the experimental study, as well as on published results from other authors, a reaction-expansion mechanism that may explain the effects of concrete stress state on ASR expansions is proposed. This paper focuses on this part of the study, summarizing the methodology and the results of the experimental campaign, which are more extensively described elsewhere [14-16].

In the second part of the study (not discussed here), the proposed reaction-expansion mechanism has been theoretically formulated and implemented in a coupled Chemo-Mechanical (C-M) Finite Element model, which has been used to demonstrate the ability of the proposed reaction-expansion mechanism to qualitative and/or qualitatively reproduce the experimental observations [14, 17].

2 ASR interfacial expansion tests

The aim of this test is to study ASR expansions at the level of single interface between a cementitious matrix and a reactive aggregate due to the formation of reaction products. Two types of cylindrical specimens of 33 mm diameter and 66 mm height are used. The first type, called 'reactive specimens' consists in sandwich-like specimens with a disc of reactive aggregate in the middle and cementitious matrix on top and bottom of it (Figur 1). The second type, called 'control specimens', consists in purely cementitious matrix specimens, without reactive aggregate. Steel gauge inserts are embedded at both ends of the specimens for measuring the length changes. The control specimens are used to evaluate the deformation of the cementitious matrix due to phenomena such as drying shrinkage or thermal expansions.

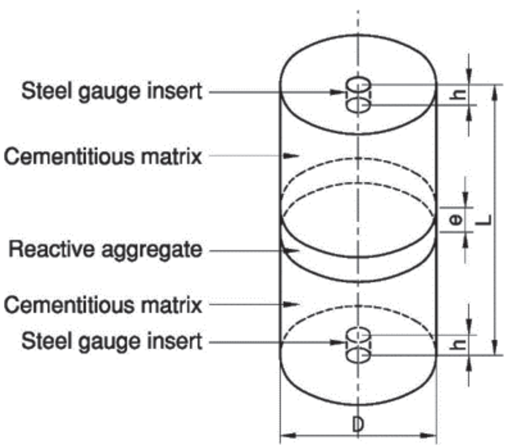

Figure 1 Scheme of a reactive specimen. Dimensions (in mm): D = 33, L = 66, h = 5, e = 6

The day after casting, the specimens are unmoulded and cured in airtight container with an alkaline solution at room temperature for 27 days. Then, the containers are heated in an oven at 60 ºC and kept at this temperature until the end of the test. During both stages, length changes of the specimens are measured regularly.

From the length change measurements of the active and the control specimens, the ASR expansion curves corresponding to a single matrix-aggregate interface are obtained using Equation (1), where L and ΔL are the length and the length change of the reactive specimen, respectively, e is the width of the reactive aggregate disc, h is the length of the steel gauge insert, $\overline{\varepsilon}$ is the average deformation of the control specimens, α_{agg} and α_{steel} are the thermal expansion coefficients of the aggregate and of the gauge insert steel, respectively, ΔT is the temperature variation from curing to exposure conditions, and d_I is the expansion at a single interface. For further details of the test method refer to [14, 16].

$$2d_I = \Delta L - \overline{\varepsilon}\left(L - 2h - e\right) - \left(e\alpha_{agg} + 2h\alpha_{steel}\right)\Delta T \quad (1)$$

A typical set of interfacial expansion curves corresponding to specimens made soda-lime (SL) glass as reactive aggregate and mortar with siliceous sand as cementitious matrix is shown in Figure 2. When the curing stage is finished and the temperature is increased to 60 ºC, the specimens start to expand due to the formation of ASR products at the interfaces.

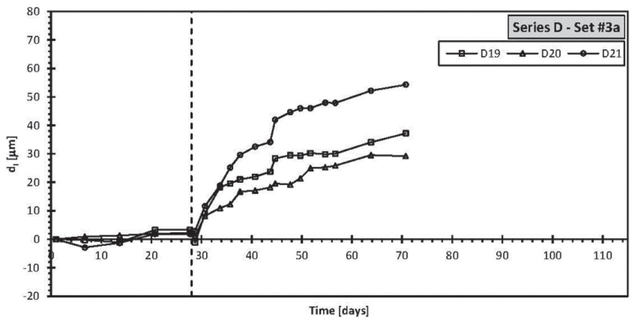

Figure 2 Interfacial expansion curves corresponding to specimens made with SL glass as reactive aggregate disc and mortar with siliceous sand as cementitious matrix. The dashed line indicates the end of curing stage (room temperature) and the beginning of exposure stage (60 ºC)

The reaction products at the interface are studied by means of SEM images and EDS microanalyses of polished sections of the specimens. For example, Figure 3 shows a set of images of the interfacial zone of a SL glass-cement paste specimen tested in the above-described conditions. In the left image, one can distinguish the glass at the upper part, the cement paste at the bottom part, and a layer in between which corresponds to reaction products. Note that the reaction products themselves are only visible at the limits of this layer, just besides the glass and the cement paste. The rest of the layer appears plain black due to the epoxy resin used in the preparation of the sample, which replace the reaction products that had been there but were lost in the cutting and polishing processes. The upper and bottom-right images, show in detail the different morphology of the reaction products located next to the glass and the cement paste, respectively. The normalized chemical composition of these reaction products obtained via EDS microanalyses is within the following ranges: Ca/Si = 1.00-1.50, (Na + K)/Si = 0.10-0.80.

In [14], additional results obtained with different cementitious matrices, reactive aggregates, and exposure conditions can be found, as well as detailed discussions of the effect of these factors. These results seem to indicate that:

- The ASR products formed in between SL glass and cement paste or mortar have relatively high calcium contents (molar Ca/Si = 1.0-1.5).

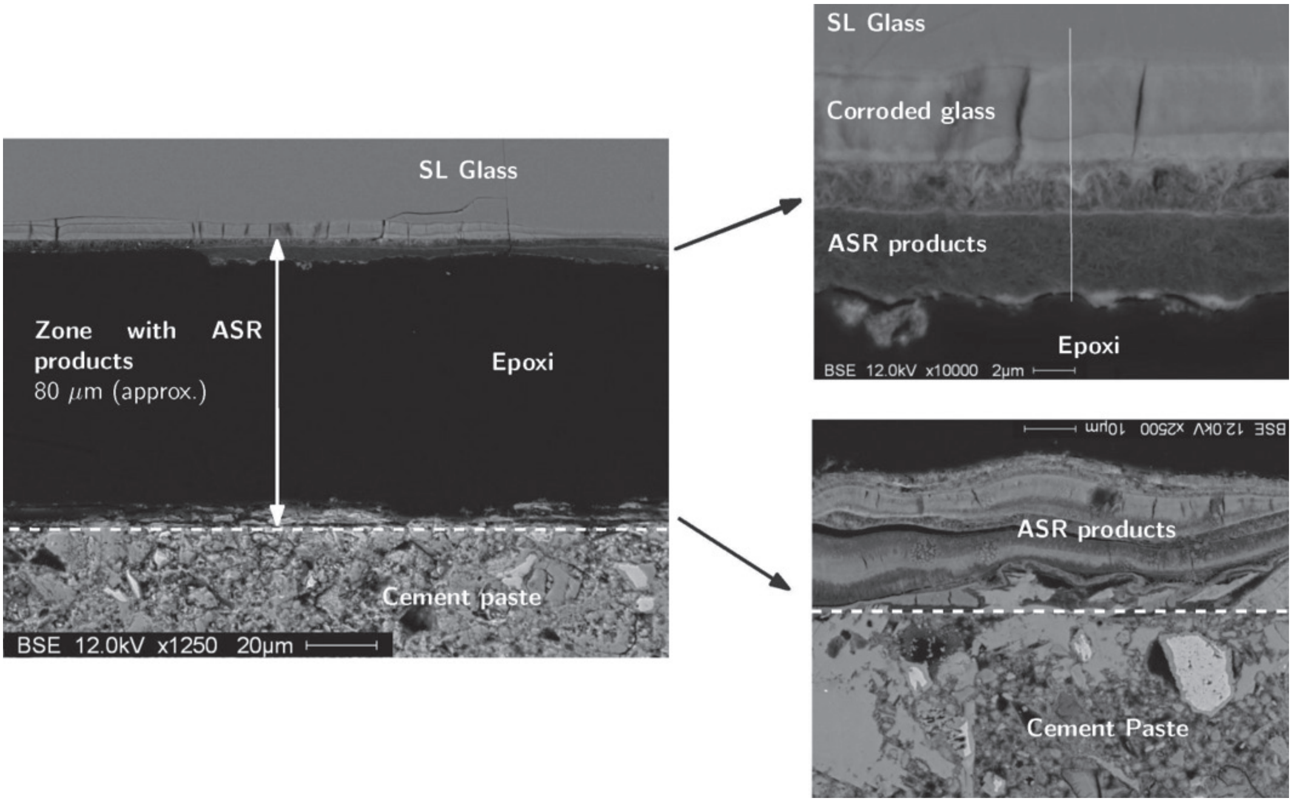

Figure 3 SEM images from the reacted zone interfacial zone of a specimen made with SL glass as reactive aggregate and cement paste as cementitious matrix [16]

- The mass exchange of alkali and/or water between the specimens and the alkaline bath determines the kinetics of the interfacial expansions.
- The interfacial expansions are limited by the separation of the reactive aggregate (SL glass of Borosilicate glass) disc from the cementitious matrix occurring for interfacial expansions ranging between 30 μm and 50 μm.
- The type of cementitious matrix has an influence on the interfacial expansion rates. The fastest expansions were measured on specimens with matrix made of cement and Micro Silica (MS) paste, followed by the specimens made with plain cement paste, and the specimens made with mortar, in this order.

3 ASR confined expansion tests

The aim of this test is to measure ASR expansions in cubic concrete specimens under true triaxial confinement, i.e. under different constant stress in each principal direction. With this purpose, a testing machine, named 'Alkali-Aggregate Reaction Triaxial Machine' (AARTM), was originally designed and constructed by Prof. V.E. Saouma at University of Colorado-Boulder. The machine was later transferred to UPC (Barcelona), where a number of modification were introduced by the authors to the original design. See Figure 4 for general and detail views of the AARTM.

The AARTM consists of a triaxial loading frame which can apply up to 9 MPa compression stress on each axis of a 150x150x150 mm cubical specimen. In contrast with other testing setups with triaxial confinement proposed in the literature [12, 18], the AARTM has the advantage of being capable of applying quasi-uniform constant true-triaxial stress states. The deformation of the specimen is measured with three displacement sensors (LVDTs) per axis, attached to the loading plates. The AARTM is capable of raising and maintaining the specimen temperature at a pre-set value between 30 and 70 ºC. In addition, the faces of the loading plates in contact with the specimen have carved grooves through which a solution may circulate to keep the specimen wet and supply alkalis. The confining pressure and the specimen temperature, as well as the data acquisition, are controlled by a LabVIEW-based computer system. For a more detailed description of the AARTM refer to [14, 15].

The AARTM has been used for a first experimental campaign in which two different kinds of concrete were tested. The first one, the 'control concrete', was made only with non-reactive aggregates. In contrast, the second one, the 'reactive concrete', was made with crushed SL glass as replacement of the coarser fraction of aggregates. Control and reactive specimens were tested in the same conditions with

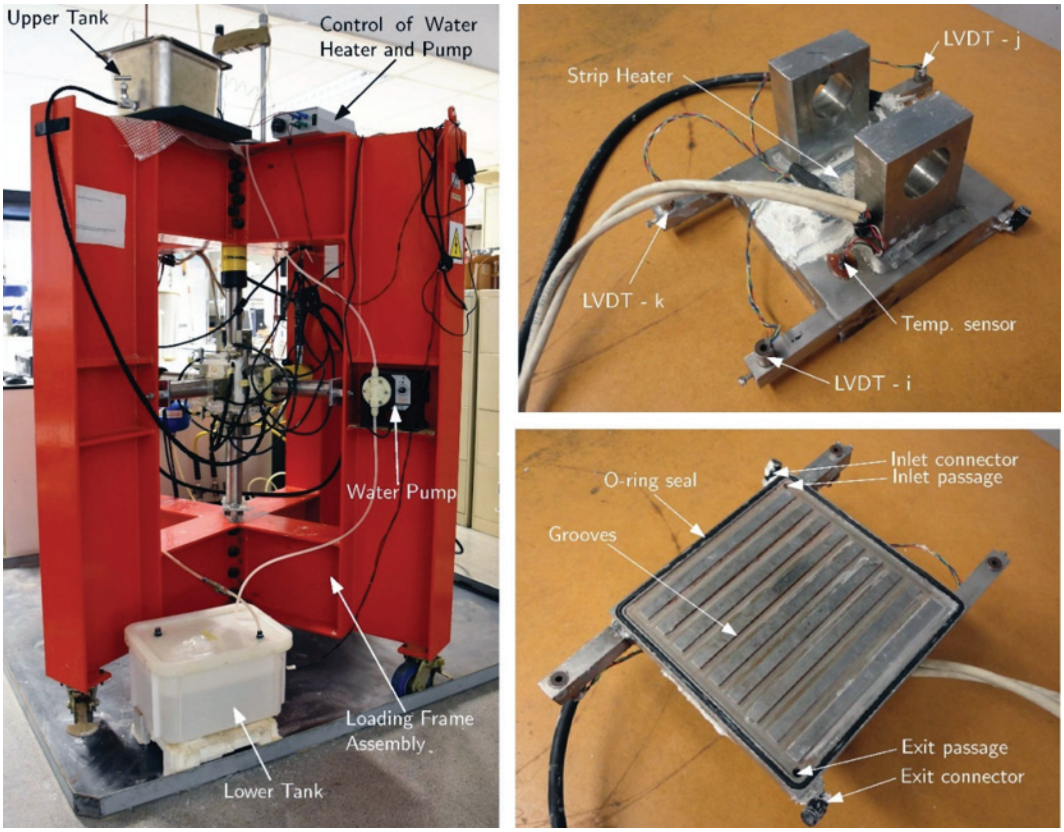

Figure 4 Left, general view of the AARTM. Right, detail views of an active loading plate of the AARTM [15]

the purpose of isolating creep/shrinkage strains from ASR-induced expansions in the reactive specimens. Four different load cases were investigated: 0-0-0, 1-1-1, 9-9-1, and 9-9-9. This notation indicates the compression stress applied in each axis. For instance, '9-9-1' indicates that compression stresses of 9 MPa were applied in the X- and Y-direction and 1 MPa was applied in the Z-direction. The test temperature was 60 ºC and the circulating solution was 1 m NaOH solution. The load case 0-0-0 (free expansion) was not carried out with the AARTM because a minimum pressure is needed to prevent the leakage of the alkaline solution circulating in between the loading plates and the specimen. Alternatively, free expansion tests were performed with a different procedure, using airtight containers with alkaline solution for storing the specimens in an oven at 60 ºC, and extracting the specimens regularly to measure ASR expansions with a DEMEC strain gage. For additional information about the specimens preparation, curing conditions, and testing methodology refer to [14, 15].

Figure 5a-c show the axial strain curves of the reactive specimens tested with the AARTM, after deducting the creep strains obtained with control specimens in the same conditions (not presented here). For each load case, two specimens were tested, which are differentiated in the plots with circular and square markers. Figure 5d shows the comparison of average volumetric strain curves, after deducting creep, obtained with the AARTM as well as with free expansion condtions.

Let us first consider the ASR expansion curves obtained with the AARTM for isotropic load cases 1-1-1 (Figure 5a) and 9-9-9 (Figure 5c). As it was observed in the free expansion tests (not presented here), the expansion rates are roughly isotropic. The expansion rates under load case 1-1-1 are a little below than in free expansion conditions, but much higher than the expansion rates under load case 9-9-9. For load case 9-9-1 (Figure 5b), the expansion rates in the most loaded directions are similar to the expansion rates in the 9-9-9 load case, but, remarkably, the expansion rate in the Z-direction (the 1-MPa-direction) is higher than that measured for the 1-1-1 load case. This seems to indicate that there is a certain expansion transfer from the most compressed directions to the less compressed one. Finally, Figure 5d shows that the volumetric expansion rate decreases as the applied volumetric stress is increased.

After the standard testing time of 21 days had been completed, the stress states of two specimens (TM14 and TM21) were changed and the tests continued for an additional period of approximately 12 days. The axial strain curves of these specimens with the additional testing period are shown in Figure 6. These curves are the raw ones, i.e. without any creep deduction, because the counterpart control specimens were not subject to the same changes of the stress state.

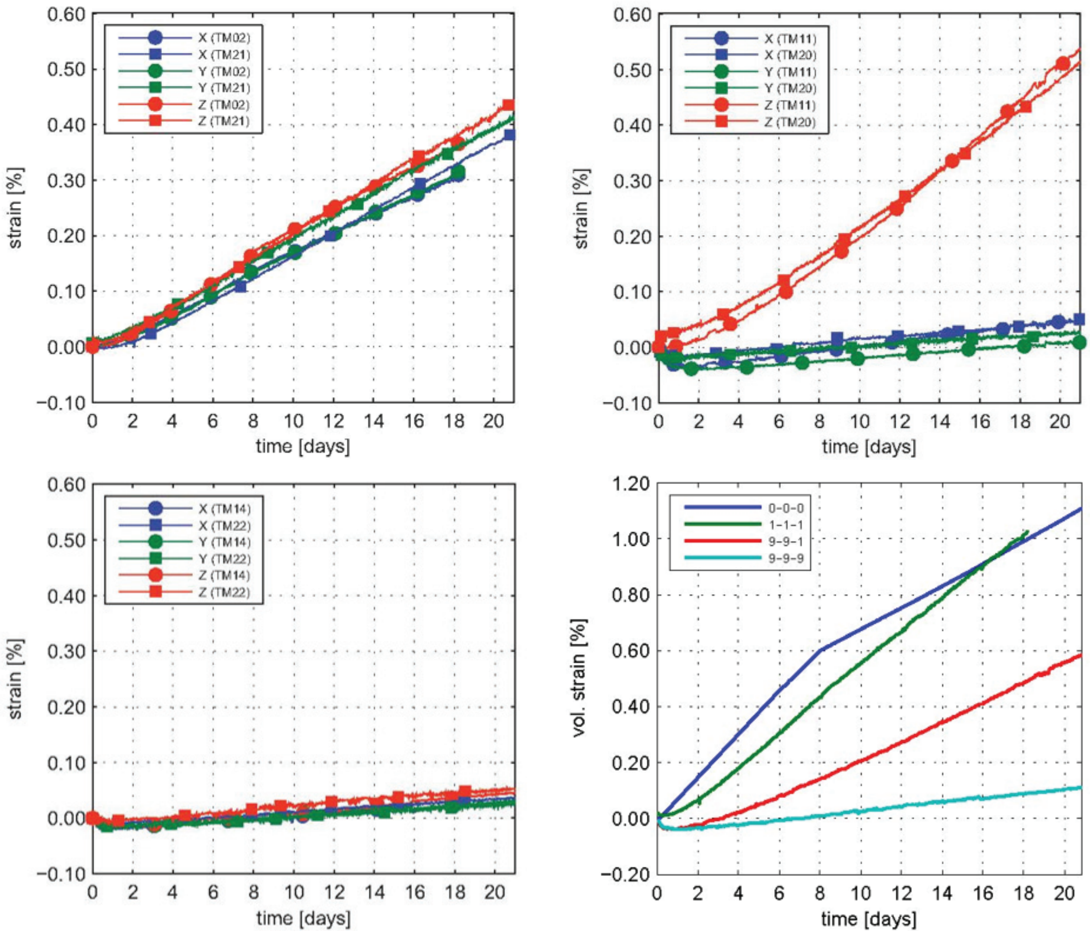

Figure 5 (a-c) Axial strain curves, after deducting creep, of reactive specimens under 1-1-1, 9-9-9, and 9-9-1 load cases, respectively. (d) Comparison of average volumetric strain curves, after deducting creep, of reactive specimens under different triaxial confinement stress values. After [15]

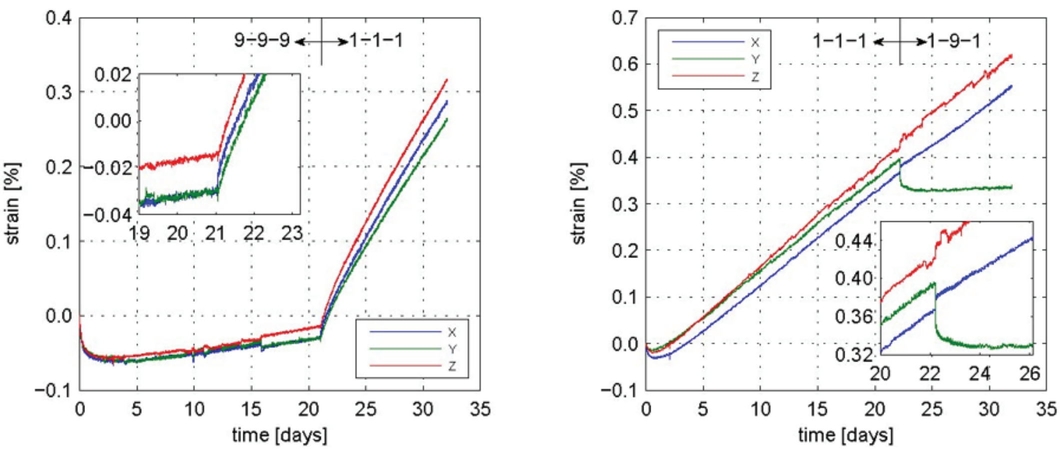

Figure 6 Axial strain curves (without deducting any creep effects) of: (a) reactive specimen first subjected to load case 9-9-9 for 21 days and then to load case 1-1-1 until the end of the test; (b) reactive specimen first subjected to load case 1-1-1 for 22 days and then to load case 1-9-1 until the end of the test. After [15]

The stresses on specimen TM14 were reduced from 9-9-9 to 1-1-1, resulting in a significant increase of the expansion rate, as it can be observed in Figure 6a). The expansion rates were maximum immediately after the stress change, decreasing asymptotically to constant rate values in the following days. Remarkably, no instantaneous elastic expansions due to the reduction of the compression stresses is distinguished in the curves. The asymptotic values of the expansion rates are about 30% greater than the ASR expansion rates obtained for load case 1-1-1 (Figure 5a). These greater expansion rates might be attributed to two different reasons:

- The decompression of the specimen may have originated a delayed elastic creep expansion of concrete, which could explain, at least in part, the initial variation of the expansion rates.
- The swelling of ASR gel formed under the 9-9-9 stress state due to water absorption when the confining stresses reduce to 1-1-1.

The stress state of specimen TM21 was changed after 22 days from 1-1-1 to 1-9-1 (Figure 6a). In contrast with the previous case, instantaneous strains are clearly distinguished: a negative strain jump in the Y-direction and smaller positive strain jumps in the X - and Z - directions (Poisson's effect). Subsequently, the expansion rate in the Y-direction goes practically to zero, while in the X- and Z - directions the expansions rates are 10 20% smaller than for the previous 1-1-1 stress state. Again, the net ASR expansion rates in the secondary load state cannot be obtained because of the lack of a counterpart control specimen with the same stress history. However, it may be expected that the deduction of the creep strains would result in a small increase of the expansion rate in the Y-direction and an even smaller, if any, reduction in the X - and Z - direction rates, due to Poisson's effect on creep strains. Therefore, the increase of the Y-stress seems not only to have reduced the expansion rate in the Y- direction, but also the expansion rates in the other two directions.

Clearly, additional research is needed to confirm the previous observations regarding the effect of changing the stress state on ASR expansions.

With the purpose of studying the ASR products formed, samples were taken from specimen TM02 (1-1-1 load case) for performing SEM/EDS analyses. Two of the SEM images obtained are shown in Figure 7. In those analyses, three types of ASR products have been identified:

- Low-calcium product. Mainly localized within cracks inside glass particles, with molar ratios Ca/Si ≈ 0.22-0.35 and (Na + K)/Si ≈ 0.14-0.28.
- High-calcium product. Localized within cracks in the limestone mortar, with molar ratios Ca/Si ≈ 1.40-1.43 and (Na + K)/Si ≈ 0.12-0.15.
- Intermediate product. Transitional product between the low- and high-calcium products, with calcium content ranging in between the two extreme values. Alkali content, in turn, tends to decrease with increasing calcium content.

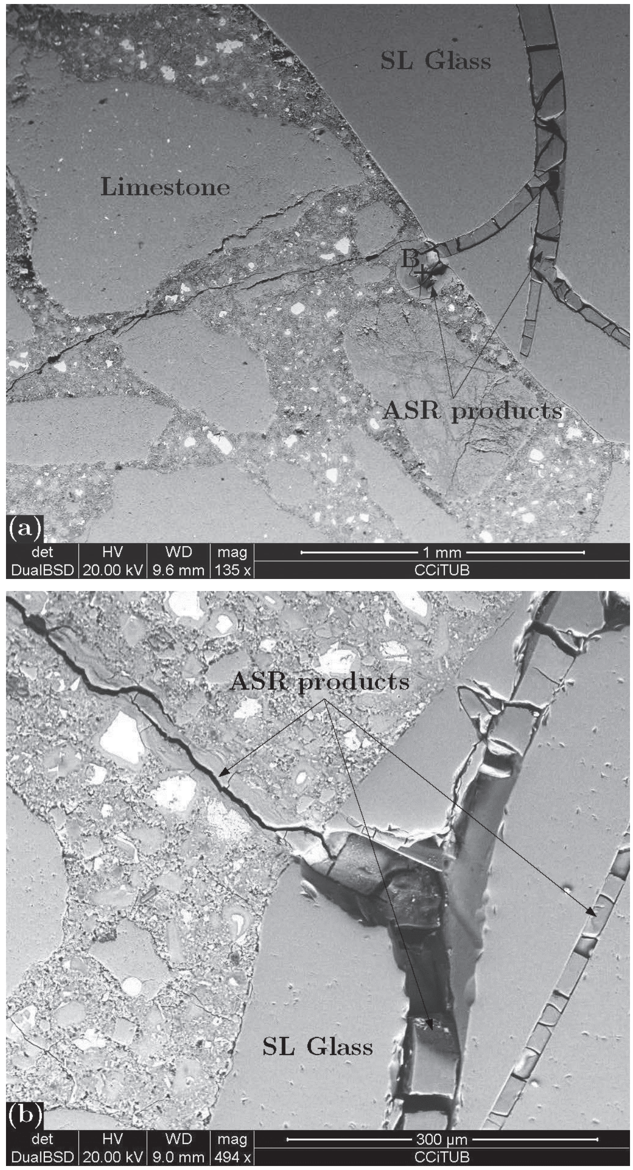

Figure 7 SEM images of a cross section of reactive specimen TM02 after testing (21 days under 1-1-1 load case) [16]

It is not possible to reconstruct the sequence of formation of the different ASR products and the propagation of cracks from a set of SEM images at a single testing time. However, based on the experimental study performed by Rajabipour et al. [19], it is possible to infer that ASR expansion begun mainly due to the precipitation of low-calcium products within pre-existing cracks inside glass particles. These pre-existing cracks are the residual result of the glass crushing process. The swelling of the low-calcium product within the residual cracks produced wedging stresses that propagate cracks towards the limestone mortar with the same orientation as the gel-filled residual cracks inside glass (Figure 7). The induced cracks in the limestone mortar were not initially filled with ASR products, but they were filled with intermediate and/or high-calcium products as the ASR progressed. Surprisingly, in most SEM images the glass-HCP interface appeared clean and did not show evidence of ASR products. In the few cases where a significant amount of ASR products was found at a glass-HCP interface, it was usually connected to a glass crack. Refer to [14] for additional SEM images and EDS analyses results.

4 Reaction-expansion mechanism for SL glass concrete

In SL glass mortar specimens tested according to ASTM C1260 (free expansion in 1 M NaOH solution at 80 °C) [20], Rajabipour *et al.* [19] found a diffuse layer of high-calcium ASR product (Ca/Si = 1.34-1.51, Na/Si = 0.06-0.29) of about 20 μm at the boundary between the glass and the HCP. Rajabipour et al. referred to this product as 'Pozzolanic CSH', differentiating it from the products with lower calcium content (Ca/Si = 0.29-0.37, (Na + K)/Si = 0.38-0.42) formed within cracks in the glass particles, which were called 'ASR gel'. The Pozzolanic CSH was regarded by the authors as a non-expansive product, attributing the observed expansion of the mortar uniquely to the ASR gel. This distinction between calcium-rich products with low swelling capacity and calcium-poor products with high swelling capacity has been also made by other authors [e.g. 9, 21, 22].

The diffuse layer of Pozzolanic CSH described by Rajabipour et al. could not be identified in the samples taken from specimen TM02 after the Confined Expansion Test (Figure 7), since in most cases the contacts between the mortar and the glass particles appeared clean and did not show evidence of ASR products.

In any case, in both studies (the one by Rajabipour et al. [19] and ours) the amount/morphology/location of the ASR products formed at the glass-HCP interfaces of glass concrete or mortar, if any, substantially differ from the well differentiated layers of reaction products obtained with the Interfacial Expansion Tests (Figure 7). Moreover, the interfacial expansion curves clearly indicate that high-calcium products (Pozzolanic CSH) is also capable of developing significant expansions.

A possible explanation to this incongruence may be found in the different mechanical restraint in each case. In the case of the Interfacial Expansion Tests, the ASR products only need to overcome the tensile strength of the glass-HCP interface in order to develop measurable expansions and to make room for further precipitation of reaction products. In contrast, in the case of glass particles within a cementitious matrix, the ASR products not only need to overcome the tensile strength of the glass-HCP interface, but also need to deform/crack the surrounding cementitious matrix (and even surpass superimposed external pressures, as in the case of specimen TM02). In other words, the swelling pressure needed for separating glass-HCP interfaces is certainly much lower in the first case than in the second case. These observations lead us to conjecture, in contrast with the interpretation of Rajabipour et al. [19], that the formation of high-calcium ASR products is indeed an expansive reaction, but an expansive reaction which can be slowed down by an applied pressure, or even inhibited if the applied pressure is higher than the Maximum Swelling-Pressure[1] (MSP) that can be developed by this reaction product. The low-calcium product within cracks inside glass particles, in turn, would have a similar behaviour but with a MSP significantly higher than the MSP of the high-calcium product. Considering that in the Confined Expansion Tests under load case 9-9-9, the glass concrete specimens were still capable of developing expansions, 9 MPa may be considered as a lower bound value of the MSP of low-calcium products. The real value has to be certainly higher, since, besides the external pressure, the low-calcium ASR products have also to overcome the internal restraints.

For the proposed interpretation of the experimental evidence, the ASR products are considered as an aggregation of colloidal particles of Calcium-Alkali-Silicate Hydrates (C-R-S-H) of variable composition which constitute a space-filling gel [1]. The C-R-S-H particles result from a number dissolution-formation reactions, in such a way that C-R-S-H with high calcium content is mainly formed at reaction sites close to HCP, while C-R-S-H with low calcium content is mainly formed in cracks inside the SL glass particles. In the resulting ASR products, two different fractions of water can be distinguished: the water chemically fixed in the C-R-S-H and the 'gel water', i.e. the water under the influence of absorbing forces. These forces may be attributed to different causes (e.g. osmotic pressure or double-layer repulsive forces) but, in any case, they are expected to be dependent on the chemical composition of the C-R-S-H. As water is absorbed, the content of gel water increases, the distance between the colloidal particles increases and, consequently, the 'bulk' volume of the ASR product increases. If this swelling is restrained by the solid skeleton around the reaction site, a mechanical pressure will build up on the ASR gel counteracting the absorption forces and, therefore, the volume of water absorbed will be lower than in free swelling conditions. In contrast, if the mechanical restraint is released, the original capacity of water absorption will be restored and the ASR products will absorb water and swell. The gel water is considered as part of the concrete pore solution, i.e. as an aqueous medium in which diffusion-reaction processes may take place. Therefore, a reduction of the gel water content is expected to reduce the ASR rate by locally reducing the volume of reacting medium, the 'wet' surface area of dissolving silica and/or the effective diffusion section.

5 Concluding remarks

With regard to the Interfacial Expansion Tests, the proposed methodology meets the objective of measuring ASR expansions at the level of a single interface between a reactive aggregate and a cementitious matrix. This methodology can provide valuable information about the ASR expansion mechanisms, being at the same time inexpensive and easy to replicate. Moreover, the simplicity of the geometry and of the boundary conditions of the tested specimens make these tests ideal for the calibration of micro- and meso-scale numerical models for ASR expansion in concrete, as it has been done by the authors elsewhere [14, 17].

1 Swelling pressure is defined as the pressure developed by the formation of ASR products under constant volume conditions.

The results obtained demonstrate that the high-calcium ASR products (molar Ca/Si ≈ 1.0-1.5) formed at the interfaces between SL glass and cement paste or mortar, which has been considered as non-expansive by some authors [19, 23], are actually capable of developing significant expansions at reaction sites with low mechanical restraint.

With regard to the Confined Expansions Tests, the AARTM has shown to be capable of accurately applying and maintaining targeted true-triaxial compressive stress states and temperatures on the specimen, while keeping it in contact with a highly alkaline solution. In contrast with other testing setups with triaxial confinement proposed in the literature, the AARTM has the advantage of being capable of applying quasi-uniform constant true-triaxial stress states.

The results obtained with specimens made with crushed SL glass as reactive specimens seem to indicate that:

- The volumetric ASR expansion rate is reduced as the applied volumetric compressive stress is increased.
- Under anisotropic stress states, there is an increase of the expansion rate in the less compressed direction in detriment of the expansion rates in the most compressed directions.
- SEM/EDS analyses of the reaction products and cracking of a specimen tested under isotropic pressure of 1 MPa, indicate the presence of ASR products with variable calcium content, from low-calcium products (molar Ca/Si ≈ 0.30) inside cracks within glass particles to high-calcium products (molar Ca/Si ≈ 1.40) formed in contact with the HCP. Most of the ASR expansion and cracking is attributed to the low-calcium product.

Based on the experimental results obtained with both testing methodologies, as well as on other experimental results found in the literature, a new reaction-expansion mechanism for ASR in SL glass concrete has been proposed. This mechanism is based on the assumption that the gel water content of the ASR products is reduced as the applied compression stress is increased. Then, because the rate of formation of ASR products depends on the amount of (free and gel) pore water at the reaction site, the development of compression stresses in the ASR products filling a crack reduces the reaction rates at this location or even completely stops them. The proposed mechanism has been implemented in a coupled C-M FE model, which has been used to reproduce the experimental reproduce the experimental results summarized in this paper [14, 17].

Acknowledgements

This research is supported by grants BIA2016-76543-R from MEC (Madrid), which includes FEDER funds, and 2017SGR-1153 from AGAUR-Generalitat de Catalunya (Barcelona). The first author thanks the scholarship FPI (BES-2010-030515) from MEC (Madrid).

References

[1] Rajabipour, F.; Giannini, E.; Dunant, C.F. *et al* (2015) – Alkali-silica reaction: Current understanding of the reaction mechanisms and the knowledge gaps. Cem Concr Res 76: 130-146. https://doi.org/10.1016/j.cemconres.2015.05.024

[2] Saouma V.E.; Xi, Y (2004) – CU/SA-XI-2004/001 Literature Review of Alkali Aggregate Reactions in Concrete Dams

[3] Poole, A.B. (1992) – Introduction to alkali-aggregate reaction in concrete. In: Swamy RN (ed) The Alkali-Silica Reaction in Concrete. Blackie and Son Ltd., Glasgow, pp 1-29

[4] Stanton, T. (1940) – Expansion of concrete through reaction between cement and aggregate. In: Proceedings of American Society of Civil Engineers 66. pp 1781-1811

[5] Stanton, T.; Porter, O.; Meder, L.; Nicol, A. (1942) – California experience with the expansion of concrete through reaction between cement and aggregate. In: ACI Journal Proceedings. pp 209-236

[6] ACI (1998) – State-of-the-Art Report on Alkali-Aggregate Reactivity Reported by ACI Committee 221

[7] McGowan, J.K.; Vivian, H.E. (1955) – The Effect of Superincumbent Load on Mortar Bar Expansion. Aust J Appl Sci 6:94-99

[8] Struble, L.J.; Diamond, S. (1981) – Unstable swelling behaviour of alkali silica gels. Cem Concr Res 11:611-617

[9] Leemann, A. (2012) – Alkali-Silica Reaction autogenous deformations and pressure development in a model system. In: Drimalas, T.; Ideker, J.H.; Fournier, B. (eds) 14th International Conference on Alkali-Aggregate Reactions in Concrete. Austin, Texas, USA

[10] Dunant, C.F.; Scrivener, K.L. (2012) – Effects of uniaxial stress on alkali-silica reaction induced expansion of concrete. Cem Concr Res 42:567-576. https://doi.org/10.1016/j.cemconres.2011.12.004

[11] Larive, C. (1997) – Apports combinés de l'expérimentation et de la modélisation à la compréhension de l'alcali-réaction et de ses effets mécaniques. École Nationale des Ponts et Chaussées, http://tel.archives-ouvertes.fr/tel-00520676/

[12] Multon, S., Toutlemonde, F. (2006) – Effect of applied stresses on alkali-silica reaction-induced expansions. Cem Concr Res 36:912–920. https://doi.org/10.1016/j.cemconres.2005.11.012

[13] Gautam, B.P.; Panesar, D.K.; Sheikh, S.A.; Vecchio, F.J. (2017) – Multiaxial Expansion-Stress Relationship for Alkali Silica Reaction-Affected Concrete. ACI Mater J 114:171–184. https://doi.org/10.14359/51689490

[14] Liaudat, J. (2018) – Experimental and numerical study of the effect of stress on ASR expansions in concrete. Universitat Politècnica de Catalunya, http://hdl.handle.net/10803/620624

[15] Liaudat, J.; Carol, I.; López, C.M.; Saouma, V.E. (2018) – ASR Expansions in Concrete under Triaxial Confinement. Cem Concr Compos 86:160-170. https://doi.org/10.1016/j.cemconcomp.2017.10.010

[16] Liaudat, J.; Carol, I.; López, C.M.; Leemann, A. (2019) – ASR expansions at the level of a single glass-cement paste interface: experimental results and proposal of a reaction-expansion mechanism. Constr Build Mater 218:108-118. https://doi.org/10.1016/j.conbuildmat.2019.05.106

[17] Liaudat, J.; Carol, I.; López, C.M. (2020) – Model for Alkali-Silica Reaction expansions in concrete using zero-thickness Chemo-Mechanical interface elements. Int J Solids Struct 207:145–177. https://doi.org/10.1016/j.ijsolstr.2020.09.019

[18] Gautam, B.P.; Panesar, D.K. (2016) – A new method of applying long-term multiaxial stresses in concrete specimens undergoing ASR, and their triaxial expansions. Mater Struct 49:3495–3508. https://doi.org/10.1617/s11527-015-0734-z

[19] Rajabipour, F.; Maraghechi, H.; Fischer, G. (2010) – Investigating the alkali-silica reaction of recycled glass aggregates in concrete materials. J Mater Civ Eng 22:1201–1208. https://doi.org/10.1061/(ASCE)MT.1943-5533.0000126

[20] ASTM (2007) – ASTM C1260-07 Standard Test Method for Potential Alkali Reactivity of Aggregate (Mortar-Bar Method). In: Annual Book of ASTM Standars. ASTM International

[21] Leemann, A.; Le Saout, G.; Winnefeld, F. *et al* (2011) – Alkali-Silica Reaction: the influence of calcium on silica dissolution and the formation of reaction products. J Am Ceram Soc 94:1243–1249. https://doi.org/10.1111/j.1551-2916.2010.04202.x

[22] Prezzi, M.; Monteiro, P.J.M.; Sposito, G. (1997) – The alkali-silica reaction, Part I: use of the double-layer theory to explain the behavior of reaction-product gels. ACI Mater J 1:10-16

[23] Maraghechi, H.; Shafaatian, S.M.H.; Fischer, G.; Rajabipour, F. (2012) – The role of residual cracks on alkali silica reactivity of recycled glass aggregates. Cem Concr Res 34:41–47.
https://doi.org/10.1016/j.cemconcomp.2011.07.00

Interaction of DEF and AAR, a review

Interação entre a RSI e a RAA: uma revisão

Bruno Godart
Jonathan Wood (†)

Abstract

AAR and DEF can lead to the development of severe cracking in structures. Both reactions are often associated with high cement content mixes: AAR because of the increased availability of alkalis, DEF because the heat of cement hydration can lead to temperatures over 65 ºC, above which sulphates lead to the delayed formation of expansive ettringite.

High cement content mixes, favoured by contractors for early strength gain and workability, also lead to increased early age thermal and shrinkage cracking. This cracking becomes increasingly complex as it is enlarged by the swelling from AAR and/or DEF, which later impose their own characteristics, modified by constraints from stress and reinforcement.

The paper considers AAR and DEF at the scale of the interaction of paste with aggregate, as observable petrographically and from changed physical properties. Examples of large scale laboratory tests on beams further clarify the interactions which are also illustrated by reference to major structures which have suffered AAR, DEF and combined AAR/DEF damage.

Resumo

A RAA e a RSI podem levar ao desenvolvimento de fissuração expressiva nas estruturas. As duas reações estão frequentemente associadas a betões com elevado teor de cimento: na RAA devido ao aumento da disponibilidade de álcalis e na RSI porque o calor da hidratação do cimento pode levar a temperaturas acima de 65 ºC, para as quais os sulfatos levam à formação retardada de etringite expansiva.

Misturas com elevado teor de cimento, preferidas pelos empreiteiros para ganhar trabalhabilidade e resistência iniciais, também induzem nas primeiras idades a formação de fissuras de origem térmica e por retração. Essa fissuração torna-se mais complexa à medida que é potenciada pela expansão devida à RAA e/ou à RSI, que posteriormente impõe as suas características próprias, que podem ser modificadas por restrições de tensões e de reforços.

O artigo considera a RAA e a RSI à escala da interação da pasta de cimento com o agregado, ao nível das observações petrográficas e a partir das propriedades físicas alteradas. São apresentados exemplos de ensaios de laboratório em vigas em grande escala, que esclarecem as interações, que são também ilustradas por referência a estruturas que sofreram danos pela RAA, RSI e RAA/RSI combinadas.

Keywords: Concrete / Structure / AAR / DEF / Cracking

Palavras-chave: Betão / Estrutura / RAA / RSI / Fissuração

Bruno Godart

Gustave Eiffel University
IFSTTAR
Champs-sur-Marne, France
bruno.godart@univ-eiffel.fr

Jonathan Wood (†)

Structural Studies & Design Ltd.
Petworth, Sussex, UK

GODART, B. [*et al.*] – Interaction of DEF and AAR, a review. **Revista Portuguesa de Engenharia de Estruturas**. Ed. LNEC. Série III. n.º 15. ISSN 2183-8488. (março 2021) 25-34.

1 Introduction

Both Alkali Aggregate Reaction (AAR) and Delayed Ettringite Formation (DEF) can lead to the development of severe cracking in concrete structures over decades as a consequence of internal expansions. This can create structural uncertainty and risks of functional failures in bridges, dams and buildings. In extreme cases, it has led to their demolition and replacement. The processes are distinct, but may interact in real structures.

External sulfate attack from soils or water is distinct from the internal effects of DEF. There are some analogies with DEF and the behaviour of expansive cements which use ettringite formation to give early age expansion to reduce shrinkage or create slight expansion to tension embedded reinforcement while putting concrete into compression to prevent cracking. External sulfate attack is out of the scope of the present article.

1.1 AAR: some historical aspects

AAR was first identified in the late 1930s by Stanton in California with fast reacting opaline aggregates. The alkalis in cement were found to react with disordered forms of silica in aggregate to produce silica gel which is hygroscopic and swells in damp conditions. This swelling of the gel can develop within aggregates splitting them, on the aggregate surfaces or, with fluid gels, as the gel spreads into the adjacent cracks, see Figure 1. Over the past 40 years AAR became the subject of detailed studies of the alkalinity of cement paste and pore solution in parallel with petrographic studies of the siliceous minerals and the microcracking and gel formation.

As the years went by, an increasing number of structures were found to be suffering damage from slowly developing severe cracking. Typically, this only became noticeable five or more years after construction. By 1980, petrographic analysis provided a basis for diagnosis of AAR, but not for assessing its structural implications. Since then, specifications and appropriate testing to minimise the risk of AAR damage in new construction have evolved, often tailored to national materials and experience.

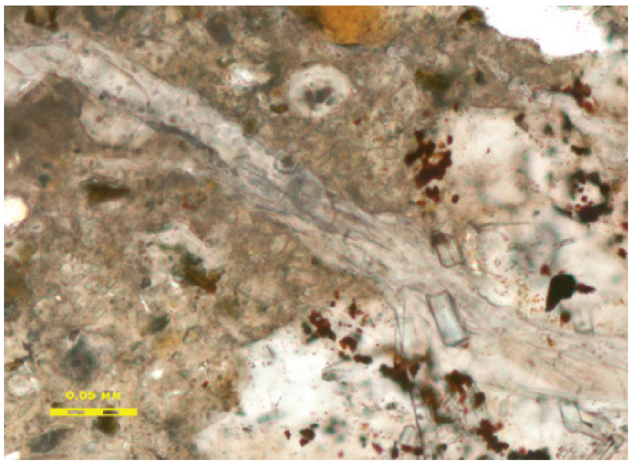

Figure 1 AAR with gel in cracked aggregate and into cracked paste

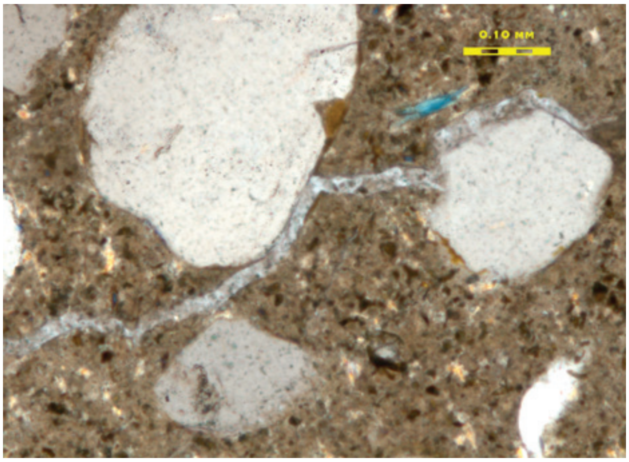

Figure 2 DEF forming in cracks in paste and around Aggregate

More recently RILEM has coordinated research to develop these into international guidance on specification [1]. Distinct, but allied, research has developed testing for diagnosis, prognosis and assessment for evaluation of AAR damage in structures [2].

1.2 DEF: some historical aspects

DEF was initially identified in the 1980s by Heinz [3] as a cause of deterioration in precast elements which had been cured at high temperatures to accelerate production. It was established that, at temperatures over about 70 °C, the sulfates in cement would form as monosulfates. With time in moist conditions the monosulfates can revert to ettringite $Ca_6[Al(OH)_6]2 \cdot (SO_4)_2 \cdot 26H_2O$. This ettringite is formed within the paste or into cracks and voids (see. Figure 2). The swelling results from the large volume of H_20 incorporated into ettringite crystals.

In 1997, Divet [4] observed for the first time in France DEF in the capbeam of the Ondes bridge near Toulouse, whose concrete had been cast on site. Then, other bridges damaged by DEF were discovered and investigated. In these bridges, the damaged parts were primarily massive structural elements (piers, crossbeams on piers or abutments, etc.) in contact with water or subjected to high moisture. In 2001, Divet [5] was able to highlight some important features, based on a comparative study of factors encountered in damaged and non damaged bridges. These general features are the following:

- the minimum delay for observing cracking on structures is around 6 to 8 years;
- the maximum temperature reached in those massive parts affected by DEF are above 75 °C to 80 °C;
- the casting of the concrete took place during the summer months;
- the nature of the cement is a CEM I and the cement content is above 400 kg/m^3;
- the SO_3 content of the cement is above 2.5 % and the C_3A cement content above 8 %.

Lessons learned from these cases were used to develop a prevention strategy [6]. Thereafter, some bridges decks composed of prestressed precast concrete beams were discovered as affected by DEF; longitudinal and shear cracks developed in these pre-tensioned beams. The main cause could be attributed to the use of a high temperature cycle during the heating phase in the factory. In France, now, about one hundred and fifty bridges and very few dams are damaged by DEF to a more or less extent.

1.3 Concomitance of AAR and DEF

Petrographic examination of samples enables the relative importance of AAR and DEF and other deterioration mechanisms to be identified and related to the temperature and moisture history of the concrete. Surface coring can show AAR features in moist concrete. For DEF, the as cast heat profile must first be estimated, followed by coring through the cooler surface zone into hottest zones which may have exceed 65 °C, with moisture in the long term.

In 2001, Taylor [7] reviewed subsequent research on DEF and its interaction with AAR. He refers to some examples of DEF in mass concrete were hydration had raised temperature to above 70 °C. When siliceous aggregates were used, this was associated with extensive damage from AAR. Taylor stresses the need to differentiate between:

- the damaging expansions from the formation of ettringite trapped within the cement paste leading to cracks developing around aggregates
- the migration of ettringite from within the paste to form larger crystals to fill space in cracks and voids without generating expansions. Ettringite in cracks from AAR is often observed when using petrography to study AAR damage.

Taylor and a more recent review by Thomas [8] have confirmed that although aggregate type and sulfate content can influence DEF damage, the dominant factor is the peak temperature after casting. Since Taylor's review, a range of significant cases of DEF damage in major in-situ concrete structures, with and without AAR have been investigated. This justifies rigorous control of peak temperatures during construction particularly when there are high temperatures, massive pours and/or high cement contents.

2 Why have AAR become widespread and not DEF?

The causes, physicochemical mechanisms and kinetics of the reaction that gives rise to the DEF swelling phenomenon, as well as the impact of the various parameters affecting DEF, are not yet thoroughly understood and continue to be the topic of widespread research. It appears however that an adverse combination of several parameters is essential to initiating and extending the DEF. This probably explains the rather low number of structures currently identified as experiencing DEF in the world, compared to the high number of structures affected by AAR where only 2 main parameters (reactive silica in aggregates and level of alkalis in concrete) are essential to trigger the reaction.

The principal parameters involved in DEF are the following:

- Temperature and its duration of application: The maximum temperature reached as well as the amount of time high temperature is maintained both influence the risk of delayed ettringite formation. Laboratory work has shown that if the temperature exceeds 65 °C and if other key parameters are present, DEF can develop to damage concrete. Exothermal heating of the concrete during hydration is a necessary precondition, yet on its own remains insufficient. A mix temperature of 20 °C with 44 °C rise from a 400 kg/m^3 cement will only just reach 64°C in the core of a very large pour, so DEF is unlikely in temperate climates with moderate cement contents.
- Sulphate and aluminate contents of the cement: Sulphates and aluminates are directly involved in the reactive mechanism that serves to form ettringite and DEF can only arise if the cement contains a high enough quantity of both tricalcic aluminates (3CaO Al_2O_3 or C_3A) and sulphates (SO_3).
- Alkali content of the concrete: the role of this on ettringite solubility is well documented. Ettringite is more highly soluble at higher alkali rates. As a result of ettringite solubility variation with temperature, a strong interaction exists between these two parameters during the DEF process. All other parameters being the same, a drop in the initial alkali content serves to increase the critical temperature value. This parameter plays also a paramount role in the case of AAR.
- Water and high humidity: water is a reactive medium essential to producing the reaction; it is as much involved in the transfer process as in the actual formation of reaction products. DEF primarily affects the parts of structures either in contact with water (submerged zone, tidal zone) or subjected to water ingress (exposure to bad weather, waterproofing defects, absence of drainage, etc.), or sometimes exposed to a high moisture level (at least 92 % RH).

The expansive or non-expansive nature of ettringite depends on the initial chemical composition, particularly on the type of cement (contents of aluminates and alkali, quantity of potentially-formed Portlandite) and the quantity of sulphates capable of being mobilised. There is not a consensus on the detailed mechanism by which ettringite formation is able to generate pressures inside concrete. Two principal mechanisms, which are to some extent linked to each other, have been proposed to explain the swelling caused by ettringite formation:

- swelling due to the crystallisation pressures inherent in ettringite crystal growth,
- swelling due to the osmotic pressures caused by an increase in the amount of colloidal ettringite.

It is likely that both of these mechanisms play a role simultaneously and cannot be dissociated from one another.

3 Why do AAR and DEF may coexist?

Several conditions are necessary at the time of casting for developing DEF. Even if calcareous aggregates may be more prone to DEF than siliceous ones, the type of aggregates is not among the most important parameters of DEF. In contrast, the type of aggregate has a paramount role in the case of AAR. It is enough to combine the conditions for DEF listed above with a reactive aggregate and an alkali content in concrete greater than 3 kg/m^3 to develop both AAR and DEF.

Designers wanting ever higher strength and contractors wanting earlier strengths has led to cement contents rising from the reasonable 350 kg/m^3 to many examples of 500 kg/m^3 or more. This raised alkali levels in concrete, with 0.8% Na_2Oeq in cement, from 2.8 kg/m^3 to 4.0 kg/m^3, i.e. above the safe 3.0 kg/m^3 threshold for most UK aggregates. When concrete mixes have been pumped, cement contents could exceed 600 kg/m^3.

These high cement contents lead to high temperatures in pours. 350 kg/m^3 gives a typical 38 °C temperature rise above mix temperature so there is little risk of exceeding 65 °C to inducing DEF. However, with 500 kg/m^3 of cement in a large pour of concrete mixed at 15 °C, the temperature will reach 70 °C in the core. Higher mix temperatures and/or higher cement contents will produce DEF if moisture can reach the areas which were overheated..

The following question then arises: which is the first reaction initiating damage ? It probably depends on the speed of development of each of the two reactions inside concrete. What is clear is that when one of the two reactions is triggered, it creates micro-cracks into concrete which accelerates the development of both reactions because of the easier transport of water and ions within the cracks.

4 The impact of AAR and DEF on mechanical properties of concrete

DEF leads to expansion that reduces the mechanical characteristics of concrete according to the extent of the reaction. As the paste expands with Ettringite it separates from the aggregates weakening the concrete. In the case of concretes with a 28-day strength of the order of 35 to 40 MPa, and that are exposed to thermal cycles which are typical of massive structures (a temperature plateau of 81 °C maintained for three days), Martin [12] obtained reductions in compressive strength of over 75% in the case of a concrete in which DEF has generated a maximum unrestrained expansion of approximately 14 mm/m (concrete tested after approximately 1,450 days of ageing). The Young's modulus was reduced by almost 90 % (as determined by linear regression of the stress-strain plot over three loading cycles at between 5 and approximately 30 % of the concrete's compressive strength). These drastic reductions in the mechanical performance should nevertheless be seen in the context of the very high level of expansion exhibited by this particular material. In the case of more moderate unrestrained expansion (1.2 mm/m), Martin [12] observed a much smaller reduction in Young's modulus of approximately 14% at 1,350 days. This expansion and deterioration will only occur in the centre of the pour not the cooler near surface zones which did not exceed 65 °C.

Considering the possible concomitance of AAR and DEF, an important question is to know the mechanical consequences of this coupled phenomenon on the behaviour of structures, and a good way to approach this question is by comparing the mechanical effects of

AAR or DEF alone and AAR & DEF together on the behaviour of simple concrete elements, through testing in laboratory.

5 Impact of AAR, DEF and AAR & DEF on concrete elements

An experimental program was carried out at IFSTTAR in partnership with EDF (Electricité de France) in order to study the behaviour of cylinder and large scale laboratory beams. Its objective was to quantify at a macroscopic scale the mechanical effects of DEF and AAR acting separately or simultaneously. The results are summarized hereafter, which are described more extensively in [9] and [10].

5.1 Impact on concrete cylinders

Three concrete mixes were designed: the first one was AAR-reactive (A) the second one was DEF-reactive (D), and the third one AAR and DEF-reactive (AD). To ensure the development of DEF and AAR, the alkali content of both mixes was increased by adding K_2O in the mixing water, and to trigger DEF under controlled conditions, all cylinders were heat cured in water, after casting, at a temperature of 80 °C during 72 hours. A non reactive siliceous sand was used for D and AD cylinders, and two types of coarse aggregates were used: either a Non Reactive Siliceous aggregate for D cylinders or an Alkali Reactive Limestone aggregate for A and AD cylinders (Table 1). A cement C1 (CEM I 52.5) with a high content of alkalis (Na_2 Oeq = 0.92 %) was used for the mix A, while a cement C2 (CEM I 52.5 R) with a high content of aluminates, sulfates and alkalis (respectively 3.5, 4.3 and 0.83 wt. %) was chosen to promote DEF.

The investigations were performed on cylinders (110 mm in diameter and 220 mm in height). The cylinders were subjected to free expansion tests under various moist exposures: each cylinder was stored at a temperature of 38 °C and either immersed in water (I) or in a 100 % Relative Humidity atmosphere (H100).

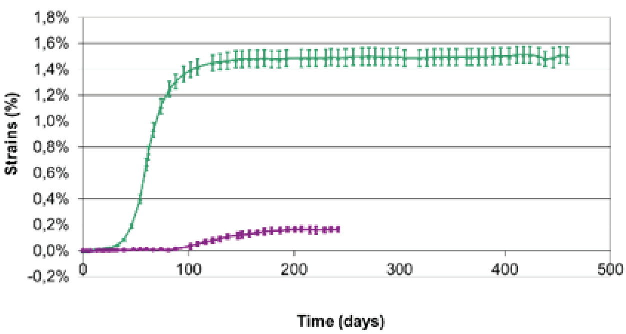

Figure 3 Expansion of AAR & DEF-reactive cylinders (green curve) and AAR-reactive cylinders (purple curve), all immersed in water (from [9])

The first evident result is that the expansion of A cylinders (0.2 %) is much smaller than that of AD cylinders (1.5 %) (see figure 3), as well as much smaller than the expansion of D cylinders. This comparison is only available for cylinders immersed in water since the authors did not test cylinders with AAR in 100 % HR condition. But it confirms a common feature observed in other experiments where the expansion of A cylinders cured at 38 °C and 100 % HR is generally lower than the expansion of D cylinders kept in water at 20 °C.

Figure 4 shows the expansion of DEF-reactive cylinders over a period of 550 days. It may be observed that the final expansion and the kinetics of the D cylinders are greater in water than in 100 % RH (final expansion of 1.5 % versus 1.25 %), which confirms the condition used for the LCPC accelerated expansion test for DEF [11]. One of the reasons is that storage in water promotes the leaching of alkalis and thus the precipitation of ettringite.

Figure 5 shows the expansion of AD cylinders over a period of 450 days. As for the D cylinders, the AD immersed cylinders exhibit a slightly faster development of the expansion at the beginning. However, after 120 days of exposure, the strains of the AD cylinders kept at 100 % RH are growing further significantly instead of reaching a plateau at 1.5 % as for the D cylinders stored in water. Finally, after a storage duration of about 350 days, the expansion processes of the D cylinders kept at 100 % RH are reaching also a plateau (for a value of the final expansion equal to 2.1 %).

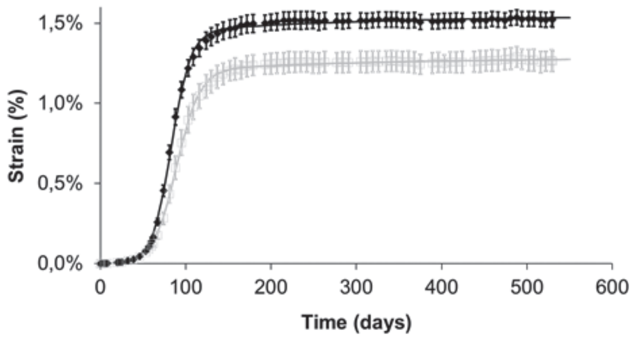

Figure 4 Expansion of DEF-reactive cylinders immersed in water (black curve) and in 100 % HR exposure (grey curve) – From [9]

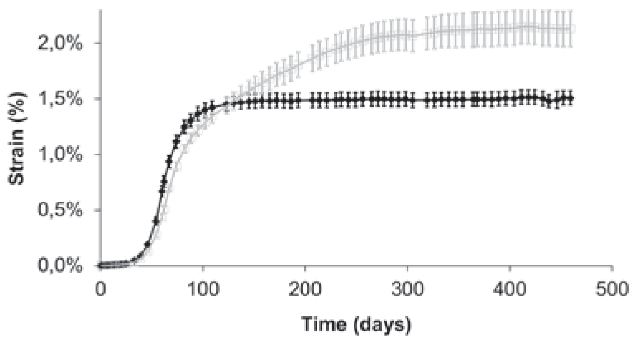

Figure 5 Expansion of AAR & DEF-reactive cylinders immersed in water (black curve) and in 100 % HR exposure (grey curve) – From [9]

Figure 6 shows a comparison between expansion of D and AD cylinders, all immersed in water. If the final expansion that reaches 1.5 % is the same, the onset of the swelling is earlier for AD cylinders than for D cylinders, and the speed of expansion is rather similar.

Table 1 Concrete mixes used for A, D and AD cylinders and beams

Mix	Reactivity	Cement type	Cement content (kg)	Water (l)	Non reactive limestone sand (kg)	Non reactive Siliceous aggregate (kg)	Reactive limestone aggregate (kg)	Na_2Oeq (%)
A	AAR	C1	410	205	621	0	1122	1.25
D	DEF	C2	410	188	0	1783	0	1.0
AD	AAR&DEF	C2	410	188	0	797	986	1.0

However, for this comparison, we must also take into account the fact that a reactive limestone aggregate was used for casting A cylinders and that a non-reactive siliceous aggregate was used for DEF. The difference in terms of behavior is too small to try to explain it.

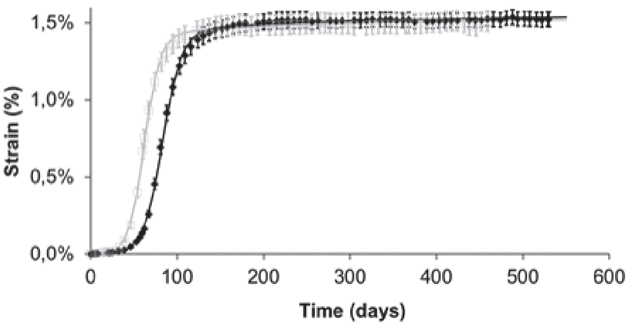

Figure 6 Expansion of DEF-reactive cylinders (black curve) and AAR & DEF-reactive cylinders (grey curve), all immersed in water – From [9]

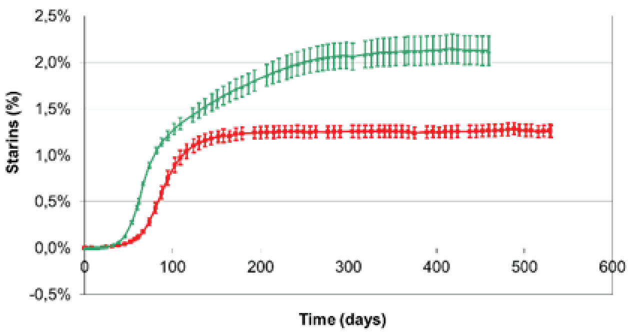

Figure 7 Expansion of DEF-reactive cylinders (red curve) and AAR & DEF-reactive cylinders (green curve), all in 100 % RH exposure – From [9]

Figures 7 shows a comparison between expansion of D and AD cylinders, all in a 100 % RH exposure. It appears that the expansion of AD cylinders is much greater than that of D cylinders. The effect of a saturated humidity is boosting AAR in the cylinders affected by AAR and DEF, but rather on the long term. At the beginning, a similar latency period is observed. Then an intense swelling with a higher speed mainly due to DEF is taking place for cylinders immersed by comparison with those at 100 % RH. According to [9], because of the development of a cracks network, leaching of alkalis may arise particularly in the case of immersed cylinders where water can penetrate into the cracks. This difference in terms of alkalis leaching means that more alkalis are present in the case of 100 % RH and can promote AAR, while less alkalis are present in the case of an immersed cylinders and reduce the AAR development. This mechanism assumes that DEF acts prior to AAR, what can be seen on figure 3.

In all the experiments, there is a rather good linear relationship between strains and mass variations for D and AD cylinders.

5.2 Impact on concrete beams

To study the structural effects of AAR and DEF acting separately or together, tests were performed by Martin & al. [10] on beams subjected to a controlled moisture gradient with the final objective to induce a gradient of imposed expansion. These tests were conducted on 6 beams (0.25m × 0.50m × 3.00m) named B1 to B6, as described in Table 2. Three of them were unreinforced and the other three were reinforced in the longitudinal direction with two rebars of 32 mm in diameter in the lower part and two rebars of 20 mm in diameter in the upper part. These simply supported beams were subjected to a moisture gradient during 430 days: the lower part of the beam was immersed in water on a depth of 7 cm while its upper face was drying in an atmosphere at 30% RH, and all lateral sides were sealed with adhesive aluminium sheets. All tests were performed at a constant temperature of 38 °C to speed up the drying process and the swelling reactions.

The vertical expansion measured was strongly dependent of the amount of water migrating from the immersed lower part up to the drying upper face. Because of the very high potential of free expansion (and associated cracking) of the concrete mixes D and AD, unreinforced beams B3 and B5 collapsed under dead weight effect after only 180 and 330 days of exposure, respectively. If we focus on the mechanical behaviour in the longitudinal direction, many interesting results were obtained.

Figure 8 shows that the longitudinal strains remain linear along the height during time for the unreinforced D-beam B3. This allows to calculate by double integration a deflection. Figure 9 presents this calculated deflection at mid-span with the deflections measured on the West (W) and East (E) sides of the beam B3, and indicates a good correlation.

Figure 10 and 11 present the same type of results for the reinforced D-beam B4. Again, the plane strains remain plane during the test, but for this beam, there was a big change around 250 days where the

Table 2 Beams tested (U = unreinforced, R = reinforced)

	B1	B2	B3	B4	B5	B6
Reactivity	AAR	AAR	DEF	DEF	AAR & DEF	AAR & DEF
Concrete mix	A	A	D	D	AD	AD
Reinforcement	U	R	U	R	U	R

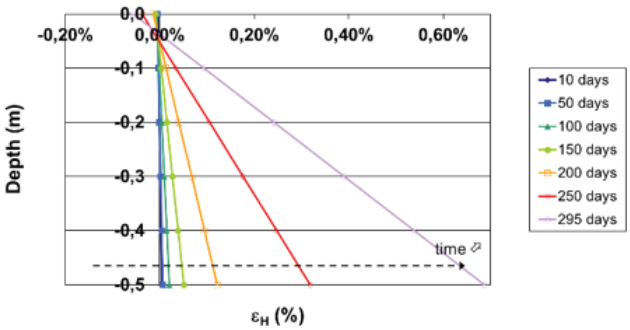

Figure 8 Evolution during time of the longitudinal strains with depth for DEF-beam B3 – (From [10])

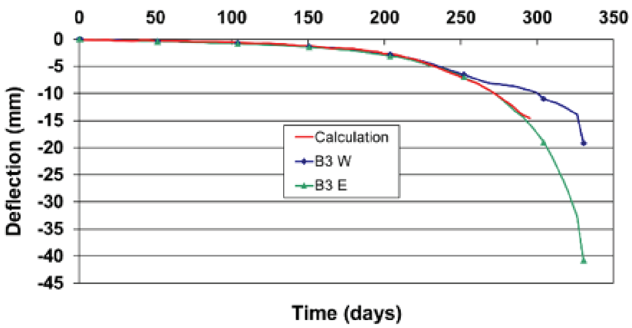

Figure 9 Mid-span deflection of the unreinforced DEF-beam B3 (From [10])

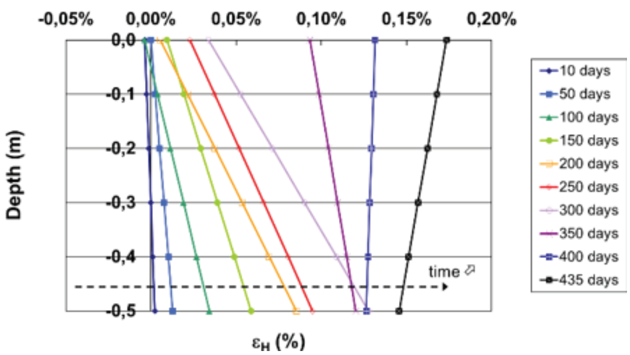

Figure 10 Evolution during time of the longitudinal strains with depth for DEF-beam B4 (From [10])

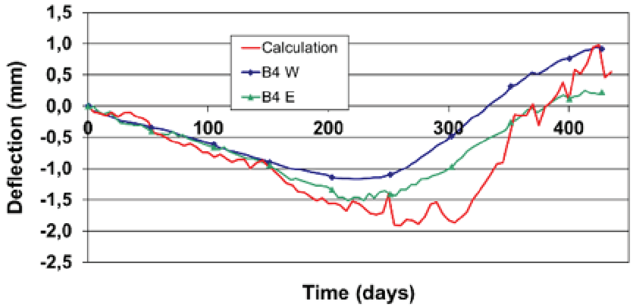

Figure 11 Mid-span deflection of the reinforced DEF-beam B4 (From [10])

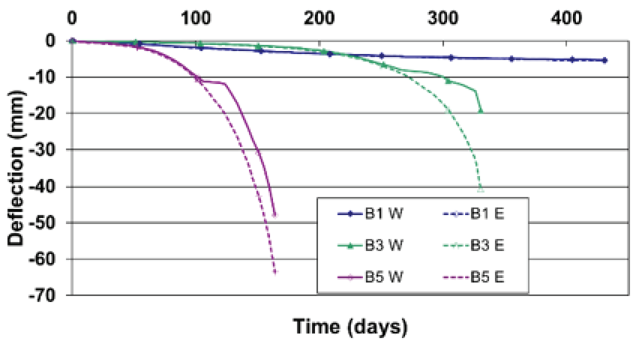

Figure 12 Mid-span deflection of the three unreinforced beams A-B1, D-B3 and AD-B5 (From [10])

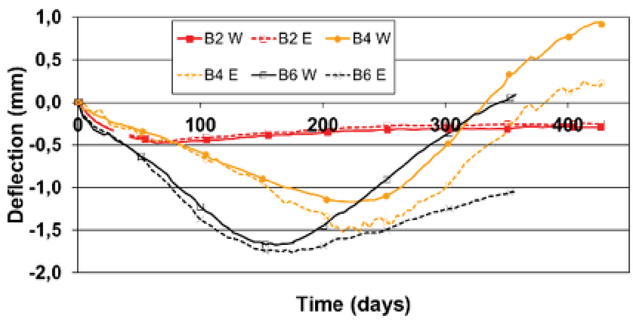

Figure 13 Mid-span deflection of the three reinforced beams A-B2, D-B4 and AD-B6 (From [10])

presence of the reinforcement in the bottom modified the structural behavior. In particular, for significant expansions developed in the lower part, the mechanical reaction of rebars to the imposed concrete expansion led to the development of a compression in this area leading to a bend upward of the beam.

Figure 12 illustrates the evolution of the mid-span deflection with time for the three unreinforced beams.

A-beam B1 reached a deflection value of about 5 mm that remains linear, while the deflection of B3 and B5 reached up to about 40 mm and 60 mm respectively. As for the cylinder, the AD-beam B5 presents a more rapid and more important deflection than the D-beam B3.

Figure 13 presents the evolution of the mid-span deflection with time for the 3 reinforced beams. For all beams, the curvature begins to decrease and then increases because of the "prestressing effect of the rebars": however, this effect is more important and rapid for the AD-beam B6 than for the D-beam B4 and rather negligible for the A-beam B2.

As a conclusion, it appears globally that AAR (with a typical magnitude of expansion 0.2- 0.3 %) is less damaging than DEF (with a typical magnitude of expansion 1.4-1.5 %), and that a combination of AAR and DEF is obviously the worst case. DEF and AAR & DEF may lead to a total collapse of unreinforced beams under their own weight. As for cylinders, there is a rather good linear relationship between strains and mass variations of the beams due to uptake of water for D and AD beams, what is not the case for A beams. Like Martin & al. [10], we may also conclude that the structural behavior of the beams can be described within the frame of the Strength of Materials.

6 About disorders on structures

The disorders on structures affected by DEF are similar to those observed on structures damaged by alkali-aggregate reaction, except for pop-outs, exsudation of gel and discoloration along cracks that are not encountered on structures having DEF. For both reactions, map cracking is the most frequent disorder observed on the facings of structures. Cracking is generally anarchic and can take the shape of a crazing with small mesh size (20 to 50 mm) and a rather small crack depth (a few centimeters), or take the shape of a larger crack network (30 to 40 cm size) with greater crack depth (greater than 10 cm).

Although the crack opening is variable in each observed zone according to the evolution rate of the reaction, this opening is generally greater with DEF than with AAR. The crack depth also varies with the degree of evolution of the disorders: cracking may be superficial (a few centimeters deep) or propagate in depth, until a through cracking. For both reactions, the map cracking can leave room for an oriented cracking in a structural element where there is a predominant direction of compression stresses. The cracks are opening in the direction perpendicular to the main compression axis. It is particularly the case of horizontal cracks developing in prestressed precast concrete beams, or vertical cracks occurring in columns or piers.

In the case of AAR, damage starts to become significant with expansions in the range 0.6 to 1.0 mm/m which can be detected by a Young's modulus reduction from microcracking of about 25 to 30 % [17]. Severe damage from AAR is associated with expansion in the range 2.0 mm/m to maximum seldom exceeding about 5.0 mm/m (Figure 14). It appears that expansions from DEF in extreme cases can exceed those from AAR (Figure 15). However the damage from AAR arises from the variability of expansion within pours due to heterogeneity giving variations in local expansions determined by local moisture, alkali and reactive aggregate concentrations. It appers that the expansions are generally less that those observed with DEF, and consequently the reductions of the mechanical characteristics of concrete are lesser.

Figure 14 AAR damage from severe 2 mm/m to 4 mm/m variable expansions

Figure 15 DEF damage from severe 1.5 to 5.5 mm/m variable expansions – (the white exsudations are calcite due to the dissolution of the lime of the cement and its carbonation with air)

7 Conclusions

Common features and differences between AAR and DEF have been presented, in the context of microscopic scale, materials and damages of affected structures. Although the reactions have similar macroscopic effects, the microscopic phenomena are very different.

The presence of alkalis has contrary effect: high alkali content tends to delay DEF while it boosts extensive AAR.

The tests performed confirm the generally observed higher magnitude of DEF expansion leading to collapse of the unreinforced beams under self weight, a phenomenon not found in testing AAR. The combination of both reactions accelerates the development of swelling and emphasizes the expansions; the consumption of alkalis to form the AAR gel leading to the precipitation of ettringite.

Both AAR and DEF lead to a decrease of the Young's modulus that can be explained by cracking of the matrix. With AAR, cracks develop in reactive aggregates and extend into the paste, but with DEF cracks degrades the paste and separate it from aggregates.

The reduction in strength can be more extreme with DEF than with AAR.

It seems that the migration of moisture and leaching of alkalis needs to be considered in modelling both reactions. With the initial heat needed for DEF being confined on site to the core of the concrete, moisture takes time to penetrate and to trigger damage. Limiting moisture is the only means of slowing damage with both AAR and DEF.

Limiting cement contents is a cost effective and environmentally beneficial approach for preventing AAR, DEF and other cracking such as cracks due to thermal gradients.

The costs and disruption from damage to structures from AAR and DEF make reliable specification and quality control essential.

Acknowledgments

Mike Eden, Sandberg LLP, for petrographic thin section (Figures 1 and 2) and Renaud-Pierre Martin, IFSTTAR, for Figures 3 to 13.

References

[1] Nixon, P.J.; Sims, I. (2016) – Recommendations for prevention of damage from AAR in New Concrete structures RILEM TC 291-ACS Springer.

[2] Godart, B.; De Rooij, M.; Wood, J.G.M.(2013) – Guide to Diagnosis and Appraisal of AAR Damage to Concrete in Structures', RILEM AAR 6-1 Part 1 Diagnosis, Springer.

[3] Heinz, D.; Ludwig, U. (1987) – Mechanism of secondary ettringite formation in concrete subject to heat treatment ' J M Scanlon ed. 'Concrete Durability' SP100 ACI vol2 pp. 2059 -2071.

[4] Divet, L.; Guerrier, F.; Le Mestre, G. (1998) – Existe-t-il un risque d'attaque sulfatique endogène dans les pièces en béton de grande masse? Bull.des Laboratoires des Ponts et Chaussées, 213, p. 59-72.

[5] Divet, L. (2001) – Les reactions sulfatiques internes au béton: contribution à l'étude de la formation différée de l'ettringite. Etudes et Recherches des Lab. Ponts et Chaussées, OA 40, 227 p.

[6] Godart, B.; Divet, L. (2013) – Lessons learned from structures damaged by delayed ettringite formation and the French prevention strategy. Fifth international conference on Forensic Engineering, Institution of Civil Engineers, London, 15-17 April.

[7] Taylor, H.F.W.; Famy, C.; Scrivener, K. (2001) – Delayed Ettringite Formation Cement and Concrete Research 31, pp 683-693.

[8] Thomas, M.; Folliard, K. *et al.* (2008) – Diagnosing delayed ettringite formation in concrete structures. Cement and Concrete Research 38, pp.841–847.

[9] Martin, R.P.; Renaud, J.C.; Toutlemonde, F. (2010) – Experimental investigations concerning combined delayed ettringite formation and alkali aggregate reaction. 6th International conference on concrete under severe conditions CONSEC10, June, Mexico.

[10] Martin, R.P.; Renaud J.C.; Multon, S., Toutlemonde, F. (2012) – Structural behavior of plain and reinforced concrete beams affected by combined AAR and DEF. Proc. of the 14th International Conference on Alkali Aggregate Reaction, May 21-25, Austin, Texas.

[11] Pavoine, A.; Divet, L. (2007) – Réactivité d'un béton vis-à-vis d'une réaction sulfatique interne : Essai de performance. Techniques et méthodes des laboratoires des ponts et chaussées, Méthode d'essai ME66 - 19 p.

[12] Martin, R.P. (2010) – Analyse sur structures modèles des effets mécaniques de la réaction sulfatique interne du béton. PhD thesis, Université Paris-Est.

[13] Wood, J.G.M. (2004) – When does AAR Stop? Proceedings of 12th ICAAR, Beijing, Vol II, pp 1016-1024

[14] Martin, R.P.; Bazin, C.; Toutlemonde, F. (2012) – Alkali Aggregate Reaction and Delayed Ettringite Formation: common features and differences. Proc. of the 14th International Conference on Alkali Aggregate Reaction, May 21-25, Austin, Texas.

[15] Godart, B. (2017) – Pathology, assessment and treatment of structures affected by delayed ettringite formation. Structural Engineering International, Vol 27, Nr. 3, 2017, pp 362-369.

[16] Wood, J.G.M. (2018) – Living with AAR: An Engineer's Perspective. ICCRRR, Cape Town.

[17] Institution of Structural Engineers. (1992) – Structural effects of alkali-silica reaction. Technical guidance on the appraisal of existing structures. Report of an ISE task group, p. 48. SETO Ltd., London.

Diagnosis and prognosis of ASR in an airfield pavement

Diagnóstico e prognóstico da RAS no pavimento duma pista de aeroporto

Eric R. Giannini
April E. Snyder
Thanos Drimalas

Abstract

A concrete runway at an international airport began to exhibit multiple modes of distress several years after construction, including popouts, paste pop-offs, spalls, and cracking, prompting a root cause failure investigation. Both coarse aggregates used in construction were considered potentially reactive per the accelerated mortar bar test, and one of the three primary mixture designs did not use an SCM for mitigation. Based on petrographic findings of ASR in all three mixtures, a residual expansion testing program was initiated to investigate future expansion potential from ASR. This program included cores immersed in 1N NaOH at 38 °C and cores stored over water at 38 °C, monitored for up to fifteen months. The data indicate minimal risk of future expansion from ASR and the surface distresses were ultimately not attributed to ASR. This information will be valuable in designing an effective rehabilitation and repair strategy to extend the service life of the pavement.

Resumo

O pavimento de betão duma pista de um aeroporto internacional evidenciou alguns anos após a sua construção vários tipos de danos, incluindo cavidades, fendilhação e destacamentos de betão, o que conduziu a uma investigação sobre a origem das suas causas. Os agregados grossos usados na construção foram considerados potencialmente reativos pelo ensaio acelerado da barra de argamassa e uma das três composições de betão não incorporou adições minerais para a mitigação das reações expansivas. Com base nas evidências petrográficas da RAS nas três composições de betão, foram efetuados ensaios de expansão residual para avaliação do potencial residual devida à RAS. Estes incluíram imersão de carotes em NaOH 1N a 38 °C e ainda em ambiente saturado a 38 °C, que foram monitorizadas durante quinze meses. Os resultados indicaram um risco mínimo de expansão futura devida à RAS e as evidências à superfície não foram atribuídas à RAS. Esta informação será valiosa na definição de uma estratégia de reabilitação eficaz para prolongar a vida útil do pavimento.

Keywords: ASR / Failure analysis / Pavements / Petrography / Residual expansion

Palavras-chave: RAS / Análise de danos / Pavimentos / Petrografia / Expansão residual

Eric R. Giannini

RJ Lee Group
Monroeville, USA
egiannini@rjleegroup.com

April E. Snyder

RJ Lee Group
Monroeville, USA
asnyder@rjleegroup.com

Thanos Drimalas

The University of Texas at Austin
Austin, USA
thano.drimalas@utexas.edu

GIANNINI, E. [*et al*.] – Diagnosis and Prognosis of ASR in an Airfield Pavement. **Revista Portuguesa de Engenharia de Estruturas**. Ed. LNEC. Série III. n.º 15. ISSN 2183-8488. (março 2021) 35-44.

1 Introduction

A concrete runway constructed at a major international airport in the United States began to exhibit multiple modes of surface distress several years after construction. The types of distress observed included popouts, paste pop-offs, spalls, and cracking, and these increased in severity with time. RJ Lee Group was engaged with by owner in a root cause failure investigation starting in 2016 when the pavement was approximately 10 years old.

Surface distress of concrete airfield pavements is potentially a much more serious concern than for highways and local streets, because of the risk of foreign object debris (FOD). Concrete that is spalled from joints, cracks, and popouts in an airfield pavement is considered FOD, and could cause damage if ingested into aircraft engines. FOD can also be blown through the air by high-velocity jet blast, causing harm to nearby vehicles and personnel. The US Federal Aviation Administration (FAA), notes that pavement materials can be the most common source of FOD at airports [1].

Smith and Van Dam [2] provide several case studies of ASR-affected airfield pavements in the United States, including Phoenix Sky Harbor International Airport, Hartsfield Jackson Atlanta International Airport, Bangor (Maine) International Airport, and Colorado Springs Municipal Airport. The affected pavements at these airports included runways, taxiways, and aprons, and were constructed between the 1960s and 1990s using specifications with less-rigorous aggregate reactivity testing and without mitigating measures such as limits on cement alkali loading or the use of supplementary cementing materials (SCMs). Repair and remediation efforts including partial-depth and full-depth repairs, and overlays have been able to extend the service life of ASR-affected pavements, while crack sealing and surface treatments were found to be largely ineffective. Even low-severity cases that ultimately did not limit service life (35+ years before reconstruction) still produced FOD issues, while more severe cases were noted to significantly reduce service life, with reconstruction efforts at Colorado Springs beginning roughly 10 years after the pavements were constructed.

A review of the construction records found that the coarse aggregates were potentially reactive and that one of the three primary mixture designs used on the project did not contain any SCMs to mitigate against the risk of ASR. This raised the possibility that ASR could reduce the expected service life, and a laboratory investigation was initiated to first conduct petrographic examination of core samples extracted from the pavement, followed by residual expansion testing of additional core samples.

This paper focuses on the authors' application of petrography and residual expansion testing for diagnosis and prognosis purposes. The residual expansion testing program was influenced by the US Federal Highway Administration (FHWA) recommendations issued in 2010 [3] and the RILEM AAR-6.1 [4]. The petrographic investigation was used to evaluate whether ASR was present, whether it could be identified as a cause of the observed surface distress, and to provide a qualitative description of the severity of any reaction that had occurred to date. The residual expansion testing program would then be used to provide the owner with an estimate of future expansion potential of each concrete mixture, information that is critical to designing an effective rehabilitation and/or repair strategy for the runway.

2 Materials and methods

2.1 Materials and mixture designs

The initial investigation included a review of construction documents and submittals. The original coarse aggregate source was unable to supply the project for its full duration. As a result, coarse aggregate from a second source was procured for the remainder of the project. Because the coarse aggregate consistent of both a traditional coarse fraction (25 × 4.75 mm) and an intermediate (9.5 × 2.36 mm) size common to paving mixtures, this resulted in three primary mixture designs used for the construction of the runway. Table 1 provides details on the aggregates and cementitious materials and Table 2 summarizes the proportions for the three mixture designs. Coarse Aggregate 1 and Intermediate Aggregate 1 were from the same source, and Coarse Aggregate 2 and Intermediate Aggregate 2 were from the same source.

Table 1 Aggregates and cementitious materials

Material	Description	ASTM C1260 (14-day)
Coarse Aggregate 1	Mixed natural gravel (predominantly granitic and metasedimentary)	0.13%
Coarse Aggregate 2	Crushed porphyritic volcanic rock	0.16%
Intermediate Aggregate 1	Crushed stone; same mineralogy as Coarse Aggregate 1	0.14%
Intermediate Aggregate 2	Crushed stone; same mineralogy as Coarse Aggregate 2	0.19%
Fine Aggregate	Manufactured siliceous sand	0.05%
Cement	ASTM C150 Type II/V, Low-alkali, 0.59% Na2Oeq	N/A
Fly Ash	ASTM C618 Class F, 3.8% CaO	N/A

The US Federal Aviation Administration (FAA) specifications in force at the time of the project [5] relied upon the accelerated mortar bar test, ASTM C1260 [6], to determine aggregate reactivity, and a modified version of ASTM C1567 [7] with materials combined in job mixture proportions to evaluate mitigation measures. All coarse and intermediate aggregates had 14-day ASTM C1260 expansions greater than 0.10%, however petrographic descriptions of Coarse Aggregate 2 and Intermediate Aggregate 2 provided in construction documents indicated that material from that source was likely innocuous. The fine aggregate was from a third quarry and had a 14-day expansion below 0.10%.

Table 2 SSD Mixture proportions (all values in kg/m^3 unless noted) and ASTM C1567 results

Material	Mix 1	Mix 2	Mix 3
Coarse Aggregate 1	991	0	0
Coarse Aggregate 2	0	832	825
Intermediate Aggregate 1	186	322	0
Intermediate Aggregate 2	0	0	338
Fine Aggregate	695	685	679
Cement	356	297	297
Class F Fly Ash	0	74	74
Water	148	160	166
w/cm	0.42	0.43	0.45
14-day expansion, Modified ASTM C1567	N/A	0.02%	0.02%

The ASTM C1260 results should have necessitated the use of mitigation measures for all concrete mixtures, one of the primary mixtures (Mix 1) used on the project contained no mitigation measures. Mix 2 and Mix 3 each contained 20% fly ash (by mass of total cementitious materials). Documentation from the producer of Coarse Aggregate 1 and Intermediate Aggregate 1 did indicate that 14-day expansions in ASTM C1567 would be reduced to 0.02% with 15% fly ash, although it did not indicate what fly ash was used to achieve these results. The authors did not find records of modified ASTM C1567 tests for the full Mix 1 job mixture aggregate combination. Mix 2 and Mix 3 both had 14-day modified ASTM C1567 expansions of 0.02%, indicating that these mixtures should acceptably mitigate ASR risk per specification requirements. Concrete produced with Mix 1 was therefore considered to contain the highest risk of developing deleterious ASR in the field.

2.2 Field investigation

It is beyond the scope of this paper to describe all aspects of the investigation, which included numerous site visits by the authors and others in 2016 and 2017 to document the types and extent of distress on the runway, and to obtain core samples for laboratory testing. This section provides details of a targeted portion of the larger investigation, focused on determination of the potential effect of ASR on the remaining service life of the pavement.

The site visits were made at night due to limited opportunities for runway closures. Figure 1 and Figure 2 show examples of the different modes surface distresses, photographed during the initial documentation of the pavement condition. Construction records were also examined to map the locations of each mixture design along the runway. Subsequent site visits were primarily conducted for sample extraction purposes.

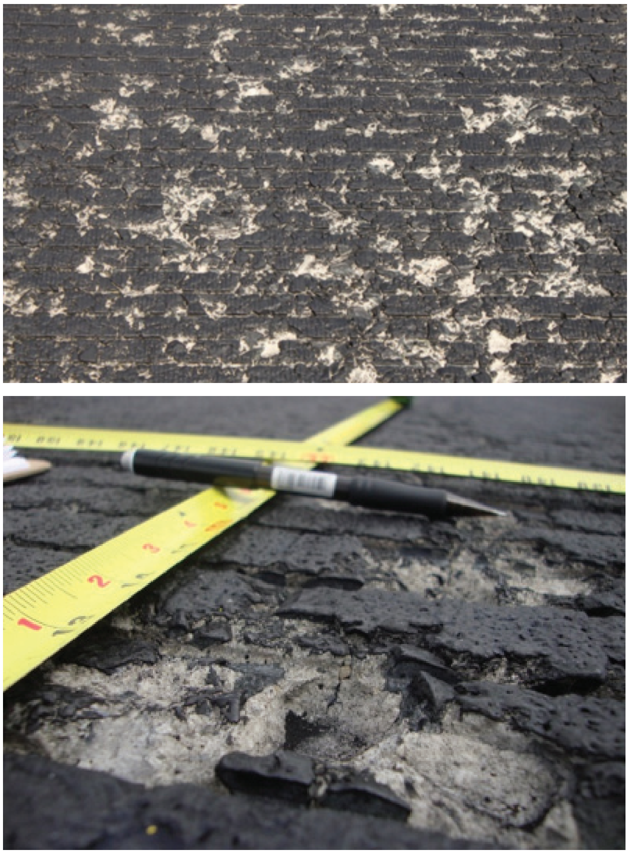

Figure 1 Examples surface distress (popouts and loss of paste)

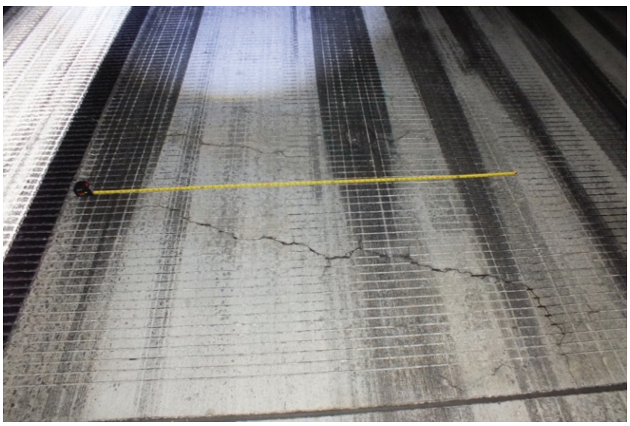

Figure 2 Example of surface cracking

2.3 Laboratory investigation

2.3.1 Petrography

Petrographic examinations following ASTM C856, *Standard Practice for Petrographic Examination of Hardened Concrete* [8] and ASTM C1723 *Standard Guide for Examination of Hardened Concrete Using Scanning Electron Microscopy* (SEM) [9] were conducted on concrete representing all three mixture designs over the course of the root cause investigation. Cores were visually examined in the as-received condition and using a binocular microscope at magnifications up to 50x. The core was then cut at a depth of 100 mm from the top of the core using a table-top masonry saw with a 355-mm diamond blade. Based on the visual observations, the top and bottom portions of the core were then cut at select locations to create two 12.7-mm-thick cross-sectioned slabs which were polished using successively finer silica carbide abrasives to 1000 grit size creating a finish satisfactory for microscopical examination showing excellent reflection of a distant light source when viewed at a low incident angel, and no noticeable relief between paste and aggregate surfaces. These polished cross sections were examined using stereo-optical microscope at magnifications up to 50×.

Figure 3 Photograph of cross-sectioned core showing locations of thin section preparation outlined in black

Three to four thin sections were prepared from select locations on the opposing slab to examine the concrete microstructure at various depths as indicated in the photographs in Figure 3. The thin sections were prepared from a 44 mm × 29 mm × 10 mm block that was vacuum-impregnated with fluorescent-dyed epoxy and mounted onto a glass slide. The thin sections were created to a thickness of 20 to 25 μm using a Pelcon automatic thin section machine. The final polish was completed manually with a 0.25 μm diamond oil to result in a highly polished surface for analysis. Thin sections were examined using polarized light microscopy (PLM) in plane-polarized and cross-polarized light modes at magnifications from 10× to 200×, and using reflectance fluorescent light at magnifications of 10x to 40×. The thin sections were finally examined using scanning electron microscopy with energy dispersive X-ray spectroscopy (SEM/EDS) on an ASPEX Personal SEM at magnifications of 20× to 2000×.

2.3.2 Residual expansion

Specimen preparation and testing for residual expansion primarily followed the procedures given in Appendix F of Fournier *et al.* [3], with slight variations. Cores were extracted from three locations of interest for each of the three mixture designs, with one 150-mm diameter core and two 50-mm diameter cores taken adjacent to each other from each location. All cores were drilled to the full depth of the pavement (approximately 480 mm), wiped of excess water, labelled, and wrapped in plastic bags for shipment to RJ Lee Group's laboratory. The top 50 mm of each core was sawn off to exclude near-surface effects and was retained for additional petrographic examination at RJ Lee Group. The 150-mm diameter cores were cut to a length of 300 mm for testing and the 50-mm diameter cores were cut to a length of 200 mm. The cut cores were then shipped to The University of Texas at Austin for instrumentation and residual expansion testing.

Two test procedures were conducted in parallel to evaluate the residual expansion potential of all three mixture designs. The first test procedure involved storing the 150-mm diameter cores over water (> 95% relative humidity) at 38 °C. The second test procedure involved storing the 50-mm diameter cores in 1N NaOH solution at 38 °C.

The DEMEC Mechanical Strain Gauge system [10], widely used for *in-situ* monitoring of ASR-affected structures as described in [3], was adapted to measure residual expansion of the cores. DEMEC target discs (a.k.a. DEMEC points) were affixed to the sides of the cores in pairs so as to provide three 150-mm gauge lengths for axial expansion measurements. The gauge lengths were set at increments of approximately 120° rotation. This instrumentation method was selected to avoid the risk of damage caused by drilling into the ends to install gauge studs. The 150-mm gauge length was selected for commonality and to ensure that the DEMEC target discs were located at least 25 mm from each end of the core. Expansion measurements were made to the nearest 0.001 mm and specimens were also weighed at the time of each expansion measurement (nearest 0.1 g for the 50-mm diameter cores and nearest 0.02 kg for the 150-mm cores). The expansions of all three gauge lengths on each core were averaged to account for any warping that might occur.

An initial conditioning period was required to allow the cores to reach initial moisture saturation (hygrometric equilibrium, according to [3]). Following RILEM AAR-6.1 recommendations, a reduced temperature of 23 °C was used for the initial conditioning period [4]; this is intended to avoid promoting further development of ASR until after the cores reached saturation. During this period, frequent measurements were taken to monitor the swelling from moisture uptake and note when this ceased; at this point the specimens would be placed in 38 °C storage. The initial conditioning period lasted six days for the 50-mm cores stored in 1N NaOH, and between 50 and 54 days for the 150-mm cores stored over water. Specimens were pre-cooled to 23 °C for 20 ± 4 hours prior to subsequent measurements, which were made initially at weekly intervals, and then less frequently as the testing progressed. Testing continued to between 315 and 351 days for the 50-mm cores in 1N NaOH, and to between 420 and 456 days for the 150-mm cores over water.

3 Results

3.1 Petrography

Petrographic evaluation of the cores representing the three different mixture designs verified that the concrete placed were generally consistent with the mixture designs described in project submittal documents. Visual examination of the cores received at the laboratory after air drying revealed that the cores extracted from Mix 1, which contained the natural gravel coarse aggregate (Coarse Aggregate 1 and Intermediate Aggregate 1) and no SCMs, exhibited damp patches or wet rims around coarse aggregate particles (Figure 4), a characteristic that is indicative of ASR [3]. Thin section evaluation using SEM/EDS confirmed the presence of slight-to-minor ASR; examples are shown in Figure 5. This primarily occurred within metagranite grains containing strained quartz (Figure 6), although a trace amount of rhyolite with amorphous or microcrystalline quartz was present in the aggregate population and also exhibited ASR.

Figure 4 Photograph of air dried core from Mix 1, showing wet rims around coarse aggregate indicative of ASR.

Damage due to ASR in Mix 1 concrete was minor with ASR gel formation mostly confined within cracks in the aggregate particles, in adjacent air voids, or extending out into the paste to a limited extent and sometimes bridging aggregates. The natural gravel aggregate was from an alluvial deposit containing a variety of rock types. In addition to those currently identified as alkali-silica reactive, metamorphosed sedimentary rocks and volcanics were present in the aggregate. The abundance of potentially reactive silica in the form of strained quartz and microcrystalline quartz within the aggregate population warranted further investigation into the potential for future expansion.

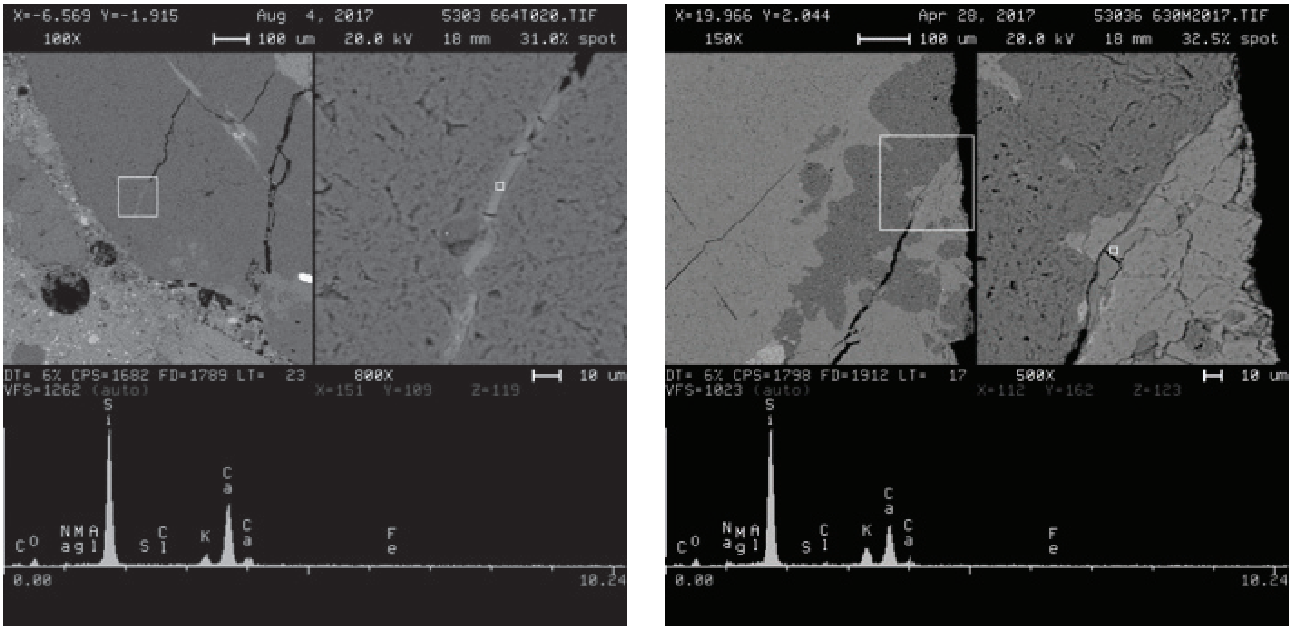

Figure 5 Backscattered electron (BSE) images with EDS spectra of ASR gel within cracks in Coarse Aggregate 1

Microscopic examination of concretes from Mix 2 and Mix 3 showed that the crushed volcanic coarse aggregate (Coarse Aggregate 2 and Intermediate Aggregate 2) also showed slight or innocuous ASR of amorphous and microcrystalline quartz. The reaction was less common in this aggregate type than observed in the natural gravel (Coarse/Intermediate 1). The ASR gel formation was generally confined within cracks in the aggregate particles and adjacent air voids, with little-to-no cracking into the paste. Concrete in core samples from Mix 2 which contained both the crushed volcanic coarse aggregate and crushed natural gravel showed more significant ASR than concrete in core samples from Mix 3, which only contained the crushed volcanic rock type (Coarse/Intermediate 2). The majority of ASR in cores from Mix 2 was detected in the Intermediate Aggregate 1. Only a trace amount of ASR gel within pockets inside of aggregate particles was found in Mix 3 cores; examples are presented in Figure 7.

The surface distresses in the pavement which had prompted the investigation were not linked to ASR in any of the cores. The majority of ASR was found in the middle and bottom of the cores, resulting in microcracks within the aggregate, and was only detected using SEM/EDS.

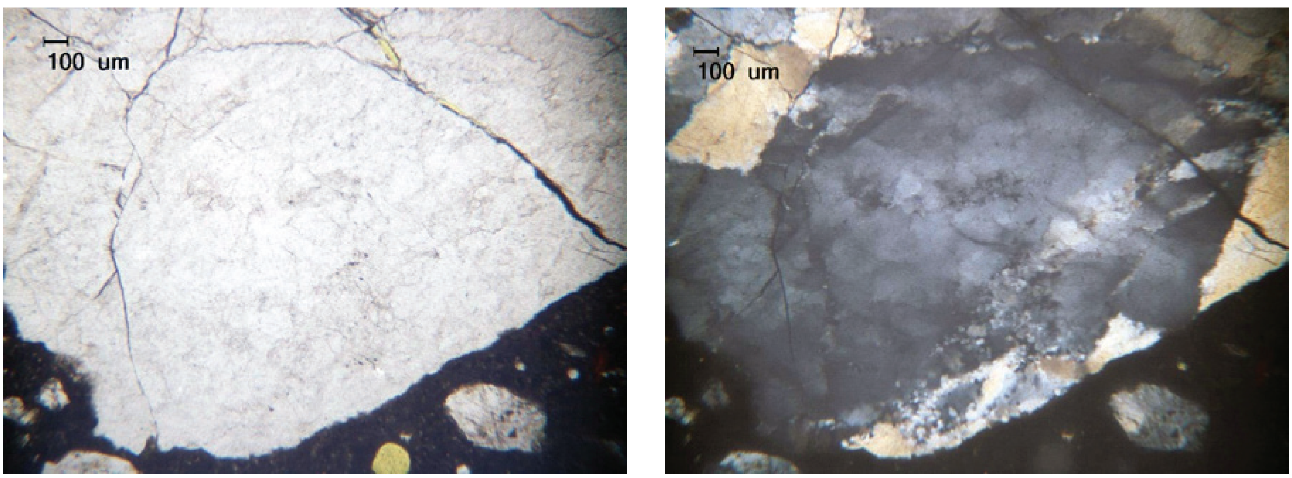

Figure 6 Polarized light micrographs in different light modes of reactive metagranite containing strained quartz found in Coarse Aggregate 1 and Intermediate Aggregate 1

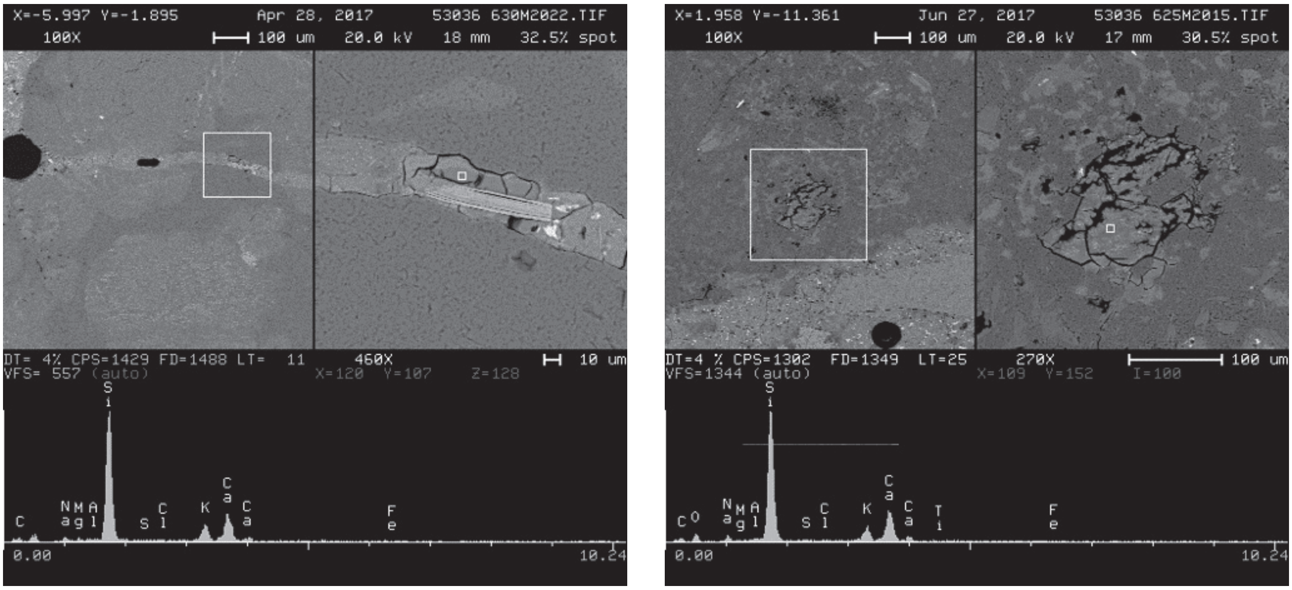

Figure 7 Backscattered electron (BSE) images with EDS spectra of ASR gel within pockets in Coarse Aggregate 2

3.2 Residual expansion

Figure 8 and Table 3 present the results of the residual expansion testing of 50-mm diameter cores in 1N NaOH at 38 °C; expansions are presented as average values for the three gauge lengths on each core. Figure 8 contains plots of the raw expansion, mass change, and adjusted expansion versus time. The adjusted expansions were calculated by subtracting the raw expansions at 6 days, to account any swelling during the initial conditioning period. Table 3 presents both the final raw and adjusted expansions at 351 days (315 days for

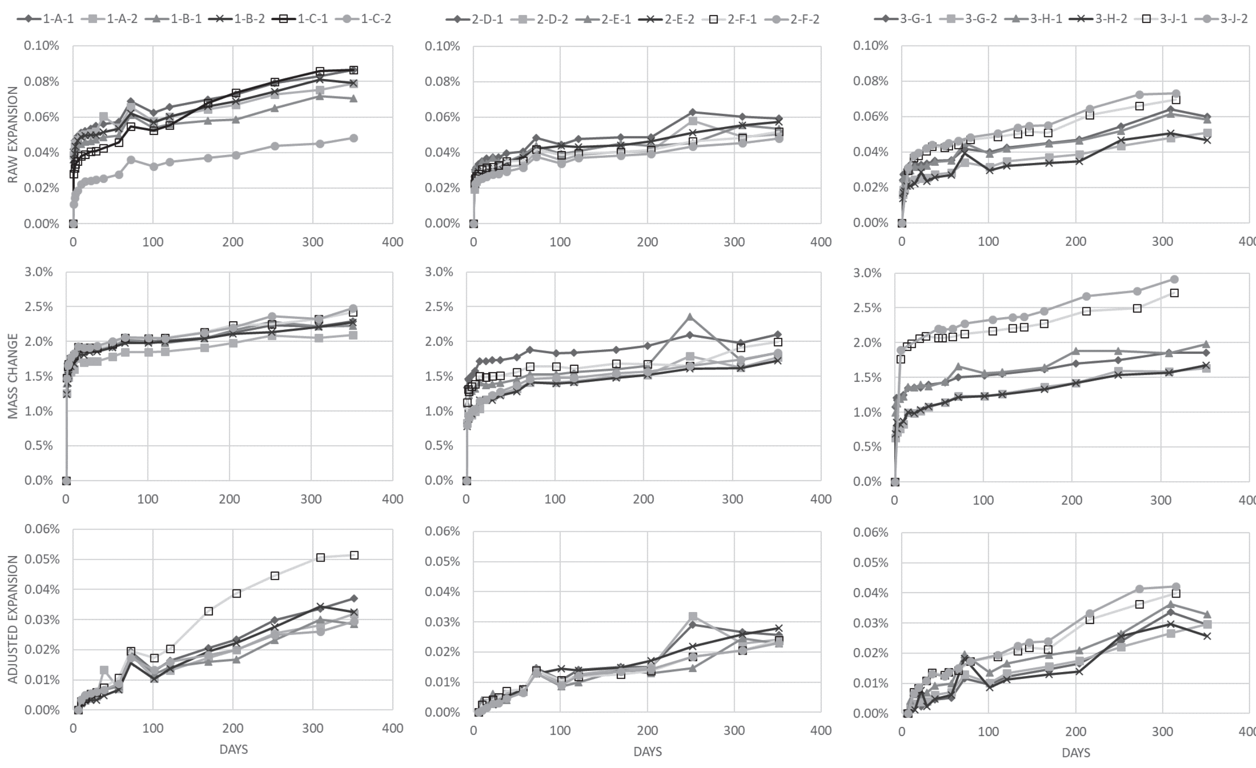

Figure 8 Raw expansion, mass change, and adjusted expansion for 50-mm diameter cores stored in 1N NaOH at 38 °C

3-J-1 and 3-J-2) and the expansion measured over the final 99 days of monitoring.

Adjusted final expansions ranged from 0.023% to 0.051%, while expansions over the final three months ranged from -0.008% to 0.009%. While some slight expansion and mass gain were continuing for most specimens when residual expansion testing concluded, there was no indication that the rate of increase was accelerating for either property.

Table 3 Expansion Details of 50-mm Cores (1N NaOH at 38 °C)

Mix	Location	Core	Days in NaOH	Average rawfinal expansion	Adjusted final expansion	Expansion overfinal 99 days
1	A	1	351	0.086%	0.037%	0.007%
		2	351	0.079%	0.032%	0.004%
	B	1	351	0.070%	0.028%	0.005%
		2	351	0.079%	0.032%	0.005%
	C	1	351	0.086%	0.051%	0.006%
		2	351	0.048%	0.029%	0.004%
2	D	1	351	0.059%	0.025%	-0.004%
		2	351	0.050%	0.024%	-0.008%
	E	1	351	0.054%	0.023%	0.009%
		2	351	0.057%	0.028%	0.006%
	F	1	351	0.052%	0.024%	0.006%
		2	351	0.048%	0.023%	0.005%
3	G	1	351	0.060%	0.030%	0.006%
		2	351	0.051%	0.030%	0.008%
	H	1	351	0.051%	0.026%	0.006%
		2	351	0.047%	0.026%	0.000%
	J	1	315	0.070%	0.027%	0.009%
		2	315	0.073%	0.028%	0.009%

Figure 9 and Table 4 present the results of the residual expansion testing of 150-mm diameter cores over water at 38 °C; expansions are presented as average values for the three gauge lengths on each core. Figure 9 contains plots of the raw expansion, mass change, and adjusted expansion versus time. The adjusted expansions were calculated by subtracting the raw expansions at 50 days (54 days for core 3-J), to account any swelling during the initial conditioning period. The end of the initial conditioning period is marked with a vertical line in the plots of raw expansion and mass change. Table 4 presents both the final raw and adjusted expansions at 456 days (420 days for core 3-J) and the expansion measured over the final 105 days of monitoring.

Adjusted final expansions ranged from 0.005% to 0.009%, while expansions over the final three months ranged from 0.000% to 0.002%. The expansion and mass change trends over the final three months of monitoring indicate that both properties had essentially stabilized at the end of the testing.

Table 4 Expansion Details of 150-mm Cores (Over Water at 38 °C)

Mix	Location	Days over water	Average raw final expansion	Adjusted final expansion	Expansion over final 105 days
1	A	456	0.027%	0.006%	0.001%
	B	456	0.029%	0.006%	0.002%
	C	456	0.031%	0.007%	0.001%
2	D	456	0.023%	0.006%	0.000%
	E	456	0.027%	0.009%	0.001%
	F	456	0.021%	0.006%	0.000%
3	G	456	0.019%	0.007%	0.001%
	H	456	0.020%	0.008%	0.001%
	J	420	0.017%	0.005%	0.001%

Table 5 presents a summary of the average results by concrete mixture. In the 1N NaOH test, Mix 1 cores expanded the most with an average adjusted expansion of 0.035% per core, while Mix 2 cores expanded the least, with an average adjusted expansion of 0.025% per core. The average adjusted expansions over water similar for the three mixtures, with Mix 1 cores expanding an average of 0.006% and Mix 2 and Mix 3 cores both expanding an average of 0.007%.

Table 5 Adjusted Expansion Summary

Mixture Design	50-mm Cores in NaOH	150-mm Cores over Water
Mix 1	0.035%	0.006%
Mix 2	0.025%	0.007%
Mix 3	0.028%	0.007%

The averaged results for each mixture were then used as inputs to assess the overall potential for future expansion following the methodology described by Bérubé et al. [11] and recommended by the US FHWA [3]. The 1N NaOH test results were used to determine residual aggregate reactivity (RAR), while the over-water test results

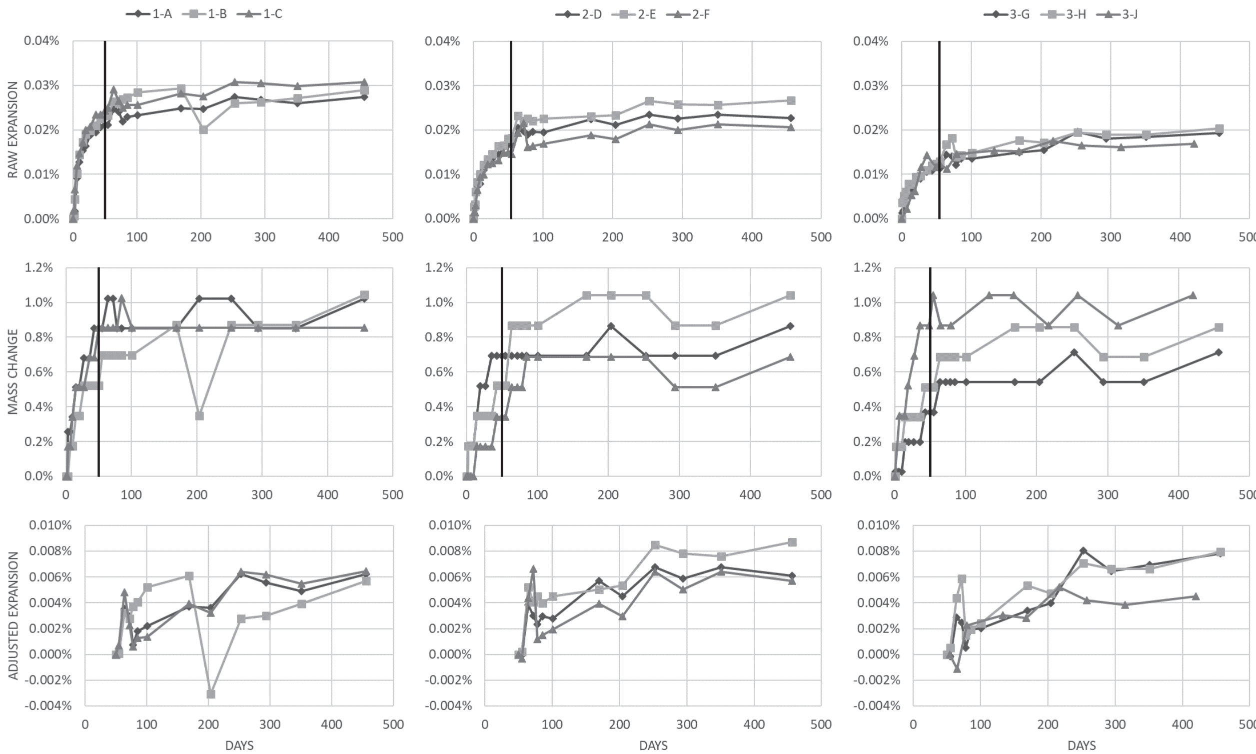

Figure 9 Raw expansion, mass change, and adjusted expansion for 150-mm diameter cores stored over water at 38 °C.

were used to determine residual concrete reactivity (RCE). Because all three mixtures had average expansions in NaOH below 0.04%, the RAR coefficient was 0 (negligible). The over-water expansions, however, indicated a low, but not negligible potential, and were assigned an RCE coefficient of 2.

This methodology also uses the effects of ambient conditions (humidity and temperature), confinement (reinforcement or external restraint), and available alkali loading. A humidity coefficient (HUM) of 1.0 was selected based on the pavement thickness, exposure to rain, and contact with the ground. An average annual air temperature of 17 °C resulted in a temperature coefficient (TEM) of 0.7. A structural confinement coefficient (STR) of 1.0 was conservatively chosen; the pavement is unreinforced, but pavements are still typically subject to some lateral confinement, which would yield a lower STR value. The investigation intended to include pore solution analysis to measure available alkalis, but it was not possible to extract sufficient pore solution from crushed samples. The alkali loading coefficient (ALK) was thus estimated from the mixture proportions and an assumption that 60% of the cement alkalis would be available. Some mill certificates were available, but given expected variability in materials, a slightly higher assumed Na_2O_{eq} of 0.60% was used. This resulted in available alkali loadings of 1.28 kg/m^3 for Mix 1 and 1.07 kg/m^3 for Mixes 2 and 3, and an ALK coefficient of 1 (low) for all three mixtures.

The future expansion potential was calculated as a current rate of expansion (CRE) using equations (1) and (2) as follows:

$$\text{CRE} = [\text{RAR} \times \text{ALK}] \times \text{HUM} \times \text{TEM} \times \text{STR} \tag{1}$$

$$\text{CRE} = \text{RCE} \times \text{HUM} \times \text{TEM} \times \text{STR} \tag{2}$$

Equation 1 yields a CRE value of 0 for all three mixtures as a result of the negligible RAR coefficient and Equation 2 yields a CRE value of 1.4 for all three mixtures. The CRE values obtained from this methodology are qualitative in nature and correspond to a negligible-to-low continuing rate of expansion from ASR in the pavement for all three mixtures, including Mix 1 that did not contain fly ash for mitigation.

Long-term monitoring of the pavement could more conclusively establish the progression of ASR, but the combined assessment of the petrographic and residual expansion investigations is that the limited amount of ASR present was not the cause of the observed surface distresses and there is at most, a low potential for continuing expansion. Given that testing with 1N NaOH exposure is more severe, yet it yielded a lower CRE rating than testing over water, the risk of deleterious expansion and resulting damage to the pavement is deemed to be minimal at this time.

4 Conclusions

An airfield pavement exhibiting several forms of surface distress and containing potentially reactive aggregates was the subject of an extensive root-cause failure analysis investigation. One focus of this investigation was to determine whether ASR was present and if so, its severity and potential to cause future distress in the pavement. The following conclusions were drawn from the petrographic and residual expansion investigations, which included petrographic examination of more than 100 core samples and residual expansion testing of 27 core samples:

- Petrographic examination of core samples found the presence of ASR in concrete from all three mixture designs used in the construction of the pavement, but not linked to the surface distresses observed in the field investigation.
- The severity of ASR was qualitatively determined to be negligible-to-slight, and more prevalent in the gravel aggregate (Coarse/Intermediate 1) than the crushed volcanic stone (Coarse/Intermediate 2).
- Residual expansion testing of cores in 1N NaOH at 38 °C indicated a negligible potential for future expansion, while testing over water at 38 °C indicated a low potential for future expansion.
- The combined assessment is that there is only a minimal risk of deleterious expansion from ASR in the pavement, although long-term monitoring could provide more conclusive data. Repair and/or rehabilitation decisions are likely to be primarily driven by the severity and progression of the unrelated surface distresses.
- Two key differences from the FHWA-recommended procedures in [3] for residual expansion testing of cores were employed in this study and are recommended for future use: (1) An initial conditioning temperature of 23 °C while the core samples reached hygrometric equilibrium, as recommended in RILEM guidance [4], may reduce the chances of concurrent swelling from re-saturation and ASR; (2) Pre-cooling of cores to 23 °C for expansion measurements also reduced the potential measurement errors caused by thermal expansion and contraction and avoids the need for temperature corrections to measurements made in the initial conditioning period.

References

[1] Federal Aviation Administration (2010) – Airport Foreign Object Debris (FOD) Management. Advisory Circular 150/5210-24. US Department of Transportation, Washington, DC.

[2] Smith, K.D.; Van Dam, T.J. (2019) – Practices to Mitigate Alkali-Silica Reaction (ASR) Affected Pavements at Airports. ACRP Synthesis 96. National Academies of Science, Engineering, and Medicine, Washington, DC. https://doi.org/10.17226/25553

[3] Fournier, B.; Bérubé, M.A.; Folliard, K.J.; Thomas, M. (2010) – Report on the diagnosis, prognosis, and mitigation of alkali-silica reaction (ASR) in transportation structures. Report No. FHWA-HIF-09-004. Federal Highway Administration, Washington, DC.

[4] Godart, B.; de Rooij, M.; Wood, J.G.M. (2013) – Guide to diagnosis and appraisal of AAR damage to concrete structures, Part 1: diagnosis (RILEM AAR-6.1). RILEM state-of-the-art report. Springer, Dordrecht. https://doi.org/10.1007/978-94-007-6567-2

[5] Federal Aviation Administration (2005) – Standards for Specifying Construction of Airports. Advisory Circular 150/5370-10B. US Department of Transportation, Washington, DC.

[6] ASTM C1260-14 (2014) – Standard Test Method for Potential Alkali-Silica Reactivity of Aggregates (Mortar-Bar Method). ASTM International, West Conshohocken. https://doi.org/10.1520/C1260-14

[7] ASTM C1567-13 (2013) – Standard Test Method for Determining the Potential Alkali-Silica Reactivity of Combinations of Cementitious Materials and Aggregates (Accelerated Mortar-Bar Method). ASTM International, West Conshohocken. https://doi.org/10.1520/C1567-13

[8] ASTM C856-14 (2014) – Standard Practice for Petrographic Examination of Hardened Concrete. ASTM International, West Conshohocken. https://doi.org/10.1520/C0856-14

[9] ASTM C1723-16 (2016) – Standard Guide for Examination of Hardened Concrete Using Scanning Electron Microscopy. ASTM International, West Conshohocken. https://doi.org/10.1520/C1723-16

[10] http://www.mayes.co.uk/6.html

[11] Bérubé, M.A.; Frenette, J.; Pedneault, A.; Rivest, M. (2002) – Laboratory assessment of the potential rate of ASR expansion of field concrete. Cement, Concrete, and Aggregates 24(1):13-19. https://doi.org/10.1520/CCA10486J

Residual load carrying capacity of ASR damaged reinforced concrete beam after 12 years exposure

Capacidade de carga residual de viga de betão armado danificada pela RAS após 12 anos de exposição

Susumu Inoue

Abstract

After the reports on the rupture of stirrups and longitudinal steels in T-shaped beams of bridge piers mainly due to ASR expansion, concentrated researches had been done in Japan. In this paper, load carrying behaviour of an ASR damaged reinforced concrete beam with a large cross section (600 mm-square) after 12 years exposure is discussed.

The specimen was cut into 3 pieces after the loading test at the positions where the effect of loading test could be eliminated, and expansive crack propagation inside the concrete was observed. In addition, the effect of anisotropy of ASR expansion on the mechanical properties of inner concrete was examined.

Test results indicated that the residual capacity of the ASR damaged beam well exceeded the design value because the rupture of stirrups did not occur during the exposure period. In addition, compressive strength of core concrete was affected by the anisotropy of ASR expansion.

Resumo

Após casos de rotura de estribos e armaduras longitudinais em vigas T de pontes devido principalmente à expansão por RAS, no Japão desenvolveram-se pesquisas específicas sobre este tema. Neste artigo apresenta-se e discute-se o comportamento de uma viga carregada de betão armado, com uma grande secção transversal (600 mm quadrados), danificada pela RAS após 12 anos de exposição.

Após o ensaio de carga, a viga foi cortada em 3 peças, em zonas em que os efeitos do ensaio de carga pudessem ser eliminados, sendo observada a propagação das fendas no betão. Foi também avaliado o efeito da anisotropia da expansão devida à RAS nas propriedades mecânicas do betão.

Os resultados dos ensaios indicaram que a capacidade residual da viga danificada pela RAS excedeu em muito o valor de projeto porque a rotura dos estribos não ocorreu durante o período de exposição. Além disso, a resistência à compressão do betão do núcleo foi afetada pela anisotropia da expansão devida à RAS.

Keywords: Anisotropy of expansion / ASR damage / Compressive strength / Crack propagation / Residual capacity

Palavras-chave: Anisotropia de expansão / Dano pela RAS / Resistência à compressão / Propagação de fendas / Capacidade residual

Susumu Inoue

Osaka Institute of Technology
Osaka, Japan
susumu.inoue@oit.ac.jp

INOUE, S. – Residual load carrying capacity of ASR damaged reinforced concrete beam after 12 years exposure. **Revista Portuguesa de Engenharia de Estruturas**. Ed. LNEC. Série III. n.º 15. ISSN 2183-8488. (março 2021) 45-54.

1 Introduction

In the last two decades, vigorous research works have been done on the structural effects of ASR expansion, for example, by Multon et al. [1]. While in Japan, it was reported in the early years of the 21st century that stirrups, as well as longitudinal steels, in T-shaped beams of reinforced concrete bridge piers were ruptured at the bent corner or butt joints. In order to make clear the causes of this rupture, concentrated researches had been done after the finding of the rupture in existing reinforced concrete structures. These researches concluded that this phenomenon occurred not only due to excessive ASR expansion but also under complex combinations of several factors, such as mechanical properties and surface shape of reinforcing bars, bending or welding methods of reinforcing bars, corrosive atmospheres and so on [2]. As for the load carrying capacity of ASR damaged structures, on the other hand, it is indicated that in most cases structural safety of damaged members is guaranteed at the present stage as far as the anchorage of ruptured steels is maintained by the bond between concrete and reinforcing bars, based on the site inspections of the damaged structures as well as some experimental and analytical investigations [2].

The author also reported on the residual shear capacity of ASR damaged reinforced concrete beams with ruptured stirrups at the 13th [3] and 14th ICAAR [4]. The main conclusions of these studies are as follows. 1) The introduced chemical prestress due to ASR expansion increased the concrete shear capacity. This positive effect was rather larger compared with the negative effect of the deterioration in material properties. 2) As for the effects of rupture of stirrups, the ruptured stirrups could not effectively restrain the ASR expansion in vertical direction and the dowel force of the longitudinal bars at the shear cracks, resulting in the significant propagation of the shear bond cracks along with the longitudinal bars. Such shear bond cracks might lead to the premature shear bond failure even when the ruptured stirrups carried some parts of the applied shear force just before the failure.

However, these were based on the test results of relatively small specimens after the exposure of up to 3 years. In addition, rupture of stirrups was imitated by cutting the bent corner of them beforehand. Therefore, it is important to examine whether rupture of stirrups occurs in the beam during long-time exposure. Information on residual capacity after long-time exposure as well as the effect of anisotropic expansion in concrete structures on mechanical properties of concrete is also useful for rational countermeasures against ASR damaged structures.

In this paper, load carrying behaviour of an ASR damaged reinforced concrete beam with a relatively large cross section (600 mm-square) is discussed. This specimen was exposed to natural outside condition for almost 12 years. After the loading test, this specimen was cut into 3 pieces at the positions where the effect of loading test could be eliminated, and expansive crack propagation inside the concrete was observed. In addition, the effect of anisotropy of ASR expansion on the mechanical properties of internal concrete is examined by using concrete core specimens.

2 Outline of tests

The specimen used was a reinforced concrete beam with width × full depth × total length of 600 × 600 × 4000 mm as shown in Figures 1 and 2. Sixteen D22 reinforcing bars (f_{sy} = 385N/mm^2) were used for longitudinal reinforcement (tensile reinforcement ratio p = 1.99%) and D13 stirrups (f_{sy} = 328 N/mm^2) were used for shear reinforcement (shear reinforcement ratio p_w = 0.40%). This beam was designed to fail in shear in order to evaluate the effectiveness of stirrups within ASR damaged concrete. Two kinds of bending radius for stirrups, 2.0 ϕ and 1.0 ϕ (ϕ: bar diameter), were selected in order to examine the effect of bending radius on the rupture of stirrups during exposure period. This is because many of the practically ruptured stirrups had smaller bending radius less than 2.0 ϕ. The design compressive strength of concrete was 24 N/mm^2. The mix proportion of used reactive concrete is shown in Table 1, in which that of non-reactive normal concrete (N) is also indicated for comparison. Reactive fine and coarse aggregates, which are categorized as one of andesite and judged as “not harmless” by JIS A 1145 “Method of test for alkali-silica reactivity of aggregates by chemical method” [5], were used in the pessimum (approximately 50% by weight) for the concrete. Sodium chloride (NaCl) was also added so that the total alkali contents might become 8 kg/m^3.

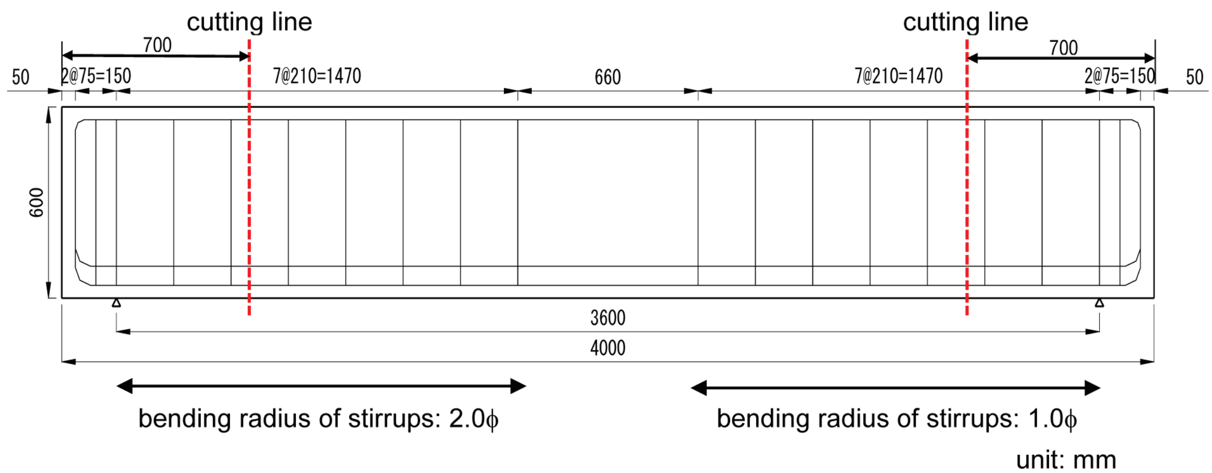

Figure 1 Reinforcing details of specimen

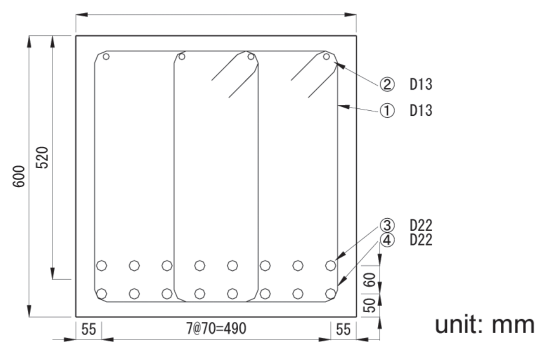

Figure 2 Cross section

Table 1 Mix proportions of concrete

Type	G_{max} (mm)	Slump (cm)	Air (%)	W/C (%)	s/a (%)	Unit weight (kg/m^3)							Water Reducing Agent (cc/m^3)
						W	C	S normal	S reactive	S normal	S reactive	NaCl	
N	25	12	4.5	63	45.8	183	290	840	–	1080	–	–	726
ASR	25	12	4.5	63	45.8	183	290	394	411	507	492	13.1	726

This beam was exposed to outside natural environment but off the ground for 4495 days (more than 12 years) after casting of concrete as shown in Figure 3. During the exposure, it was simply supported and subjected to the stress caused by its own weight. During the last 5 years of exposure, the temperature range was – 4.8 to 39.6 degree centigrade and the average was 16.4 degree centigrade, while the average relative humidity was about 72.5%. During the exposure, changes in the vertical, horizontal and longitudinal strain of the concrete surface and ultrasonic pulse velocity were measured in addition to the observation of crack propagation.

Figure 3 Exposed specimen (at the age of 1.5 years)

After the exposure, the beam was loaded monotonously up to failure under symmetrical two-point loads (shear span: 990 mm, flexural span: 1520 mm). The shear span - effective depth ratio (a/d) was set as 1.9 so that the effect of shear force might become dominant. During the loading test, applied load, deflections at the mid span and the loading points were recorded. In addition, the propagation of cracks during loading was observed.

3 Results and discussions

3.1 Expansion characteristics during exposure period

3.1.1 Expansion characteristics

Figure 4 shows the expansive crack profiles after the exposure of 491 and 4495 days. As seen in this figure, the density of expansive cracks in the upper and side surfaces, as well as the width of existing cracks, increased during this period. In addition, longitudinal cracks along with the tensile reinforcement developed remarkably.

Figure 5 shows the changes in concrete strain used for the beam, in which the values of non-reactive normal concrete having the same W/C ratio are also indicated for comparison. These strains were measured using 100 × 100 × 400mm concrete prisms exposed to the same environment as the beam specimen. Figure 6 shows the changes in concrete surface strain of the beam, in which the horizontal strain in the upper surface, the vertical ones in the side surfaces and the longitudinal ones (upper: 80mm from the top fibre, lower: 80mm from the bottom fibre) in the side surfaces are indicated. All of these values are the average ones obtained from several measuring points. Although no measurement was done between 3 and 12 years, the accuracy of the measured values after 12 years exposure was guaranteed because these values were calculated from the elongations measured mechanically between two contact tips embedded in the concrete.

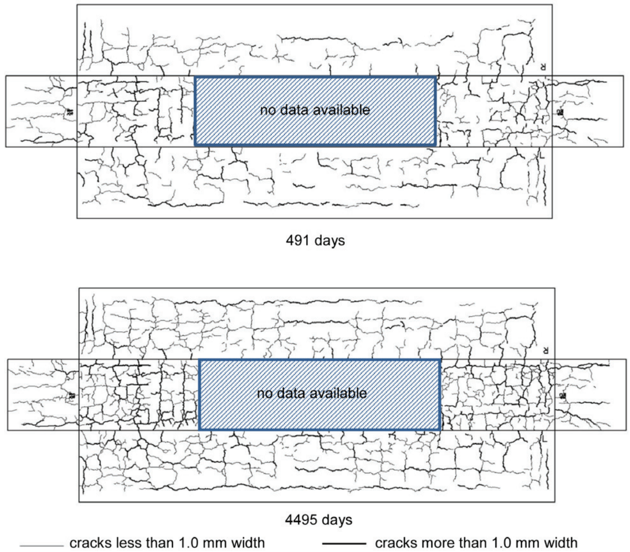

Figure 4 Expansive cracking patterns of the beam

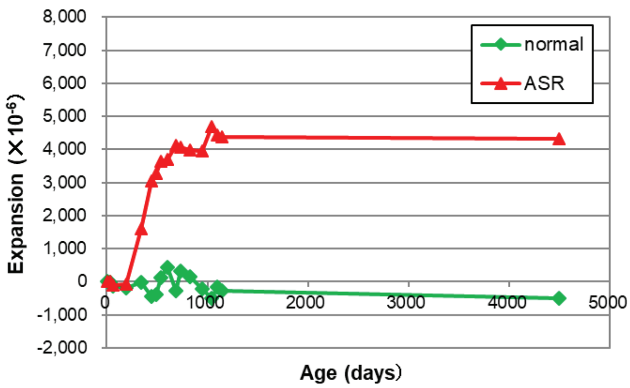

Figure 5 Changes in expansive strain of used concrete

As seen in Figure 5, ASR expansion at the end of exposure was approximately 4300 × 10^{-6} and no increase was observed from the age of 1150 days (about 3 years). This implies that expansion of used concrete almost finished. The same tendency was observed in the horizontal strain of the upper surface of the beam as seen in Figure 6. On the other hand, however, vertical strains in the side surfaces as well as upper longitudinal ones increased further from the age of 1150 days. This was mainly due to the increase in crack width of the existing expansive cracks (creep) caused by the eccentric chemical prestress. The influence of reinforcement corrosion on the increase in crack width was also considered. From the strain distribution in the cross section, the introduced chemical prestress was estimated and it became approximately 6.5 N/mm^2 at the bottom fibre.

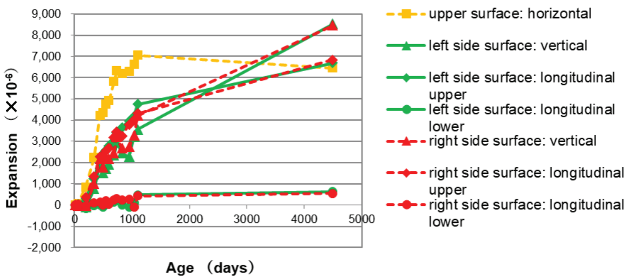

Figure 6 Expansion of concrete surface of the beam

3.1.2 Ultrasonic pulse velocity

In Figure 7 are shown the changes of ultrasonic pulse velocity in the beam during the exposure period. It is indicated that the value of the ultrasonic pulse velocity decreased to almost the half of its initial value at the age of about 1000 days. After that, however, the values restored at the end of exposure irrespective of the measured positions. The same tendency was also reported by Siegerd et al. [6]. From this result, re-filling of micro cracks and pores by alkali-silica gel might occur. The value at the end of exposure became the largest in side upper and the smallest in side lower. This can be related to the density and the maximum width of expansive cracks depending on temperature, relative humidity, rainfall as well as local chemical prestress. Minute cracks were dominant in side upper while relatively wider ones were dominant in side lower, and this might led to the difference in re-filling by alkali-silica gel.

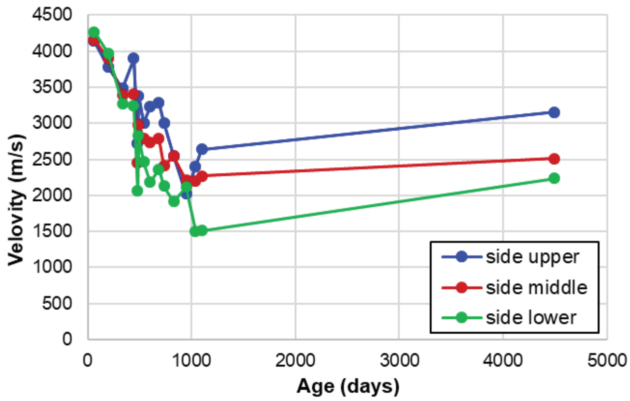

Figure 7 Changes in ultrasonic pulse velocity

3.1.3 Mechanical properties of concrete

In Table 2 are listed the compressive strength and the elastic modulus of used concrete obtained from the test specimens (ϕ 100 mm × 200 mm cylinders) exposed under the same condition as the beam. These values are the average ones obtained from at least 3 specimens, and significant scatter was not observed among those specimens.

The elastic modulus of the reactive concrete decreased remarkably at the age of 491 days. After that, however, its value began to increase again and almost restored at the end of exposure. This result coincided well with the tendency of the changes in ultrasonic pulse velocity.

Table 2 Mecanical properties of concrete

Age (days)	Normal concrete		Reactive concrete	
	Compressive strength f'_c (N/mm^2)	Elastic modulus E_c (kN/mm^2)	Compressive strength f'_c (N/mm^2)	Elastic modulus E_c (kN/mm^2)
8	30.0	25.2	33.8	27.7
491	–	–	27.7	11.6
550	–	–	26.8	21.9
1150	28.2	24.9	26.5	25.4
4495	31.9	32.7	32.9	29.9

Table 3 Results of loading test

Calculated		Measured			
Flexural capacity $P_{uf.cal}$ (kN)	Shear capacity $P_{us.cal}$ (kN)	Flexural cracking load $P_{cr.mea.}$ (kN)	Shear cracking load $P_{scr.mea.}$ (kN)	Maximum load $P_{u.mea.}$ (kN)	Failure mode
2189	1680	437	1300	2367	flexure

3.2 Results of beam loading test

3.2.1 Load carrying capacity and failure mode

Figure 8 shows the appearance of the beam after the loading test. In Table 3 are listed the measured maximum load and so on together with the calculated flexural and shear capacity according to the JSCE Standard Specifications for Concrete Structures [7], in which the mechanical properties of concrete at 4495 days were used and the material factors were set to be 1.0.

Figure 8 The appearance of the beam after the loading test

As indicated in Table 3, the beam failed finally in flexure although it was designed to fail in shear. This is mainly due to that the equation for estimation of shear capacity in JSCE Specifications is rather conservative and tends to underestimate the effect of prestress including chemical one. In addition, inspection after the loading test showed that rupture of stirrups did not occur during the exposure period, and this led to the preservation of shear capacity.

The measured maximum load well exceeded the calculated flexural capacity. However, the cover concrete in the compression zone of section peeled off in layers along with the existing expansive cracks at the ultimate state as seen in Figure 8. From these results, the design ultimate capacity of ASR damaged members might be guaranteed as long as no rupture occurs in tensile and shear reinforcements, although the final failure mode would be affected by the condition of existing cracks.

3.2.2 Deformation characteristics

Figure 9 shows the load – deflection relationships at the mid-span and the loading points. In Figure 10 are shown the relationship between the applied load and the maximum flexural and shear crack width. Flexural crack width was measured at the position of 35mm from the tension fibre in the mid-span region and shear one was measured at the mid-height of the section in the shear span on the line drawn from the loading point with 45 degrees against the vertical line.

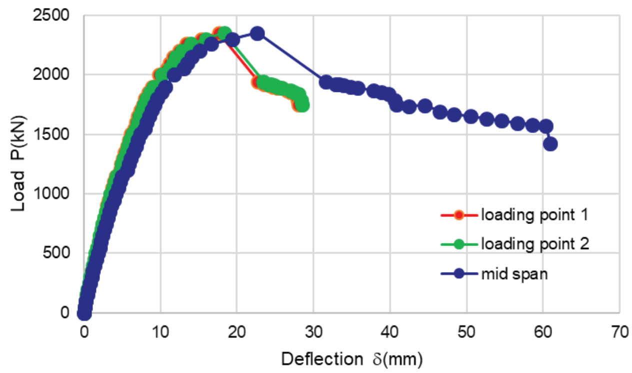

Figure 9 Load – deflection relationships

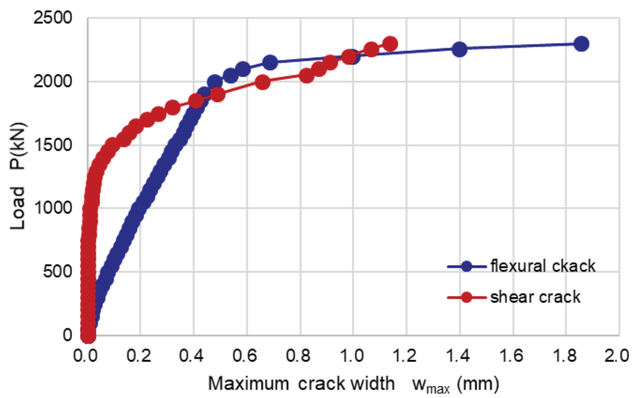

Figure 10 Load – maximum crack width relationships

As seen in Figure 9, the load – mid-span deflection curve turns out similar to the one which is observed typically in reinforced concrete members having an under-reinforced section.

Flexural cracks occurred at 437 kN and the maximum crack width increased linearly until the yielding of tensile reinforcement. Although a shear crack occurred at around 1300 kN and its width increased up to approximately 1.2 mm, shear failure did not occur due to the effect of introduced chemical prestress. In addition, the no-ruptured stirrups, although their rupture had been expected during the exposure, performed well as shear reinforcement.

3.3 Inspections after the loading test

3.3.1 Internal cracks

The beam was cut into 3 pieces after the loading test at the positions (700 mm from both ends, see Figure 1) within the shear spans where the effect of loading test could be eliminated, and expansive crack propagation inside the concrete was observed. Figure 11 shows the internal cracking profiles of the sections.

As seen in Figure 11, relatively large cracks were observed in the concrete in the left and right inside sections. Large cracks were also observed at the position of the lower tensile reinforcement. These cracks connected with each other through the horizontal direction of the section. Except for these cracks, development of expansive cracks remained generally within the cover concrete outside the stirrups.

3.3.2 Effect of anisotropy of ASR expansion on the properties of internal concrete

The effect of anisotropy of ASR expansion on the mechanical properties of internal concrete is examined by using concrete core specimens. These core specimens (ϕ 100 mm cylinder) were taken from the outside cut pieces of the beam in vertical, horizontal and longitudinal directions. The vertical specimens were taken from the top surface, while the other two were taken from the mid-height of the side surface and the cut surface, respectively. The number of specimens was three in each direction. Compressive strength and elastic modulus of these core specimens were measured. The average values of them are listed in Table 4.

As seen in Table 4, both of compressive strength and elastic modulus were the largest in vertical direction and the smallest in horizontal direction. However, these values were considerably smaller than those of the exposed specimens (see Table 2). This might be mainly due to the effect of released expansion of the core specimens as well as the inner cracks occurred during the loading test.

As for the effect of anisotropy of ASR expansion, definite difference was observed especially in the value of elastic modulus. The vertical specimens included the cover concrete of the top surface, in which ASR expansion almost finished as shown in Figure 6. On the other hand, the horizontal and longitudinal ones were taken from the mid-height of the section where the restraining of ASR expansion was relatively large, and this might result in larger released expansion especially in horizontal direction.

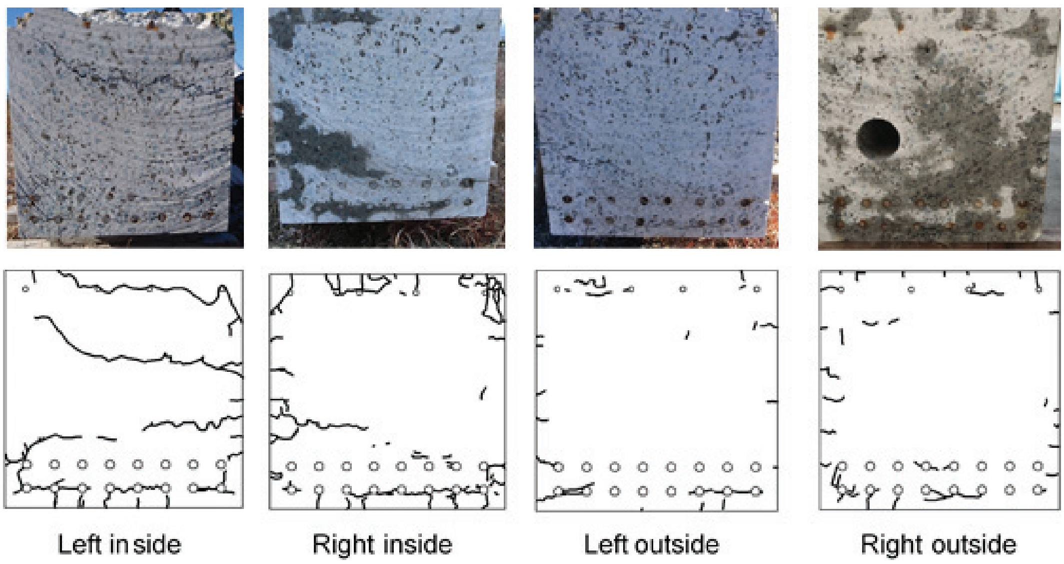

Figure 11 Cracking profiles inside the sections

Table 4 Test results of concrete core specimens

Vertical		Horizontal		Longitudinal	
Compressive strength f_c' (N/mm²)	Elastic modulus E_c (kN/mm²)	Compressive strength f_c' (N/mm²)	Elastic modulus E_c (kN/mm²)	Compressive strength f_c' (N/mm²)	Elastic modulus E_c (kN/mm²)
18.2	12.2	14.5	5.75	17.5	9.04

3.3.3 Condition of longitudinal bars and stirrups after the loading test

After the loading test, cover concrete in the mid-span region was tipped away and the condition of longitudinal bars and stirrups was observed. Figure 12 shows some profiles of the observed conditions.

As seen in Figure 12, longitudinal bars as well as stirrups corroded severely during the exposure due to the influence of NaCl which was added to obtain the prescribed total alkali contents. However, rupture of stirrups was not observed irrespective of the bending radius at the corners. One of this reason was that the shape of lugs and ribs of the used reinforcing bars was different from those of the ones used in the practical structures constructed more than several decades ago in which the rupture of them was detected. As shown in Table 3, the measured maximum flexural capacity exceeded well the design value and the final failure mode was flexure although shear was predicted. From these results, ASR expansion and reinforcement corrosion in the tested beam did not significantly affect the load carrying capacity.

Mid-span region

Bent corner of a stirrups

Figure 12 Condition of longitudinal bars and stirrups

4 Conclusions

In this study, ASR expansion characteristics in a relatively large scale reinforced concrete beam was investigated through the exposure of more than 12 years. Residual load carrying capacity was also examined by static loading test after the exposure. The main conclusions obtained are summarized as follows.

The expansive strain of the used reactive concrete increased up to approximately 4300×10^{-6} at the age of about 3 years. After that, however, the increase was not observed, and thus, the expansion of concrete almost finished at the age of about 12 years. The expansive strain in the tested beam showed different profiles according to the measuring position. The vertical strains in the side surfaces as well as the upper longitudinal ones increased further from the age of 1150 days while the horizontal strain in the upper surface showed the same tendency as that of the test pieces. This was mainly due to the increase in crack width of the existing expansive cracks caused by the eccentric chemical prestress. The influence of reinforcement corrosion on the increase in crack width was also considered. The estimated introduced chemical prestress was approximately 6.5 N/mm^2 at the bottom fibre of the section.

The elastic modulus of the reactive concrete test specimens decreased remarkably at the age of 491 days. After that, however, its value began to increase again and almost restored at the end of exposure. Similar tendency was observed in the changes in ultrasonic pulse velocity measured in the beam. This implies that re-filling of micro cracks and pores by alkali-silica gel might occur.

In the static loading test, the beam failed in flexure and its residual capacity exceeded well the design value although shear failure was predicted. This is mainly due to the conservativeness in the design equation for shear capacity and the effect of chemical prestress. In addition, rupture of stirrups did not occur during the exposure period, and this led to the preservation of shear capacity.

In the inspection after the loading test, a few relatively large expansive cracks were observed in the internal core concrete of the beam. Horizontal cracks at the position of the lower tensile reinforcement were also observed. Except for these cracks, the development of expansive cracks remained generally within the cover concrete. As for the effect of anisotropy of ASR expansion, definite difference was observed especially in the value of elastic modulus. This might be related to the released expansion of the concrete core specimens. In the core specimens taken from the direction and position where the restraint of expansion was relatively large, elastic modulus as well as compressive strength tended to show smaller values.

Although the rupture of stirrups was expected during the long-time exposure, no rupture occurred practically in spite of large expansion and relatively severe corrosion. Thus, the residual load carrying capacity of ASR damaged members might be guaranteed as long as the rupture of stirrups as well as tensile reinforcement did not occur.

References

[1] Multon, S.; Seignol, J.F.; Toutlemonde, F (2006) – Chemomechanical Assessment of Beams Damaged by Alkali-Silica Reaction, Journal of Materials in Civil Engineering, ACSE, Vol.18, No. 4, pp. 500-509

[2] Japan Society of Civil Engineers (2005) – State-of-the-Art Report on the Countermeasures for the Damage Due to Alkali-Silica Reaction, Concrete Library 124 (in Japanese)

[3] Inoue, S.; Oshita, H.; Sawai, K.; Hatano, Y. (2008) – Effect of Rupture of Shear Reinforcement on Shear Capacity of ASR Damaged Reinforced Concrete Beams, Proc. of the 13th ICAAR

[4] Inoue, S.; Mikata, Y.; Takahashi, Y.; Inamasu, K. (2012) – Residual Shear Capacity of ASR Damaged Reinforced Concrete Beams with Ruptured Stirrups. Proc. of the 14th ICAAR

[5] Japanese Standards Association (2001) – Method of test for alkali-silica reactivity of aggregates by chemical method, Japan Industrial Standards, JIS A 1145

[6] Siegert, D.; Multon, S.; Toutlemonde, F. (2005) – Resonant Frequencies Monitoring of Alkali Aggregate Reaction (AAR) Damaged Concrete Beams, Experimental Techniques, Vol. 29, No. 6, pp. 37-40

[7] Japan Society of Civil Engineers (2017) – Standard Specifications for Concrete Structures – 2017, Design

Studies on flexural behavior of post-tensioned concrete beam structure deteriorated by alkali-silica reaction

Estudos sobre o comportamento em flexão da estrutura de uma viga de betão pós-tensionada, deteriorada pela reação álcalis-sílica

Takuro Maeda
Yukio Hiroi
Hideki Manabe
Takashi Yamamoto
Toyo Miyagawa

Abstract

Alkali Aggregate Reaction (ASR) has been recognised as one of factors to degrade the mechanical properties of concrete structures. In this study, the purpose of this research mainly is looking for a proper quantitative approach to evaluate the degree of flexural capacity on ASR deteriorated structures. However, the internal condition of concrete members to be taken to observe deterioration into concrete structures are often inaccessible. Due to this limitation, the deteriorated levels and quantitative evaluation for flexural capacity on concrete structures still remain unknown. Therefore, an appropriate evaluation method to quantify the deteriorated levels and flexural capacity of concrete structures under ASR effect is significant undertaking. In this study, the authors proposed an analytical model to evaluate the flexural capacity of prestressed concrete (PC) beam deteriorated by ASR associated with measurement results, loading condition, and the crack density, as well as reactivity parameters related to mechanical properties, so that the degradation of concrete structures can be modelled for ASR conditions.

Resumo

A reação álcalis-sílica (RAS) tem sido reconhecida como um dos fatores que degradam as propriedades mecânicas das estruturas de betão. Neste estudo, o objetivo da pesquisa é procurar uma abordagem quantitativa, adequada para avaliar a capacidade em flexão de estruturas deterioradas pela RAS. No entanto, as condições internas dos elementos de betão a serem considerados para observar a deterioração nas estruturas de concreto estão frequentemente inacessíveis. Devido a essa limitação, os níveis de deterioração e a avaliação quantitativa da capacidade em flexão de estruturas de betão permanecem desconhecidos. Assim, um método de avaliação adequado para quantificar os níveis de deterioração e a capacidade em flexão de estruturas de betão afetadas pela RAS é um empreendimento significativo. Neste estudo propõe-se um modelo analítico para avaliar a capacidade em flexão de vigas de betão pré-esforçado deterioradas pela RAS, associado à medição de grandezas, condição de carregamento e densidade de fissuras, bem como parâmetros da reação expansiva

Keywords: Alkali aggregate reaction / Crack density / Expansion / Prestressed concrete

Palavras-chave: Reação álcalis-sílica / Densidade de fissuras / Expansão / Betão pré-esforçado

Takuro Maeda

Engineering Department
CORE Institute of Technology Corporation
Osaka, Japan
t.maeda@coreit.co.jp

Yukio Hiroi

Engineering Department
PC Division, IHI Construction Service Co., Ltd.
Tokyo, Japan
yukio_hiroi@iik.ihi.co.jp

Hideki Manabe

CORE Institute of Technology Corporation
Osaka, Japan
manabe@coreit.co.jp

Takashi Yamamoto

Kyoto University
Kyoto, Japan
yamamoto.takashi.6u@kyoto-u.ac.jp

Toyo Miyagawa

Infra-System Management Research Unit
Kyoto University
Kyoto, Japan

MAEDA, T. [*et al.*] – Studies on flexural behavior of post-tensioned concrete beam structure deteriorated by alkali-silica reaction. **Revista Portuguesa de Engenharia de Estruturas**. Ed. LNEC. Série III. n.º 15. ISSN 2183-8488. (março 2021) 55-64.

1 Introduction

Despite the fact that ASR has been considered as one of factors to cause decreased mechanical properties in structures, due to the limited information, it is unclear to define how such phenomenon affects the flexural capacity in existing ASR-affected PC beam structures. In addition, an appropriate method for quantifying the magnitude of flexural capacity after ASR damage occurred and initiated corrosion of embedded steel reinforcements still remain unknown. The primary objective of this study is to develop a reasonable method to estimate mechanical properties of ASR deteriorated concrete structures by estimating the crack density of concrete members or components' surface and the mechanical properties of drilled cores, and the performance of flexural capacity is then proposed. Based on this process, the correlation between decreased mechanical properties of concrete and flexural capacity of PC structures can be clarified.

The amount of expansion commonly serves as an index to describe the degree of ASR deterioration in concrete structures. However, the internal condition of concrete members to be taken to observe deterioration into concrete structures are often inaccessible. Moreover, for PC structures, in most common procedure for obtaining a core drilled from a concrete specimen, it is typically taken perpendicular to a horizontal surface. It is difficult to drill a core specimen from a longitudinal axis that prestressed tendons originally placed. Thus, to find more efficient approaches to examine the influence of ASR deterioration, the author proposed the method to quantify the mechanical properties of ASR deteriorated concrete at bridge axial direction by linking with the crack density of concrete members surface and the mechanical properties of drilled cores. Finally, the determination of input values associated with investigations and measurements discussed in this study on the effect of ASR were organized in simulations as detailed below.

2 Determination of ASR deteriorated index and input values

2.1 Crack density and retention rate of mechanical properties

2.1.1 Amount of expansion and retention rate of mechanical property

The relationship between amount of expansion and retention rate of mechanical property can be seen in Figure 1 [1,2], in terms of elastic modulus (E_c), compressive strength (f'_c) and tensile strength (f_t), respectively. In this figure, the data were obtained in the minimum limits for expansion in unconfined free-expansive specimens and retention rate of mechanical properties in unconfined cylindrical specimens. Linear regression analysis was applied to quantify the relationship between expansion and retention rate of mechanical properties for E_c. The scatter plot is presented in Figure 2. Due to difficulties in evaluating ASR-induced expansion on real structures during construction period, the measurements of crack density and retention rate of mechanical property in monitoring long-term exposed specimens were selected for assessing deteriorated index instead of the use of expansion amount on structures.

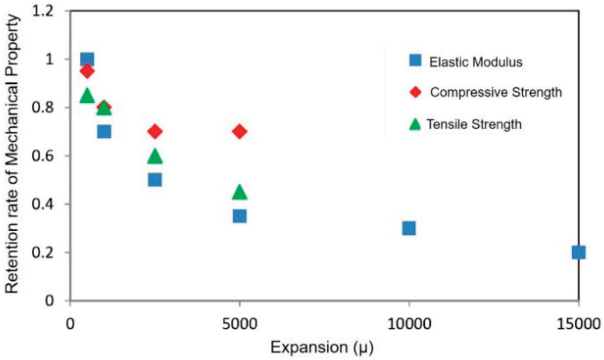

Figure 1 Expansion and retention rate of mechanical property relationship [1,2]

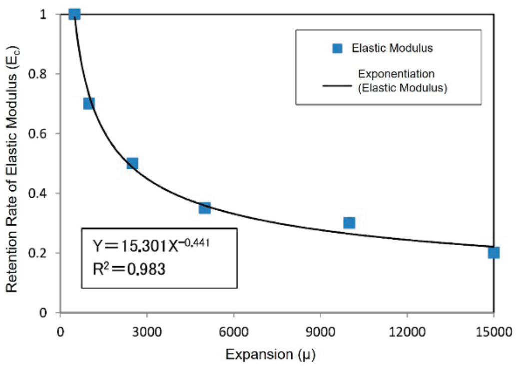

Figure 2 Expansion and retention rate of elastic modulus relationship

2.1.2 Crack density and amount of expansion

A series of measurements was conducted on both large scale and medium scale specimens to evaluate the values of crack density and expansion, where the values of expansion here are perpendicular to the direction of maximum expansion. In the case of PC structures, because the development of expansion is restrained by PC tendons and prestressing bars, etc., the greater expansion occurs in the direction that is perpendicular to and vertical to prestressing are than to the axial direction. The computation of crack density corresponding to the real structures has two criteria. The values of top and bottom of specimens were excluded from consideration during the crack density calculations. On the other hands, the values of side of specimens with the cracks which were equal to or greater than 0.2 mm ($w \geqq 0.2$ mm) were considered to be carried out in calculation. Additionally, in the case of ASR deteriorated PC beam structures, existing cracks have wider width of cracks compared with new cracks and thus, the crack density has a tendency to converge [3]. Therefore, to compute crack density, the width of cracks should be introduced for evaluating ASR deteriorated condition (Method B). The crack density of Method A (m/m^2) is defined as the length of cracks per unit of area, whereas for Method B (mm · m/m^2), the crack density is defined as the length × width of cracks per unit of area. Figure 3 shows the relationship between crack density of Method A and expansion that that the formation of the cracks occurred on side of specimens. Similarly, Figure 4 illustrates the crack density of Method B and expansion relationship that the formation of the cracks occurred on side of specimens. Compared with the results of Figure 3 and Figure 4, it is clear that Method B, introducing width of cracks into crack density computation, has a more significant correlation (R^2 = 0.931) than Method A. Therefore, in this study, to meet the aim of safety assessment, the Method B is adopted for determining crack density to evaluate the influence of expansion on ASR deteriorated PC specimens.

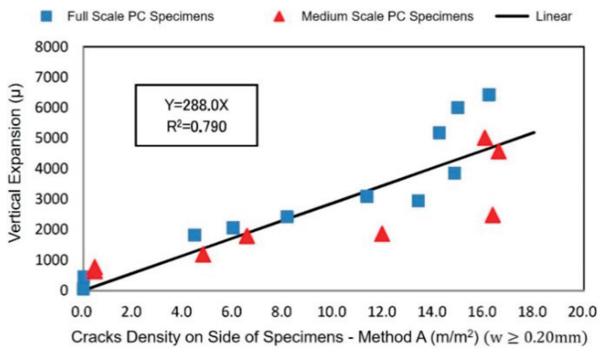

Figure 3 Relationship between vertical expansion and crack density on side of specimens-method A

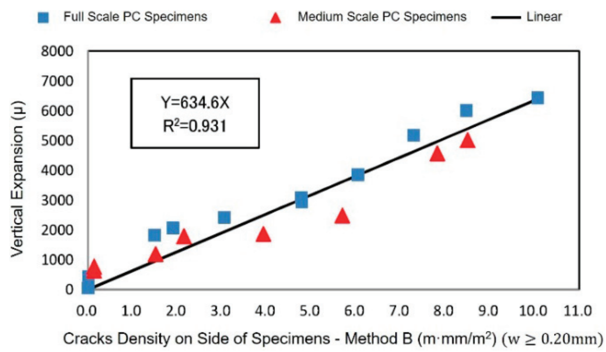

Figure 4 Relationship between vertical expansion and crack density on side of specimens-method B

2.1.3 Crack density and retention rate of mechanical property

To evaluate the relationship between crack density and retention rate of mechanical property on ASR deteriorated specimens, it was assumed that vertical expansion is equal to the expansion. As shown in Figure 4, linear regression equation ($Y = 34.6\ X$) was applied to quantify the relationship between expansion at vertical direction and crack density of Method B on side of specimens. The equation was replaced vertical expansion with crack density of Method B, in writing a formula for linear regression line. Then the relationship between crack density of Method B and retention rate of mechanical property can be confirmed with the following equation:

$$\text{Crack density of Method B} = \frac{\text{Expansion}}{634.6} \quad (1)$$

2.2 Assessment of anisotropy difference in drilled cores and restrained of prestressing direction

2.2.1 Significance of mechanical properties of drilled cores under long-term exposure to ASR condition

A series of loading tests were conducted on ASR deteriorated specimens to assess the mechanical properties of drilled cores. Here, large scale specimens were assumed to be representative of actual in-situ condition. The tested pieces (TP) were obtained from the specimens after loading tests at axial and vertical direction. The locations of cores were plotted corresponding to inner and surface shown in Figure 5(1) and Figure 5(2), and the test results are summary in Figure 6.

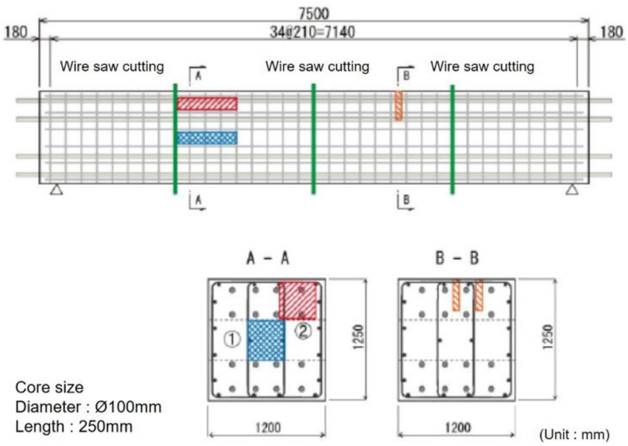

Figure 5 Location of drilled cores (TP)

2.2.2 Conversion coefficient determination at axial direction

In most common procedure for obtaining a drilled core drilled from a concrete specimen, a core specimen taken perpendicular to a longitudinal surface, so that its axis is perpendicular to the prestressing tendons as originally placed. In order to obtain the mechanical properties for real applications, determination of conversion factors is needed. Nevertheless, one of key problems for the conversion is that the conversion coefficient may yield significantly with characteristics of existing structures, the levels of ASR deterioration and mechanical properties. Hence, an appropriate conversion coefficient for core specimens is difficult to determine.

Currently, it is noted that the drilled cores perpendicular to prestressing are applied to evaluate flexural capacity in most cases. Previous studies [4-11] have investigated reduction rate of compressive strength (f'_c) and elastic modulus (E_c) on TP of ASR deteriorated PC beam structures. The obtained data is summary in the Table 1 and presented in Figure 7 and Figure 8.

In this study, a major modification of the input parameters for TP's mechanical properties has to be replaced measurement values to reduction rate B, where reduction rate B is the value in perpendicular direction to the axial direction (the values in perpendicular direction / the values in axial direction). The reduction rate B corresponding to f'_c and E_c at axial direction are listed in Table 1 and shown on Figures 9 and Figure 10.

In the case of f'_c at axial direction, the reduction rate B is in the range of 43% to 96%, and the average of which is about 71%. Whereas, the reduction rate B of Es falls into the range of 30%~85%, tending to have averagely decreased by 58%. Here, conversion coefficient (α) in axial direction defines as an inverse relationship to the reduction rate B, and then the new value at axial direction can be computed from multiplication by α and TP values corresponding to perpendicular and vertical direction, respectively. However, the magnitude of reduction rate B is dependent on α. It was inferred that the selection of large value in reduction rate B (i.e 43% [11]) lead to have large value in α. On the other hand, for the selection of low reduction rate of B might overestimate the design values.

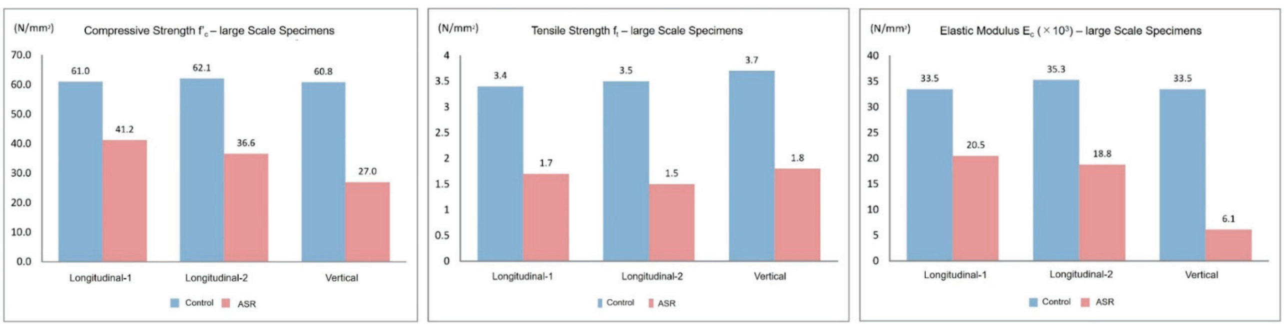

Figure 6 Summary of the mechanical properties of TP

Table 1 Conversion coefficients on compressive strength and elastic modulus

	Type of structures		Core		Compressive strength				Elastic modulos			
	PC/RC	Structures	Direction	Size	Design	Measurement	Reduction rate A	Reduction rate B	Design	Measurement	Reduction rate A	Reduction rate B
					a	b	b/a	Axial direction	c	d	d/c	Axial direction
				mm	N/mm²	N/mm²	%	%	N/mm²	N/mm²	%	%
Ueda *et. al.*	PC	Post tensioned specimen	Axial	∅100 × 200	36.0	48.0	133		29800	32300	108	
			Axial		36.0	40.3	112	96	29800	21000	70	
			Vertical		36.0	46.1	128	88	29800	27500	92	85
			Vertical		36.0	42.2	117		29800	19400	65	60
Tomiyama *et. al.*	PC	Prestressed H	Perpendicular	∅68 × 100	49.3	44.3	90		33000	15200	46	
Kawashima *et. al.*	PC	PC beam	Perpendicular to the axis of bridge footing	∅68 × 130	35.0	37.9	108		27800	12000	43	
					35.0	44.4	127		27800	19500	70	
Inagaki *et. al.*	PC	Post tensioned specimen	Axis of bridge	∅55 × 110	50.0	48.0	96		33000	20500	62	
			Vertical		50.0	40.0	80	83	33000	16500	50	80
			Perpendicular		50.0	37.0	74	77	33000	14000	42	68
Aikyo *et. al.*	PC	Prestressed H	Perpendicular		50.0	30.0	60		33000	6500	20	
Minato *et. al.*	PC	Post tensioned T	Perpendicular		40.0	40.0	100		31000	23200	75	
	PC	Post tensioned T	Perpendicular		40.0	40.0	100		31000	14000	45	
	PC	Post tensioned T	Perpendicular		40.0	35.0	88		31000	7800	25	
	PC	Prestressed H	Perpendicular		50.0	55.0	110		33000	24750	75	
Author	PC	Post tensioned specimen	Inner of bridge axis	∅100 × 250	36.0	41.2	114		29800	20500	69	
			Surface of bridge axis		36.0	36.6	102		29800	18800	63	
			Vertical		36.0	27.0	75	66	29800	6100	20	30
Report of Hansin Express Co, Ltd.	PC	PC specimen	Axial	∅75 × 150	36.0	40.2	112		29800	21900	73	
			Perpendicular		36.0	27.1	75	67	29800	16000	54	73
			Perpendicular		36.0	20.5	57	51	29800	7200	24	33
			Vertical		36.0	17.2	48	43	29800	6700	22	31

Consequently, to obtain the TP values of ASR deteriorated PC beam structures, a unique set of conversion coefficient at axial direction, namely, $\alpha_1 = 1.4(100/71)$ and $\alpha_2 = 1.7(100/58)$ were determined in this study. In the case of tensile strength (f_t), the scatter plot had insufficient data points to perform the analysis. Thus, based on author's research [10] (Figure 11), $f_t = 1/24 f'_c$ for the input setting.

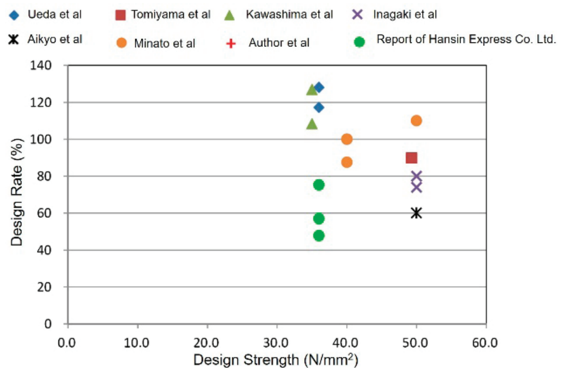

Figure 7 Reduction rate of compressive strength (vertical direction along bridge axis)

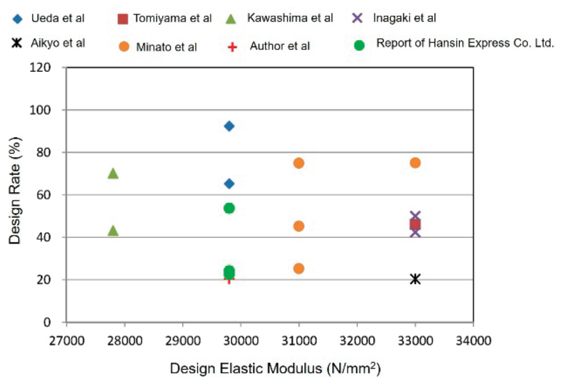

Figure 8 Reduction rate of elastic modulus (vertical direction along bridge axis)

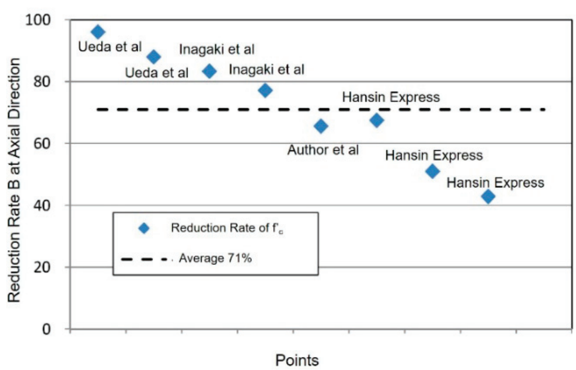

Figure 9 Reduction rate of compressive strength

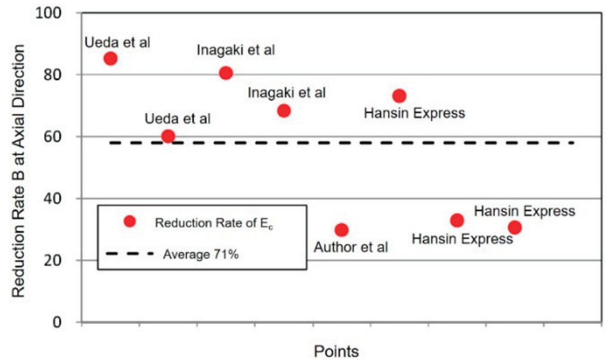

Figure 10 Reduction rate of elastic modulus

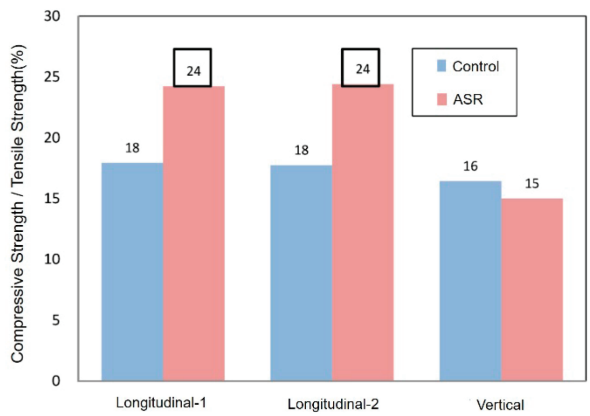

Figure 11 compressive strength / tensile strength (%)

3 Flexural strength of PC beam specimens assessed by deteriorated index

3.1 Flexural capacity verification via crack density method

3.1.1 Crack density evaluation based on Method A and Method B

Recently study revealed that the formation of the cracks occurred in PC structures inhibit the tendency of the cracks to stop propagation. The concept of Method B which has been discussed above was introduced by considering the width of cracks and expansion to evaluate the condition of ASR deteriorated structures. However, in most of cases, Method A is commonly used to describe the crack density of ASR deteriorated condition. In the following research, Method B was applied to quantify and examine crack density based on the results obtained from Method A. The results of Method A and Method B are shown in Figure 12.

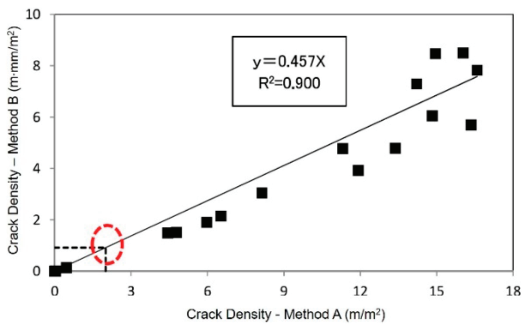

Figure 12 Method A and Method B relationship

3.1.2 Crack density estimation at axial direction based on Method B

Experimental studies on mechanical properties of concrete specimens under large scale tests were conducted and summarized in Table 2. The modelling simulation employed for this study to estimate flexural capacity is schematically shown in Figure 13.

The estimation for crack density of Method B (E_B) can be computed numerically by crack density of method B on side of specimens, in which is 10.078 m · mm/m² W ≧ 0.2 mm at concrete age of 2718 days. The values of EB can be computed from expansion and retention rate of mechanical properties, which illustrated by Equation (2) to Equation (5), and multiplication by retention rate and soundness values. Equation (2) can be obtained with the regression analysis between expansion and crack density of Method B as shown in Figure 12. Moreover, Equation (3)~Equation (5). which defined by the regression analysis of the crack density of Method B were plotted against corresponding retention rate of mechanical properties as presented in Figure 14~Figure 15, respectively.

Expansion $Y = 6.34.6\ X$ (2)

Compressive strength $Y = 0.883\ X^{-0.134}$ (3)

Tensile strength $Y = 0.846\ X^{-0.281}$ (4)

Elastic modulus $Y = 0.891\ X^{-0.441}$ (5)

in which, X is crack density of Method B.

The computed results for retention rate of mechanical properties are listed in Table 2. The EB for flexural capacity analysis in the study presented in Table 3, at which the ratio of average TP is obtained from the average value at axial 1 and axial 2 (Figure 6).

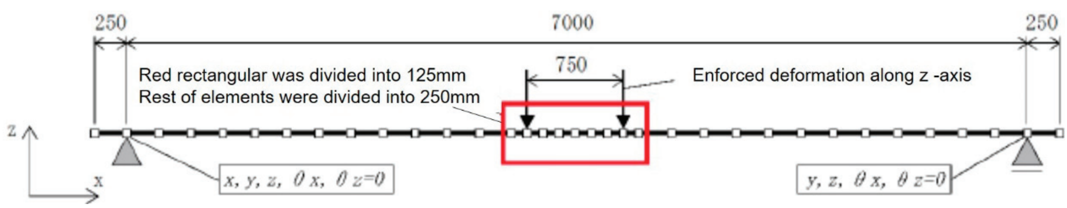

Figure 13 Schematic diagram of FEA modelling system

Table 2 Mechanical properties of tested specimens

	Soundmess values (N/mm²)	ASR					
		Surface values (N/mm²)	Ratio of surface to soundness (%)	Internal values (N/mm²)	Ratio of internal to soundness (%)	Vertical values (N/mm²)	Ratio of vertical to soundness (%)
f_c	61.6	36.6	59%	41.2	67%	27.0	44%
f_t	3.45	1.5	43%	1.70	40%	1.80	52%
E_C	34400	18800	55%	20500	60%	6100.0	18%

Table 3 Retention rate of mechanical properties

Crack density of method B (X) (m · mm/m²)	Expansion (μ)	Equation
10.078	6395	(5.4.1)

Crack density of method B (X) (m · mm/m²)	Retention rate of compressive strength	Equation
10.078	0.65	(5.4.2)

Crack density of method B (X) (m · mm/m²)	Retentiom rate of tensile strength	Equation
10.078	0.44	(5.4.3)

Crack density of method B (X) (m · mm/m²)	Retention rate of elastic modulos	Equation
10.078	0.32	(5.4.4)

Table 4 Results of Estimation B for flexural capacity analysis

	Retention rate of mechanical properties	Soundness value N/mm²	Estimation N/mm² ①	Average values at TP axis N/mm² ②	Ratio ①/②
Compressive strength f'_c	0.65	61.6	40.0	38.9	1.03
Tensile strength f_t	0.44	3.5	1.5	1.6	0.95
Elastic modulus E_c	0.32	34400	11060	19650	0.56

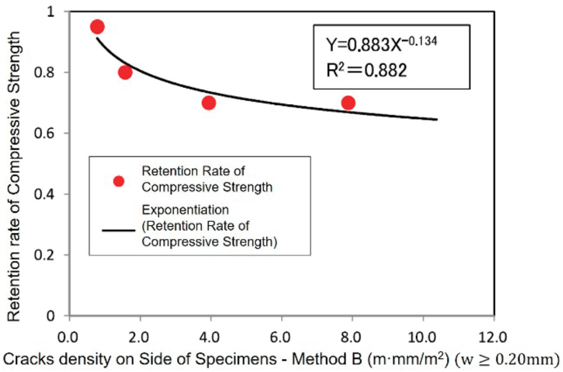

Figure 14 Crack density of Method B and compressive strength relationship

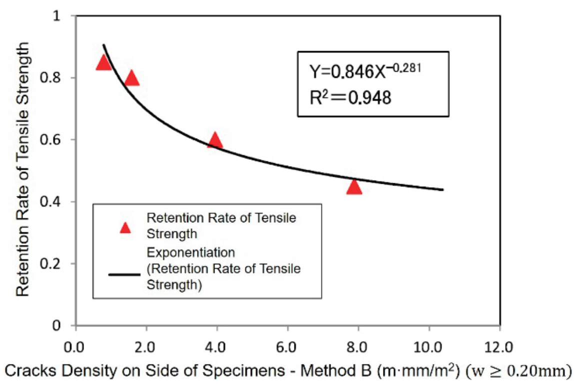

Figure 15 Crack density of Method B and elastic modulus relationship

3.2 Flexural capacity verification via conversion coefficient at axial direction

As mentioned above, the observation indicated the existing difference between the constrained direction of prestressing and the orientation of drilled core. It doesn't render the true values of anisotropic mechanical properties for specimens. Such true mechanical properties at axial direction can be determined from multiplication by conversion coefficient along bridge axis and vertical TP values which is anisotropic to prestressing. Obtained results can be surface valued. A diagram of calculated area (hatched) is shown in Figure 16, and flexural capacity of large-scale PC beam was estimated by modelling system given in Figure 13, while the use of conversion coefficient at axial direct (EA) to define the mechanical properties values for flexural capacity were listed in Table 5.

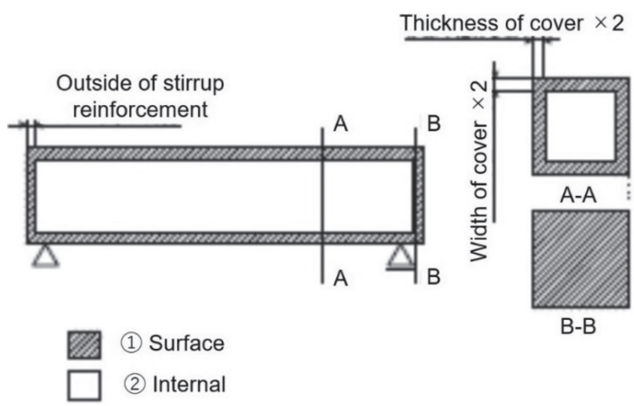

Figure 16 Diagram illustrating details of large-scale PC beam specimen

Table 5 Estimation of flexural capacity at axial direction

		Vertical core values	Conversion coefficient at bridge axis	Estimated mechanical property ①	Average values at TP axis ②	Ratio ①/②
f_c	N/mm²	27.0	1.4	37.8	38.9	0.97
f_t	N/mm²	1.8	σc/24	1.6	1.6	0.98
E_c	kN/mm²	6.1	1.7	10.4	18.8	0.55

3.3 Comparison of various methods

The results of various methods were simulated by the proposed model with corresponding coefficient as shown in Table 6 and their respective data results are shown in Figure 17 and 18. The results of TP axis simulated by FEA modelling system are shown in Table 7 and Figure 19, in which the values of TP axial expressed in ratio are shown in Figure 17.

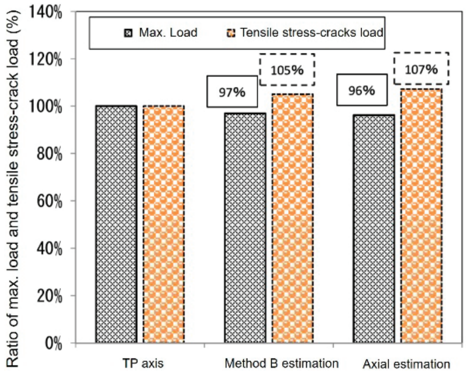

Figure 17 Comparison between max. load and tensile stress-crack load

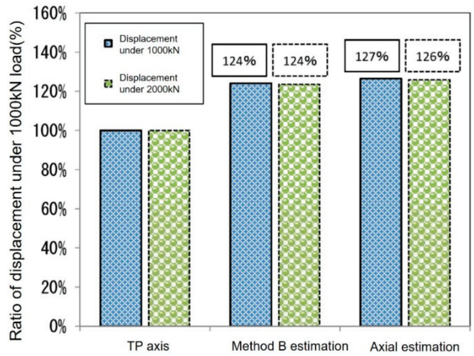

Figure 18 Displacement comparison under 1000kN and 2000kN load

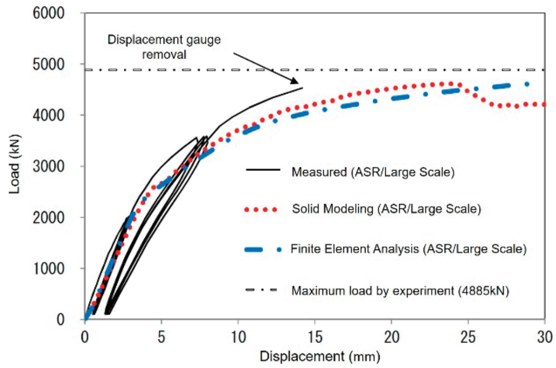

Figure 19 Comparison between model prediction and test results on ASR specimen

Table 6 Summary of simulated results on three methods

	No.	Loads as tensile-stress crack occurred (kN)	Max. load (kN)	Displacement under load of 1000 kN (mm)	Displacement under load of 2000 kN (mm)
TP axis	1	1308	4628	1.43	3.05
Method B estimation	2	1374	4488	1.78	3.77
Axial estimation	3	1402	4450	1.81	3.84

Table 7 Comparison of maximum Loads

Large scale soundness (kN)			Large scale ASR (kN)		
Measurements	Solid model	FEA model	Measurements	Solid model	FEA model
4908	4901	5090	4885	4611	4616
Ratio of measurements	100%	104%	Ratio of measurements	94%	94%

3.4 Summary of results

Regarding to the maximum loads, by using the results of TP at axial direction (TP axis) as a comparison basis for ASR deteriorated specimens, both EB and EA reached 96% consistency for prediction. In the case of tensile stress-crack loads, model simulations were also compared with TP axial results. The predicted loads of Eb and Ea are 105% and 107%, respectively. These implied that both methods provided prominent accuracy compared with TP axial results. Therefore, either Eb or Ea can be selected for evaluating tensile loading during the initiation and evolution of a crack. Considering the displacement, a direct comparison of the difference in displacements by estimated methods is approximately 11mm, inferring that the two methods can be introduced for assessment. As a consequence, the findings concluded that crack density Method B and conversion coefficient at axial direction can be selected for assessing flexural capacity on ASR deteriorated PC beam structures.

4 Conclusion

To examine the influence of ASR deterioration on concrete structures, estimation of mechanical properties of ASR deteriorated concrete specimens by crack density and mechanical properties of drilled cores were proposed. The input data, for instance, mechanical properties, and conversion coefficients, which were introduced to simulate and assess flexural capacity of ASR deteriorated structures was efficient interpretation in this study. The main results and conclusions drawn from this study are summarized below.

1) A FEA model accounting for the influence of ASR deteriorated concrete was performed. Using the set of determined input data proposed by authors, all comparisons between the experimental data and the numerical simulations demonstrated that the model can approximately simulate the initial stiffness and maximum load for PC beam structures.
2) According to the results of long-term measurements, it is confirmed that crack density of Method B was linked and correlated to expansion.
3) It is clearly shown from those figures that expansion has relationship between retention rate of mechanical properties and crack density of Method B. Such relationship can be used to estimate retention rate of mechanical properties by crack density Method B.
4) It is confirmed that either crack density of Method A or Method B is thought to be relatively reliable.
5) To estimate the mechanical properties of ASR deteriorated structures on the constrained direction of prestressing, it can be determined from multiplication by conversion coefficient and mechanical properties of drilled cores.

References

[1] Japan Society of Civil Engineers (2005) – State-of-the-art report on the countermeasures for damage due to alkali-silica reaction – Rupture of reinforcing bars. Concrete Library (124). Japan

[2] CLARK, L.A. (1990) – Structural aspects of alkali silica reaction. Structural Engineering Review, 2, pp 81-87

[3] Prestressed Concrete Contractors Association (2009) State-of-the-art report on the countermeasures for ASR. Japan

[4] Ueda, N.; Nakamura, H.; Kunieda, M.; Maeno, H.; Morishita, N.; Asai, H. (2011) – Evaluations on ASR damage of concrete structure and its structural performance. Journal of JSCE, E2(67.1), pp 28-47

[5] C Tomiyama J.; Yamada, K.; Kaneda, K.; Iraha, S.; Oshiro, T. (2011) – ASR diagnosis by petrographic and evaluation of mechanical performance of ASR deteriorated pretensioned PC Beam. Journal of JSCE, E2 vol. 67 No.4 pp. 578-595

[6] Kawashima, K.; Kousa, K.; Matsumoto, S.; Miura, M. (2011) – Quantitative Evaluation of ASR deterioration Level based on survey result of existing structure. Journal of JSCE, E2 Vol. 67 No. 1 pp. 103-120 2011

[7] Inagaki, T.; Obana Y.; Ishi. T.; Torii, K. (2009) – Evaluation of mechanical properties of drilled cores on ASR deteriorated PC concrete beam structure. Concrete Journal vol. 31 No.1 pp. 1237-1242

[8] Aikyo, K.; (2007) – Soundness assessment and investigation on ASR deteriorated PC bridge. Concrete Journal, vol. 45 No. 8 Page of concrete diagnosis engineer, pp 79-83

[9] Minato, T.; Ishii, K.; Ushiya, S.; Torii, K. (2011) – Characteristics of cracks and current status of countermeasures for ASR deteriorated prestressed concrete bridge. Proceedings of the concrete structure scenarios, JSMS, 11, pp 471-478

[10] Hiroi, Y.; Okubo, T.; Kirikawa, K.; Miyakawa, T.; (2013) – Experimental report on full scale ASR deteriorated PC specimens in loading test Proceedings of the Symposium on Developments in Prestressed Concrete, 22nd, pp 195-198

[11] Hanshin expressway management technology center (2008) – Report of maintenance management methods for ASR-affected structures, Hanshin Expressway Co., Ltd., Japan pringerBasicNumber.zip

Predicting the incidence of alkali-aggregate reaction in Finnish bridges with machine learning

Previsão da incidência das reações álcalis-agregado em pontes finlandesas usando aprendizagem automática

Tandré Oey
Tapio Vehmas
Antti Torkki
Miguel Ferreira
Edgar Bohner

Abstract

Alkali-aggregate reaction (AAR) is a prominent degradation mechanism of concrete structures, which results from the dissolution of reactive silicate aggregates and the associated formation of damaging, expansive AAR gels. Due to the complex nature of AAR reactions, it has remained ambiguous which factors contribute the most to its occurrence on a global scale. Similarly, concrete monitoring in Finland has only recently begun to adapt to the reality that AAR often occurs concomitantly with other degradation mechanisms such as freeze-thaw damage, highlighting the need for critical evaluation of current methods to identify AAR occurrence and distinguish it from these other mechanisms. Machine learning (ML) provides a data-driven framework for both evaluating the relative "importance" of various data features, as well as predicting their consequent influence on AAR damage to concrete. Building on the success of previous such data-driven learning for the prediction of well-defined concrete properties such as compressive strength and setting time, the current work evaluates the feasibility of extending ML methods to AAR-relevant predictions. Results provide new insights into several of the most relevant concrete characteristics linked with AAR occurrence, and establish a basis for future work to extend and enhance such predictions to supplement monitoring and risk management of concrete structures.

Keywords: Alkali-aggregate reaction / Bridges / Feature importance / Machine learning / Prediction

Resumo

A reação álcalis-agregado (AAR) constitui um mecanismo de degradação proeminente das estruturas de betão, que resulta da dissolução de silicatos de agregados reativos e da formação associada de geles expansivos, que provocam danos. Devido à natureza complexa da AAR, são ambíguos os fatores que mais contribuem para a sua ocorrência, na escala global. Por outro lado, a monitorização das estruturas de betão, na Finlândia, só recentemente começou a adaptar-se à realidade de que a AAR ocorre muitas vezes em simultâneo com outros processos de deterioração, como degradação por ciclos de gelo-degelo, destacando a necessidade de avaliação crítica dos métodos atuais para identificar a ocorrência de AAR e distingui-la dos outros mecanismos. A aprendizagem automática (ML) constitui uma ferramenta, baseada em dados, para avaliar a importância relativa desses dados e prever a sua influência nos danos provocados pela AAR. Com base na aprendizagem anterior, baseada em dados bem definidos de previsão das propriedades do betão, como a resistência à compressão e tempo de cura, o trabalho pretende avaliar a viabilidade de estender os métodos de ML para previsões relevantes sobre os efeitos da AAR. Os resultados fornecem novos elementos sobre várias características do betão que são relevantes para a ocorrência de AAR e estabelecem uma base para trabalhos futuros, para estender e melhorar as previsões, em complemento da monitorização e da gestão das estruturas de betão.

Palavras-chave: Reação álcalis-agregado / Pontes / Importância do carácter dos dados / Aprendizagem automática / Previsão

Tandré Oey

VTT Technical Research Centre
Espoo, Finland
tandre.oey@vtt.fi

Tapio Vehmas

VTT Technical Research Centre
Espoo, Finland

Antti Torkki

VTT Technical Research Centre
Espoo, Finland

Miguel Ferreira

VTT Technical Research Centre
Espoo, Finland

Edgar Bohner

VTT Technical Research Centre
Espoo, Finland

OEY, T. [*et al*.] – Predicting the incidence of alkali-aggregate reaction in Finnish bridges with machine learning. **Revista Portuguesa de Engenharia de Estruturas**. Ed. LNEC. Série III. n.º 15. ISSN 2183-8488. (março 2020) 65-76.

1 Introduction

Alkali aggregate reaction (AAR), also commonly referred to as alkali silica reaction (ASR), is a prevalent durability problem in concrete infrastructure. The chemical and physical mechanisms leading to AAR damage of concrete remain poorly understood [1]. While broadly, AAR is acknowledged to be caused by reactive silica-containing aggregates, and exacerbated by high levels of alkalinity and moisture, more detailed understanding is still being developed, complicating efforts to develop general methods for AAR mitigation. In Finland in particular, the likely co-occurrence of AAR with other damage mechanisms (e.g., freeze-thaw damage) has even confounded efforts to diagnose this process, let alone mitigate it. In the absence of knowledge needed to predict AAR occurrence, data-driven machine learning (ML) methods offer an attractive, mechanism-agnostic approach that may achieve such predictions even while lacking detailed physical understanding. For example, ML methods have recently been demonstrated to make reasonable estimations of the 28 day compressive strength of concrete, from either mixture proportions [2], or cement composition and fineness [3]. Although limited application of ML methods to modelling of AAR has been attempted [4], these efforts have likely suffered somewhat from a reliance on largely synthetic, and possibly biased data, as well as relying on accelerated laboratory test methods. The current study focuses on a dataset acquired from inspection reports of several concrete bridge structures currently in service across Finland, with the aim of evaluating feasibility of such ML methods for the prediction and/or diagnosis of AAR under realistic operating conditions.

2 Background and machine learning procedures

2.1 Machine learning algorithms

Several recent studies have demonstrated the ability of bootstrap-aggregated (or bagged) decision tree ensembles to accurately estimate compressive strength of concrete [2, 3]. These rule-based models identify logical splits in the data and partition the input space into a "tree" of decision nodes, which are then followed to arrive at predictions of a target data feature (i.e., "leaf nodes") for each given set of input features. A collection, or ensemble of trees are constructed, with each tree then being trained on different subsets of the data and their results averaged to produce the final prediction [5]. Recent application of these models to concrete has largely been in the context of regression problems, i.e., prediction of a given property (e.g., compressive strength) as a continuous function of input variables. The success of such bagged decision tree ensembles for concrete datasets, which may have relatively high inherent variability, highlights their potential for successful extension to classification problems in this domain, i.e., as necessitated by the nature of the dataset currently under consideration for prediction of AAR incidence in Finnish bridges. As such, bootstrap-aggregated decision tree ensembles are the primary focus of the current study for classification of AAR. More specifically, two particular methods for decision tree construction are given primary consideration due to their past success in the domain of concrete materials: (1) "random forest," wherein a random subset of the input features is considered when determining the split at each decision node, and (2) "extra trees," wherein the threshold for each split is also randomly determined ("extra" being a portmanteau of "extremely" and "randomized"). Other classification algorithms beyond these two were also examined, though it was confirmed that the "extra trees" type random forest model obtained the highest accuracy among these (see *Section 3.1*). All the algorithms and auxiliary functions used for classification were sourced from the scikit-learn library, and can be accessed and downloaded, along with their documentation, at http://scikit-learn.org/stable/.

2.2 Data collection and pre-processing

The dataset under consideration was provided by Väylävirasto, the Finnish Transport Infrastructure Agency. It originally consisted of 156 data records, selected from bridge inspection reports collected on concrete bridge structures across Finland between the years 2016 and 2018 to provide a representative sample of different regions and construction years (methods defined in [6, 7]). Data feature types represented in these original data records are listed in Table 1, along with several that were derived from these features for the purpose of this study. Several data records were noted to be missing some of these original features, and were omitted prior to data pre-processing, resulting in a new input set of 136 data records. Features which consisted of text were then converted to numerical values as follows:

1) Features descriptive of "types" of bridges (e.g., use, maintainer, etc.) were converted to integer values, with lower values arbitrarily assigned to those types that occurred first in a randomly shuffled list of the data records.
2) Features descriptive of "abundances" of materials (e.g., the occurrence of various rock types in concrete aggregates) were assigned integer values, with lower values assigned to relatively lower reported abundance (i.e., "none" = 0, "little" =1, "moderate" = 2, "abundant" = 3).

Table 1 Input features used to train machine learning models for classification of AAR gel (the target feature, shown in gray text). Features from the original bridge inspection reports are shown in plain text, while features determined from these reports for the purposes of the current study are shown in *italic*. The final set of nine features used as inputs for optimized classification models are underlined.

Type-Features
Use (1-7)
Maintainer (1-9)
Environment (0-3)
Marine Exposure (0-1)
Pre-stress (0-1)

Numerical-Features	
Records	Testing
Year Built	Tensile Strength (Minimum)
Year Inspected	Tensile Strength (Maximum)
Location (Latitude)	Carbonation Depth (Minimum)
Location (Longitude)	Carbonation Depth (Maximum)
Condition Score	Chloride Content (Mass % Concrete, Minimum)
Condition	Chloride Content (Mass % Concrete, Maximum)

Abundance-Features	
Thin Section	Aggregate Rock
AAR Gel (0-3)	Slate (0-3)
Cracking (0-2)	Granite (0-3)
Air Voids (0-3)	Gneiss (0-3)
Ettringite (0-3)	Amphibole (0-3)
Calcite (0-2)	Meta-Tuff (0-3)
	Diabase (0-3)
Visual Inspection	Quartzite (0-2)
Map Cracking (0-2, RILEM)	Sandstone (0-1)
Deformation (0-2, RILEM)	Diorite (0-1)
Discoloration (0-2, RILEM)	Phyllite (0-2)
Exudations (0-2, RILEM)	Limestone (0-2)
Pop-Outs (0-1, RILEM)	Gabbro (0-3)
Environment (2-3, RILEM)	Mylonite (0-1)
Other Damages (0-3)	

Numerical features that displayed low or zero variance (i.e., those that were nearly uniform across every data record) were omitted, following confirmation of negligible feature importance (as described in *Section 3.2*) to verify that they did not contribute significantly to classification accuracy. Remaining feature data was inspected to ensure that no unphysical or meaningless values were present (e.g., negative carbonation depths, etc.), of which none were found. Data records were also checked for duplicates, with none being found. Finally, the data records were randomly shuffled to avoid introducing inadvertent bias in the sampling of input attributes during model construction.

Several data features not typically included in inspection reports were also determined and included in the input dataset. These consisted of visual criteria for AAR diagnosis, determined according to RILEM guideline 6.1 [8], and assignment of numerical values to quantify observations of "other damage" (e.g., freeze-thaw damage) as provided from the bridge inspection reports. These additional features, which were assessed similarly to the original features descriptive of "abundances" as described in (2) above, are also included in Table 1, and distinguished from original inspection data using *italic* text.

2.3 Training of classification models

AAR gel abundance was chosen as the target feature because the available dataset contains no other features that would provide a simple (e.g., expansion), unambiguous indicator of AAR occurrence. Even if such features did exist, the available data are also lacking in important details relevant to prediction of concrete's mechanical strength (i.e., cement composition, fineness and mixture proportions [2, 3]), which are likely necessary for ML to extrapolate from the presence of AAR gel to the manifestation of AAR-induced expansion and damage. Lastly, and of particular relevance to AAR incidence in Finland, AAR damage often occurs concomitantly with other damage mechanisms (e.g., freeze-thaw damage), making it difficult to even unambiguously link characteristic cracking patterns or other indicators with AAR. For these reasons, classification by AAR gel occurrence represents a small yet critical first step in moving toward models that would someday be able to predict the extent and kinetics of AAR damage.

Numerous ML classification models were constructed and applied to predict the abundance or occurrence of AAR gel. Training and testing of each model took between one-to-ten seconds, depending on the model used (i.e., for a personal computer with an Intel Core i5-8350u 1,7 GHz processor, and 8GB RAM). Performance of each classification model was evaluated using the prediction accuracy metric, i.e., what fraction of predictions on the test data produced the correct classification for AAR gel abundance (with accuracy ranging from 0 to 1, wherein a value of 1 would indicate that every prediction was correct). Both training and testing were conducted on different portions of data using a standard low-bias resampling procedure called k-Fold Cross-Validation [5]. The data records were randomly split into k = 10 "folds," nine of which were used to train the model, and one of which was used to evaluate the model after training. The process was then repeated nine additional times, each time using a different fold as the test set, and the remaining nine folds as the training set.

The classification models used in this study were not noted to be sensitive to the magnitude of the data attributes, in the sense that they may potentially have been biased to assign more importance to attributes with inherently greater values. Nonetheless, to address this potential artefact, after the training and testing sets were identified and separated, the data for each attribute were rescaled to a standard normal distribution (mean = 0, variance = 1, i.e., using sklearn.preprocessing.StandardScaler). This step was taken after the separation of the training and testing sets to avoid data leakage (i.e., the unintentional passing of information about the test set to the training set), which could potentially happen if the combined testing and training data were rescaled together. In any case, no difference in model accuracy was found between results obtained with and without this rescaling procedure.

2.4 Hyper-parameter optimization

Following model selection and feature selection (detailed in *Section 3.1* and *3.2*), the most accurate model was optimized for the selected feature set in terms of its hyper-parameters (i.e., those that are set before model training, which dictate the speed and quality of the learning process), to arrive at a current best-in-class predictor of AAR occurrence (i.e., the occurrence or abundance of gel). This classification model, an "extra trees" type random forest model, contains two embedded hyper-parameters: (1) the number of data features considered at each "split" when building decision trees, and (2) the total number of decision trees. Additionally, the k-fold cross validation procedure contains a third hyper-parameter: (3) the number of "folds" into which the data is divided prior to construction of the training and test sets.

In the number of features per "split," an optimum in accuracy for five features is observed (out of nine total features, selected as described *Section 3.2*). A similar optimum in accuracy occurs for six "folds" in cross-validation. This is likely due to the small size of the dataset being considered: whereas too few "folds" decreases the size of training sets to a degree sufficient to impair classification accuracy, too many decreases the likelihood that the test set will be representative of broader trends in the data. Lastly, accuracy plateaus with number of trees, with diminishing returns to adding decision trees beyond about 400 (for this specific dataset and ML model). Final models are limited to the use of 400 trees to avoid "overfitting," i.e., building a model that sacrifices its ability to generalize to predictions on unseen data by too closely fitting the available data. Final values for each of the three optimized hyper-parameters with the "extra trees" model are marked in red in Figure 1, corresponding to five features per "split," six "folds," and 400 trees.

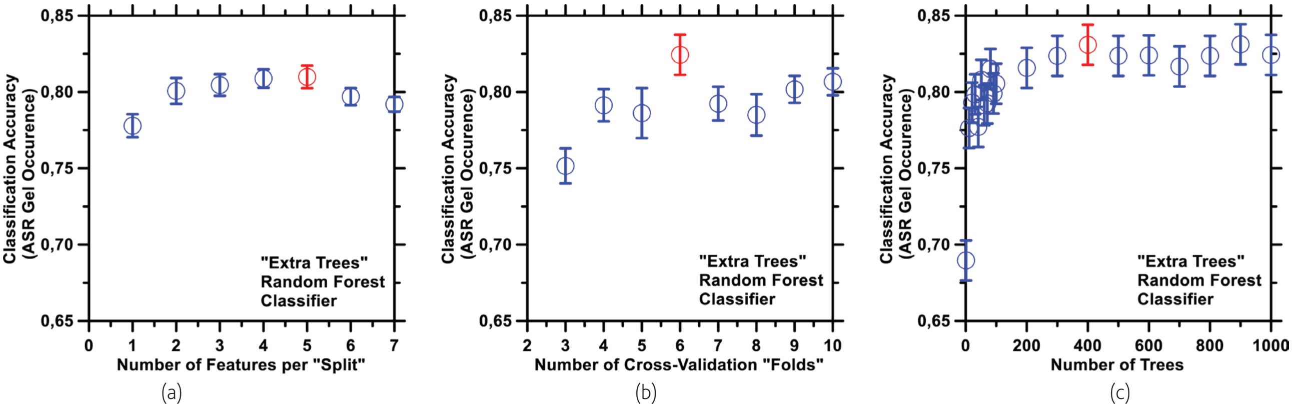

Figure 1 The results of a representative hyper-parameter tuning exercise using the "extra trees" algorithm to classify bridge concretes for ASR gel occurrence, showing (a) an optimum of five features per "split," (b) an optimum of six "folds" of data during cross-validation, and (c) an optimum of 400 trees. Points shown in red indicate parameter values used for final models. Error bars represent the standard deviation between 20 separate train-test repetitions of the models.

3 Results and discussion

3.1 Ensemble models perform best for classification of AAR gel amount

Unsurprisingly, ensemble models of decision trees outperform most other classification models in predicting the abundance of AAR gel in the Finnish bridge concrete dataset (Table 2). Specifically, the "extra trees" random forest model provides the highest classification accuracy, both before and after the feature selection described in *Section 3.2*. This again highlights the ability of such models to perform well, even for data obtained from real concretes that may be prone to high inherent variability [2], a finding now borne out in the context of classification and AAR. Further consideration during feature selection and later steps of analysis is given only to the "extra trees" model, in the interest of defining an upper bound on AAR prediction accuracy that can be obtained using existing bridge inspection data.

3.2 Recursive feature elimination improves classification accuracy

The best performing classification model using all features of the bridge inspection dataset, an "extra trees" type random forest model, was able to obtain only an accuracy score of 0,649, corresponding to about 65% of correct predictions of AAR gel abundance. For comparison, the same classification model trained and tested using inputs where reported values of AAR gel abundance were *randomly* assigned to the data records yielded an accuracy score of 0,450, i.e., the worst-possible performance that could likely be achieved using

Table 2 Accuracy of several common classification models when predicting AAR gel abundance. All models used are open-source, and their documentation can be found at http://scikit-learn.org/stable/.

	Accuracy (0-1)	
Classification Model	After Feature Selection	Before Feature Selection
Non-ensemble models		
K-nearest neighbours	0,600	0,571
Logistic regression	0,630	0,565
Linear discriminant analysis	0,632	0,584
Support vector machine	0,683	0,580
Decision tree	0,676	0,515
Ensemble models		
Bagged trees	0,670	0,612
Random forest	0,691	0,632
Gradient boosted trees	0,692	0,581
"Extra trees" random forest	0,728	0,649

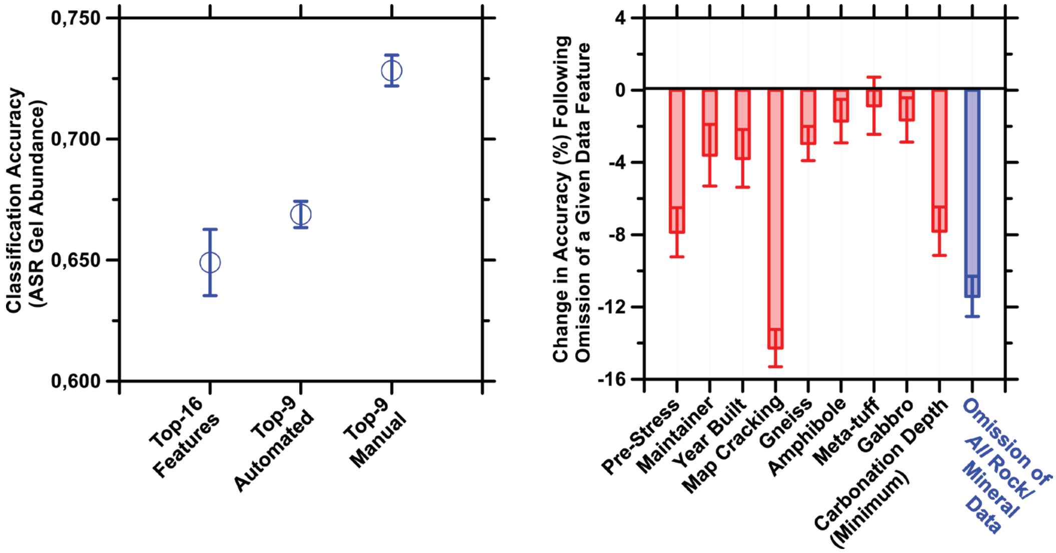

(a) (b)

Figure 2 Results of feature selection, demonstrating (a) the better classification accuracy achieved during recursive feature elimination by preferentially removing features whose omission improved the model prior to those that had negligible significance, and (b) the final "feature importances" of the nine features remaining after recursive feature elimination (i.e., all of which resulted in significantly reduced classification accuracy when omitted from the input data). The cumulative "importance" of the combined rock/mineral data (i.e., decline in accuracy when omitting gneiss, amphibole, meta-tuff, and gabbro together) is also shown for comparison. Error bars represent the standard deviation between 20 separate train-test repetitions of the models.

this dataset. While an accuracy of 0,649 is appreciably higher than this value, it is nonetheless desirable to further refine the "extra trees" model by performing feature selection.

Feature selection typically consists of sequentially removing various data features from the inputs, to identify features that may be (1) of negligible importance to predicting the target feature, or (2) detrimental to such predictions due to being redundant or partially redundant with other features (thus introducing bias). Two methods for such feature selection were tested, both of which fall under the umbrella of recursive feature elimination: omitting features one-by-one and then determining which feature to eliminate from the model based on how much of a change in accuracy its omission produced. The default recursive feature elimination algorithm provided by the scikit-learn library sequentially eliminates the features whose omission produces the *lowest absolute change* in model accuracy. However, it was found that first eliminating those features whose omission produced increase in model accuracy (followed by those producing the lowest absolute decrease) led to a more accurate final model, as illustrated in Figure 2(a). As an example, omission of granite, quartzite, and sandstone abundance led to a roughly 5% increase in classification accuracy, likely due to co-occurrence with other rock types (and thus redundancy with data features corresponding to those rock types). The final feature set arrived at via recursive feature elimination, consisting of nine data features (Figure 2(b)), resulted in a classification accuracy improvement for the "extra trees" model to 0,728, or about 73%.

3.3 Feature importances highlight need for improved monitoring practices

Feature importance, defined herein by the magnitude of accuracy loss (%) upon omission of a given feature from ML model inputs (Figure 2(b)), provides a rough indicator of which available data features one can expect to be most relevant to AAR incidence. Among the nine features remaining after recursive feature elimination, the extent of "map-cracking," a feature often used to distinguish AAR occurrence by visual inspection, appears to be of primary importance. On the one hand, this lends credence to the RILEM method developed to evaluate such visible damage in concrete structures, by demonstrating a significant link with observed AAR gel formation. Additionally, model performance appears not to depend on the "other damage" feature, implying that such ML models represent a reliable means to distinguish AAR from other concurrent damage mechanisms (at least based on the current methods for evaluating such concurrent damage mechanisms). On the other hand the importance of "map-cracking," along with minimum carbonation depth, implies that the current model depends strongly on observation of damage that has already occurred (i.e., rather than being able to estimate AAR risk *a priori*). While this link should be further explored, e.g., by pursuing more quantitative metrics for AAR damage such as via computer-aided image analysis or other non-destructive testing techniques [9–11], it would ultimately be more desirable to train such models exclusively on data reflecting the state of the concrete *before* AAR damage has occurred (e.g., mixture proportions, aggregate mineralogy, etc.).

Importance of unexpected data features, specifically minimum carbonation depth and maintainer, may suggest either (1) the importance of "embedded" data, which correlates with these features but is absent from inspection records (e.g., moisture-resistant coatings that may have been applied to the concrete by specific maintainers), or (2) artificial differences in data due to variable inspection methods (e.g., near-surface sampling that may have impacted AAR gel assessments due to carbonation). While it is currently impossible to distinguish between these two options, both point toward the need for more extensive record keeping and/or more standardized inspection and sampling procedures. This is likely all the more important for one feature that is conspicuously absent from the current dataset, yet widely acknowledged to play a critical role in AAR: moisture [1]. Although several features were present that may have been related to the bridge concrete's moisture state, i.e., environment and location, neither was found to be necessary in accurately classifying bridge concretes by AAR gel abundance. This may of course be due to a similar moisture state among bridges because of the geographically limited nature of the dataset (within Finland), and it is likely that the current classification models would require more detailed data on the moisture state of concrete in order to be applied under circumstances where environmental conditions vary more widely.

Another factor expected to vary between concretes undergoing AAR is their stress state, or confinement, which has been reported to result in preferential expansion along the direction of minimum applied load (i.e., resulting in cracking primarily transverse to this direction [12]). Though past efforts to incorporate the influence of stress into understanding of AAR progression have mainly focused on mechanical effects [13], the importance of pre-stress to AAR gel abundance for the bridge concretes currently under study (Figure 2(b)) suggests that even this rough indicator of mechanical stress is significantly linked to *chemical* driving forces for AAR, i.e., those necessary to influence gel formation. Though it is difficult to comment further without more detailed data on the stress state of these concretes, this would be in line with reported mechanisms for chemo-mechanical coupling in mineral-water systems [14, 15], which have been employed to propose a dissolution-precipitation mechanism at the origin of concrete creep [16]. Current results indicate that more detailed investigation along these lines is merited, specifically the possibility that applied loads may influence dissolution and precipitation in the context of AAR.

Among the lowest "importance" values were assigned to the four rock/mineral features retained by the recursive feature elimination process. However, their cumulative importance was substantial (i.e., when *all* were omitted from the model), second only to the importance of the "map cracking" feature (Figure 2(b)). Obtaining more detail as to the AAR reactivity of these rocks/minerals thus represents a very promising area for future improvements in the accuracy of such models, in particular because they represent a *pre-damage* descriptor of potential AAR risk (as opposed to features reliant on existing AAR damage like cracking or carbonation). Recent work has shown success in linking aqueous reactivity to chemical structure for silicate materials, i.e., those most relevant to AAR due to their release of silicon upon dissolution [17, 18]. To illustrate the potential of this concept, several simple assumptions were tested regarding the reactivity of each rock type or mineral provided in the input data:

1) Cumulative contribution to "reactivity," as relevant to AAR, was assumed to be proportional to the reported abundance of each rock type or mineral (i.e., with reactivity being calculated as a weighted average as outlined in Equation 1 below).
2) "Reactivity" of each rock type, constituted of several minerals, was assumed to be dictated by the most abundant of these minerals in a typical specimen of the given rock (e.g., orthoclase for granite, plagioclase for diorite, pyroxene for gabbro, etc.).
3) "Reactivity" of each silicate mineral (whose structures are defined by SiO_4 tetrahedral units, Figure 3) was assumed to be inversely proportional to the average number of inter-tetrahedral bonds within its chemical structure, i.e., 4 for orthosilicates, 2 for single-chain silicates, 1,5 for double-chain silicates, 1 for sheet silicates, and 0 for tectosilicates [19]. This is an extension of the idea that silicon dissolution is required for AAR to occur [1], and furthermore that silicon dissolution proceeds via sequential breaking (hydrolysis) of inter-tetrahedral Si-O-Si bonds [17]. Such a formulation is the equivalent to the average number of "non-bridging" oxygen atoms that make up the corners of the SiO_4 tetrahedral units in silicates [20], as illustrated in Figure 3.
4) "Reactivity" of each non-silicate mineral (i.e., calcite, from limestone) was assumed to be 0.

$$\text{"Si-Bonding Weighted Average"} = \frac{\sum_1^i A_i N_i}{\sum_1^i A_i} \tag{1}$$

where A_i is the reported abundance for mineral i, and N_i is the average number of "non-bridging" oxygen atoms per tetrahedral unit in the mineral's molecular structure (or 0, for non-silicates).

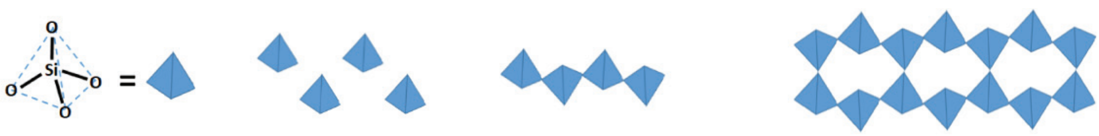

(a) (b) (c) (d)

Figure 3 Illustrations of local molecular structure of (a) an SiO_4 tetrahedral unit, and such units in (b) an orthosilicate: 0 inter-tetrahedral bonds, 4 "non-bridging" oxygens per unit; (c) a single-chain silicate: 2 inter-tetrahedral bonds, 2 "non-bridging" oxygens per unit; and (d) a double-chain silicate: alternating between 2 and 3 inter-tetrahedral bonds, 2 and 1 "non-bridging" oxygens per unit, etc.

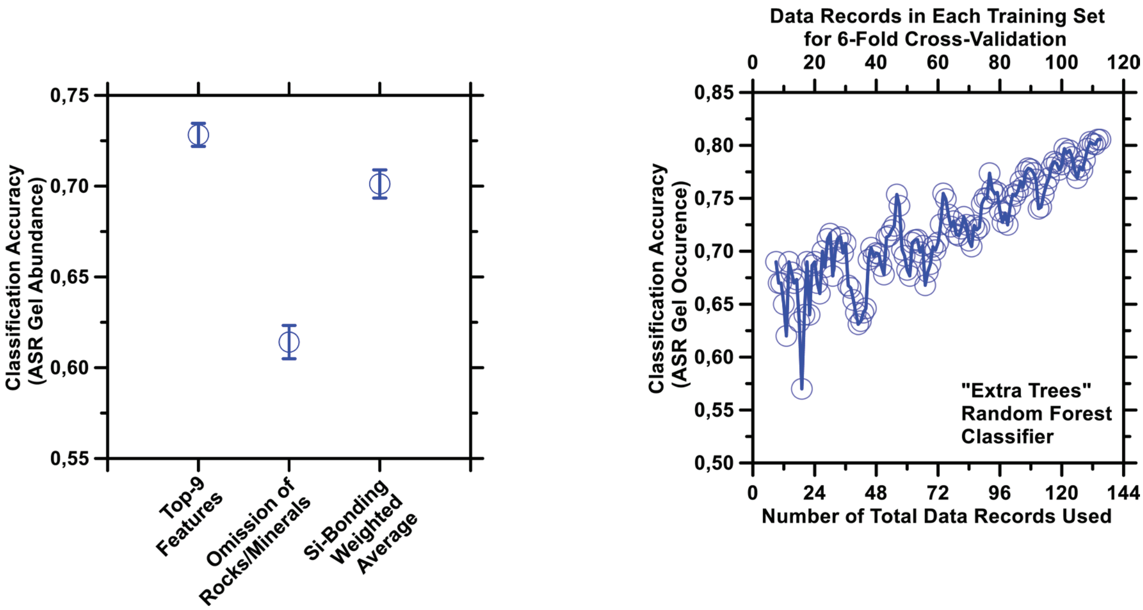

Figure 4 (a) ML classification accuracy following recursive feature elimination (i.e., "Top-9 Manual" from Figure 2(a)) as compared with other ML models wherein (1) all rock and mineral data features were omitted from the inputs, and (2) the "Si-bonding weighted average" was re-introduced to the inputs following such omissions. Error bars represent the standard deviation between 20 separate train-test repetitions of the models. (b) Classification accuracy as a function of the total number of data records used in ML inputs, i.e., an illustrative "learning curve" for the ML classification models.

The end result of the simple assumptions outlined above regarding the influence of silicate aggregates' chemical structure on their AAR reactivity is a weighted average (Equation 1), meant to reflect the cumulative influence of each rock type or mineral on the formation of AAR gel. As demonstrated by Figure 4(a), this "Si-bonding weighted average" produced models with comparable classification accuracy when substituted for the raw data on rock type and mineral abundance in ML inputs. The surprising success of even these very simple assumptions in distilling the data from rock and mineral abundance to a single descriptive parameter, without sacrificing classification accuracy, highlights that improved aggregate characterization methods, e.g., reporting mineralogy data rather than just rock types, hold great potential to improve such predictive modelling efforts.

Though not reflected among the importances of individual data features, the number of data records available should also be noted for its substantial influence on the quality of current classification models. The dataset under consideration, consisting of only 136 data records (i.e., data from each of 136 unique bridge inspection reports), is quite small relative to the size of datasets typically utilized for training ML models. Though recent work has highlighted the ability of such models to perform well even with only a few hundred data records [3], it is nonetheless expected that the AAR gel classification models would continue to improve as more data becomes available. To illustrate this point, "learning curves" were constructed by sequentially omitting full data records from the inputs (Figure 4(b)). It can be seen that, though current models are unstable (accuracy fluctuates with small perturbations to input data), there is a consistent improvement in accuracy with the inclusion of increasingly more data records. The lack of a "plateau" in such a learning curve for the current, limited dataset suggests the likelihood that provision of even more data to the model would, in fact, be able to produce additional accuracy improvements.

3.4 Addressing imbalance in AAR gel class distribution improves accuracy

Though accuracy improvements often necessitate the provision of greater amounts of more detailed data, it is important to recognize that this is not always the case [3]. As an example, skewed distributions between the classes in the target feature (AAR gel abundance) could be expected to somewhat bias the model toward predicting the occurrence of no AAR gel, as this is the majority class (Table 3). For comparison, prediction of only the absence of AAR gel would result in a classification accuracy of 58%. Two methods have been investigated to deal with this possible class bias in ML models: (1) binarization of the classes, i.e., shifting from consideration of *how much* AAR gel has formed to the simpler consideration of *whether* any has formed or not; and (2) stratification of the "folds" during k-fold cross validation, i.e., ensuring that each subdivision of the data used to train and test the models contains an equal number of members of each target feature class.

Table 3 Class distributions for the originally marked dataset according to AAR gel abundance, and the new class distribution after application of binarized class markings based on AAR gel occurrence.

AAR Gel *Abundance* Class Distribution		AAR Gel *Occurrence* Class Distribution	
Class	Population	Class	Population
"None" (0)	79	"None" (0)	79
"Little" (1)	45	"Any" (1)	57
"Moderate" (2)	11		
"Abundant" (3)	1		

Binarization of target feature data from AAR gel abundance to AAR gel occurrence does somewhat reduce the class imbalance problem (Table 3). This results in a marked improvement in model accuracy to about 80% (Figure 5(a)), and may also benefit from the fact that such binarization helps simplify the evaluation of AAR by obscuring any bias accompanying inter-operator variability in quantification of gel abundance from thin section analyses (i.e., removing the degree of subjectivity associated with what any given bridge inspector regards as "little" relative to "moderate" AAR gel). Stratification during cross-validation produces a similar improvement in accuracy to about 78%, or 82% with the combination of both binarization and stratification (Figure 5(a)). This result highlights that current ML classification models are at present best-suited to use as binary AAR diagnostic tools, which identify whether observed damage can be attributed to AAR rather than some other mechanism. Furthermore, it highlights the importance of providing such models with balanced training data, i.e., indicating the need for preferential collection of data from concrete structures that experience AAR, and even more so from those that experience moderate-to-abundant formation of AAR gel. While over-sampling or under-sampling are also known to help reduce such bias [3], i.e., by preferentially including duplicate data records of underrepresented classes or excluding data records of overrepresented classes, neither of these methods were found to be feasible for the current dataset due to its relatively small size.

To verify that class imbalance had been suitably addressed by binarization, the specific nature of each correct or incorrect classification by the model was examined (Figure 5(b)). For example, if the model was biased to preferentially classify data records as having no AAR gel due to this being the majority class, many of its classifications would be false negatives, i.e., they would predict no AAR for concrete where in reality AAR had occurred. Grouping predictions as such yields four types: true negatives (correct predictions of no AAR), true positives (correct predictions of AAR), false positives (incorrect predictions of AAR), and false negatives (incorrect predictions of no AAR). Looking at the split between true positives and true negatives in Figure 5(b), these appear to be in

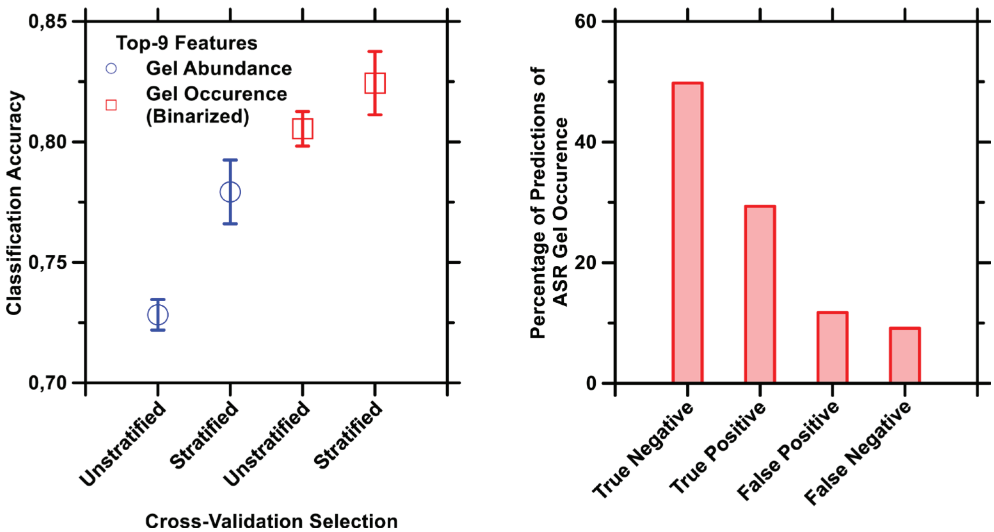

(a) (b)

Figure 5 (a) A comparison in classification accuracy between models with stratified and un-stratified cross-validation for classifying AAR gel abundance (four classes) or occurrence (two classes). (b) The distribution among classification predictions by correctness as well as class, e.g., making the additional distinction between incorrect predictions for those which did or did not truly have AAR gel. Error bars represent the standard deviation between 20 separate train-test repetitions of the models.

rough proportion to the class distribution between concrete with and without AAR gel, respectively. This result confirms that class bias has been largely addressed by binarization and stratification for the current dataset and ML models.

It should also be noted, however, that the "cost" of the various types of predictions has not been factored into current ML models. For example, a model that falsely suggests AAR has occurred when in reality it has not may be deemed as less of a risk than a model that falsely suggests AAR has not occurred when in reality it has. This highlights a promising area for future research regarding use of ML for AAR risk assessment: rather than using algorithms that maximize the number of correct predictions, they could instead minimize the number of false negatives (or any other type of prediction). In the current case of AAR evaluation in concrete, this would mean the difference between the minor short-term cost of applying unnecessary AAR mitigation measures, and the potentially catastrophic long-term cost of structural failure. In this light, if one includes false positives in the calculation of accuracy for the current best-in-class model, it performs at 90% "reliability," only *failing to detect* AAR 10% of the time. Likewise, in the pursuit of a predictive rather than a diagnostic model for AAR (i.e., one not dependent on observation of damage), even previously "poor" models perform somewhat well. When the rate of false positive predictions is combined with classification accuracy, a model trained to make binary predictions for AAR incidence *without* the "map cracking" and carbonation depth features performs with a "reliability" of 85%. This is promising in that, even without improvements in the size or quality of input data, new ML algorithms for cost-sensitive optimization may also have the potential to improve reliability of AAR classification to the point required for their more widespread use in risk assessment or mix design.

4 Summary and conclusions

This study evaluated the feasibility of applying ML methods to the prediction and/or diagnosis of AAR in concrete under realistic service conditions. It was found that using an "extra trees" type random forest algorithm, an accuracy of 78% could be achieved when classifying concretes by AAR gel abundance. This accuracy was improved to 82% when applied to the simpler classification of the existence (or not) of AAR gel in the concretes, and to 90% when factoring in the relatively lower "cost" of falsely predicting the occurrence of AAR (relative to that of falsely predicting that AAR did not occur).

Several significant trends in the importance of various data features were also highlighted, particularly the promise shown by an exercise to incorporate a more detailed understanding of aggregate reactivity while maintaining model accuracy. These trends suggest the need for both:

(1) More thorough record keeping of concrete's raw materials, particularly with regard to details about the cement composition, mixture proportions, and aggregate mineralogy, and

(2) More in-depth monitoring activities, particularly of the moisture and stress states of the concrete.

While the AAR classification models currently seem best-suited to limited diagnostic use, i.e., to facilitate more confident and rapid deployment of AAR mitigation measures, their accuracy and applicability is likely to improve upon the development of either:

(1) Larger, more detailed datasets, and/or

(2) Improved "cost-sensitive" ML algorithms, potentially qualifying them for future application to risk assessment or even concrete mix design.

5 References

[1] Rajabipour F, Giannini E, Dunant C, Ideker JH, Thomas MD (2015) Alkali–silica reaction: Current understanding of the reaction mechanisms and the knowledge gaps. Cem Concr Res 76:130–146. https://doi.org/10.1016/j.cemconres.2015.05.024

[2] Young B, Hall A, Pilon L, Gupta P, Sant G (2019) Can the compressive strength of concrete be estimated from knowledge of the mixture proportions?: New insights from statistical analysis and machine learning. Cem Con Res 115:379-388. https://doi.org/10.1016/j.cemconres.2018.09.006

[3] Oey T, Jones S, Bullard JW, Sant G (2020) Machine learning can predict setting behavior and strength evolution of hydrating cement systems. J Am Ceram Soc 103:480–490. https://doi.org/10.1111/jace.16706

[4] Allahyari H, Heidarpour A, Shayan A, Nguyen VP (2020) A robust time-dependent model of alkali-silica reaction at different temperatures. Cem Concr Compos 106:103460. https://doi.org/10.1016/j.cemconcomp.2019.103460

[5] Brownlee J (2016) Machine Learning Mastery. Machine Learning Mastery Pty Ltd.

[6] Nummelin M, Äijälä M (2018) Taitorakenteiden erikoistarkastusten laatuvaatimukset - Sillat. https://www.google.com/url?sa=t&rct=j&q=&esrc=s&source=web&cd=1&cad=rja&uact=8&ved=2ahUKEwiEwMKw4OTmAhVow4sKHX-8CsUQFjAAegQIBBAC&url=https%3A%2F%2Fjulkaisut.liikennevirasto.fi%2Fpdf8%2Flo_2018-28_taitorakenteiden_erikoistarkastusten_web.pdf&usg=AOvVaw163JCX1pvtux_55gggYQcw. Accessed 2 January 2020.

[7] Nummelin M, Äijälä M (2017) Sillantarkastuskäsikirjan sovellusohje. https://www.google.com/url?sa=t&rct=j&q=&esrc=s&source=web&cd=1&cad=rja&uact=8&ved=2ahUKEwjZv-_n4OTmAhWow4sKHbmKAeUQFjAAegQIAhAC&url=https%3A%2F%2Fjulkaisut.liikennevirasto.fi%2Fpdf8%2Fohje_2017_sillantarkastuskasikirjan_sovellusohje_web.pdf&usg=AOvVaw2A6DbKCBHpF8aVKpqZuv6T. Accessed 2 January 2020.

[8] Godart B, Rooij M de, Wood J (2013) Guide to diagnosis and appraisal of AAR damage to concrete in structures. Springer Verlag, New York.

[9] Voltolini M, Marinoni N, Mancini L (2011) Synchrotron X-ray computed microtomography investigation of a mortar affected by alkali–silica reaction: a quantitative characterization of its microstructural features. J Mater Sci 46:6633–6641. https://doi.org/10.1007/s10853-011-5614-5

[10] Clayton DA, Ezell ND, Albright A, Santos-Villalobos HJ (2018) Detecting alkali-silica reaction in thick concrete structures using linear array ultrasound. In: Shull PJ (ed) Nondestructive Characterization and Monitoring of Advanced Materials, Aerospace, Civil Infrastructure, and Transportation XII. SPIE, p 4.

[11] Ezell NDB, Albright A, Floyd D, Clayton D, Khazanovich L (2019) A novel use of frequency-banded synthetic aperture focusing technique for reconstructions of alkali-silica reaction in thick-reinforced concrete structures. In: AIP Conf Proc 2102:110003. AIP Publishing LLC, Melville.

[12] Multon S, Toutlemonde F (2006) Effect of applied stresses on alkali–silica reaction-induced expansions. Cem Concr Res 36:912–920. https://doi.org/10.1016/j.cemconres.2005.11.012

[13] Pignatelli R, Comi C, Monteiro PJM (2013) A coupled mechanical and chemical damage model for concrete affected by alkali–silica reaction. Cem Concr Res 53:196–210. https://doi.org/10.1016/j.cemconres.2013.06.011

[14] Kristiansen K, Valtiner M, Greene GW, Boles JR, Israelachvili JN (2011) Pressure solution–The importance of the electrochemical surface potentials. Geochim Cosmochim Acta 75:6882-6892.

[15] Greene GW, Kristiansen K, Meyer EE, Boles JR, Israelachvili JN (2009) Role of electrochemical reactions in pressure solution. Geochim Cosmochim Acta 73:2862-2874.

[16] Pignatelli I, Kumar A, Alizadeh R, Le Pape Y, Bauchy M, Sant G (2016) A dissolution-precipitation mechanism is at the origin of concrete creep in moist environments. J Chem Phys 145:054701. https://doi.org/10.1063/1.4955429

[17] Pignatelli I, Kumar A, Bauchy M, Sant G (2016) Topological Control on Silicates' Dissolution Kinetics. Langmuir 32:4434–4439. https://doi.org/10.1021/acs.langmuir.6b00359

[18] Oey T, Kumar A, Pignatelli I, Yu Y, Neithalath N, Bullard JW, Bauchy M, Sant G (2017) Topological controls on the dissolution kinetics of glassy aluminosilicates. J Am Ceram Soc 100:5521–5527. https://doi.org/10.1111/jace.15122

[19] Nesse W (2012) Introduction to mineralogy. Oxford University Press, New York.

[20] Shelby J (2005) Introduction to glass science and technology. Royal Society of Chemistry, London.

Coupled constitutive equations for assessing mechanical effects of Internal Swelling Reactions

Equações constitutivas acopladas para avaliação dos efeitos mecânicos das reações expansivas de origem interna do betão

Bruno D. Regnicoli Benitez
Jean-François Seignol
Boumediene Nedjar

Abstract

Internal swelling reactions (*ISR*) in concrete can have significant impact on the long-term behaviour of massive concrete structures. This communication presents the foundations of a constitutive model developed within the framework of the finite-element method. In order to reach, in further step, a correct quantification of the visible crack patterns, we first develop a set of evolutive constitutive equations based on Larive's law and taking into account the main couplings that affect *ISR* in structures: chemical extent, available moisture, past and present temperature, and creep.

First, the aim of this modelling framework is presented by setting the set of constitutive equations and identifying material parameters on the base of observable data. Then we describe the evolution equation governing the chemical expansion. The third part focuses on coupling with various phenomena. Finally, we propose perspectives about material damage and cracking in concrete.

Keywords: Constitutive equations / Coupling / Numerical model / Parameter identification

Resumo

As reações expansivas de origem interna do betão podem ter um impacto significativo no comportamento a longo prazo de estruturas maciças de betão. Esta comunicação apresenta os fundamentos de um modelo constitutivo, desenvolvido no âmbito do método dos elementos finitos. Para se conseguir, numa etapa posterior, uma adequada interpretação dos padrões de fendilhação superficial, desenvolveram-se equações constitutivas evolutivas, com base na lei de Larive, tendo em consideração os principais acoplamentos que afetam as reações expansivas nas estruturas: afinidade química, humidade, temperatura e fluência.

Em primeiro lugar, a abordagem de modelação é apresentada através de um conjunto de equações constitutivas, identificando os parâmetros materiais com base em dados da observação. Em seguida, apresenta-se a equação de evolução química da expansão. A terceira parte diz respeito ao acoplamento dos vários fenómenos. Finalmente, fazem-se propostas relativas ao dano e à fendilhação do betão.

Palavras-chave: Equações constitutivas / Acoplamento / Modelo numérico / / Identificação de parâmetros

Bruno D. Regnicoli Benitez

University Gustave Eiffel
Marne-la-Vallé, France
bruno.regnicoli@univ-eiffel.fr

Jean-François Seignol

University Gustave Eiffel
Marne-la-Vallé, France
jean-francois.seignol@univ-eiffel.fr

Boumediene Nedjar

University Gustave Eiffel
Marne-la-Vallé, France
boumediene.nedjar@univ-eiffel.fr

REGNICOLI BENITEZ, B. [*et al.*] – Coupled constitutive equations for assessing mechanical effects of internal swelling reactions. **Revista Portuguesa de Engenharia de Estruturas**. Ed. LNEC. Série III. n.º 15. ISSN 2183-8488. (março 2020) 77-84.

1 Scope and motivation

The structural behaviour analysis of structures affected by internal swelling reactions (*ISR*) as well as the prediction of their future behaviour and the assessment to their lifespan requests the use of numerical models. These models need to be precisely fitted to be relevant, which is often difficult to achieve because information about concrete or construction conditions can be scarce or missing in the case of old structures. The only trustable information is often those directly observed *in situ*: crack patterns or physical quantities collected from monitoring systems. This information is essential in the adjustment of the model to each case study conditions and the model should be able to simulate, in the most realistic way possible, the different phenomena involved.

Two kind of *ISR* pathologies are considered: the Alkali-Silica Reaction (*ASR*) and the Delayed Ettringite Formation (*DEF*). While for the former, the chemical reaction happens between alkalis in the cement paste and the reactive silica aggregates, the latter is caused by the formation of ettringite in concrete when subjected to high temperature during cement hydration, and later exposed on to moisture. In both cases, the hardened concrete expands progressively which can potentially lead to cracking and structural disorders, to mention a few. It is then of major importance to build numerical tools that can simulate these expanding mechanisms and their consequences on the structural serviceability. For both phenomena, it is unanimously admitted that *ISR* develops when concrete is at high humidity above a certain threshold, or in contact with water.

Extensive research has been conducted so far to model the expansions caused by *ASR* [1–5]. Later on, models have been developed for *DEF* as well, see for example [6–8]. From the mathematical point of view, the models are mostly based on phenomenological approaches formulated in terms of internal variables that can be deployed to feed constitutive relations and evolution laws that must be integrated in a sound way within boundary-value problems that, in a last step, must be solved numerically for the response of concrete structures. This constitutes a good compromise between efficiency and representativity of the complex concrete behaviour.

The *ISR* expansion is in general characterized by two important factors: amplitude, and kinetics. Both are in turn dependent on the humidity level, and on temperature. Hence, by nature, the complete problem at hand is a coupled one thermo-hydro-mechanics. Moreover, other phenomena must be accounted for, e.g., creep, damage, plasticity. In this contribution, details on the creep modelling are given through viscoelastic strain-like internal variables. The plasticity formulation is nowadays classical and is not described for the sake of clarity.

2 General framework for constitutive equation

2.1 Kinematics

Within the continuum, the kinematical choice made in such developments is based on the additive split of the total strain tensor ε into an elastic part $\varepsilon^{(E)}$ and complementary parts, each one corresponding to a specific phenomenon. we assume that the total strain is the sum:

$$\varepsilon=\varepsilon^{(E)}+\varepsilon^{(T)}+\varepsilon^{(H)}+\varepsilon^{(\chi)}+\varepsilon^{(C)}+\varepsilon^{(P)} \tag{1}$$

where $\varepsilon^{(T)}$ and $\varepsilon^{(H)}$ are respectively the temperature-induced strain and the hygric-induced strain, $\varepsilon^{(X)}$ is the free chemical strain, $\varepsilon^{(C)}$ is the basic creep strain and $\varepsilon^{(P)}$ is the plastic strain.

If θ_0 is defined as the reference temperature and θ as an arbitrary temperature, the thermal strains caused by a change in temperature of an unconstrained isotropic volume are given by:

$$\varepsilon^{(T)}=k_T\left(\theta-\theta_0\right)\mathbf{1} \tag{2}$$

where k_T is the coefficient of thermal expansion. Here and in all what follows, **1** denotes the second-order identity tensor. Following the same logic, the volumetric strain due to a change in the degree of saturation $\varepsilon^{(H)}$ is given by:

$$\varepsilon^{(H)}=k_S\left(S_R-S_{R,0}\right)\mathbf{1} \tag{3}$$

with $S_{R,0}$ is the reference degree of saturation, S_R is an arbitrary value of the degree of saturation and k_S is the linear coefficient of hygric expansion. The concrete shrinkage/swelling can easily be expressed in terms of relative humidity too, rather than in terms of degree of saturation.

More complex relationships can be found in the literature for the drying of concrete and for the expression of k_S and k_T. However, a linear relationship between saturation degree and expressing the two coefficients, k_S and k_T respectively, by a constant value are reasonable approximations within the framework of the present model.

Eventually, the free volumetric *ASR* strain is given by:

$$\varepsilon^{(x)}=\varepsilon^{X}\mathbf{1} \tag{4}$$

with $\varepsilon^X = \varepsilon^X$ (t, θ) is the free chemical expansion.

2.2 Chemical kinetics

The macroscopic phenomena of *ASR* are modelled within the framework of the porous continua theory, extended to reactive partially saturated porous media [9]. Then, in order to take into account the diffusion conditions as the alkaline reaction develops, as well as accurately representing the sigmoidal chemical expansion-time curve, the model was calibrated on the basis of the extensive and rigorous experimental campaign published in [1].

It follows that the *ASR* strain-induced can be represented as:

$$\varepsilon^{x}=\varepsilon_{\infty}\frac{1-exp\left(-\dfrac{t}{\tau_C}\right)}{1+exp\left(-\dfrac{t+\tau_L}{\tau_C}\right)}; \tag{5}$$

From Equation (5) the chemical expansion can be represented through three parameters, namely, ε_∞ which is the asymptotic volumetric expansion strain in the stress-free experiment, together with the characteristic time τ_C and the latency time τ_L of *ASR* swelling.

The previous formulation may also be extended to the case of structures affected by Delayed Ettringite Formation – *DEF*, see for instance [7, 8]. However, the difference lays in the asymptotic volumetric expansion strain; in case of *ASR* ε_∞ is a constant parameter, deduced from experimental tests and depends on the type of concrete, whereas in case of *DEF* $\varepsilon_\infty \equiv \varepsilon_\infty(\boldsymbol{x})$ is a field variable that depends on the thermal history. In order to take into account this strong dependance the following model, based on experimental work by [10], has been proposed in [6, 7]:

$$\varepsilon_\infty=\alpha\int_0^{t_m}\begin{cases}0 & if\ \theta\leq\theta_{DEF}\\ e^{\left[\frac{E_\alpha^{DEF}}{R}\quad\frac{1}{\theta-\theta_{DEF}}\right]} & if\ \theta>\theta_{DEF}\end{cases}dt \tag{6}$$

with α is a parameter which accounts for material properties influencing swelling development (cement, aggregates ...), θ_{DEF} is the temperature threshold above which *DEF* occurs, E_α^{DEF} is the activation energy, R is the universal gas constant and t_m is the maturation time.

An alternative formulation can be found in [11, 12]. In any case, during the mechanical analysis, the field $\varepsilon_\infty(\boldsymbol{x})$ is known, which plays a key role in the design of the algorithm.

In the case of constant or monotonically increasing temperature and humidity chemical strain can be expressed by Equation (5). In the case of variable temperature and humidity, characterised even by decreasing functions, the expansion should take into account its irreversibility during time. Within the continuum thermodynamic framework, developing the formulations presented in [1, 2], it can be deduced that the swelling evolution equation can be expressed as follows:

$$\left[\tau_C\ \varepsilon_\infty\left(1+e^{\frac{T_L}{T_C}}\right)\right]\dot{\varepsilon}^X+\left(e^{\frac{T_L}{T_C}}\right)\varepsilon^{\chi^2}+\left[\varepsilon_\infty\left(1-e^{\frac{T_L}{T_C}}\right)\right]\varepsilon^X=\varepsilon_\infty{}^2. \tag{7}$$

2.2.1 Temperature dependance

In endothermic reactions, an increase in temperature normally increases the speed of reaction since the energy added to the system allows an easiest combination of reactive ions. This physical result is reinforced, for alkaline reactions, by the way in which accelerated testing is carried out, i.e., high storage temperatures are used in order to accelerate the development of chemical reactions over a period of months, rather than years, time typically needed for *AAR* to develop within the concrete of structures exposed to the natural environment, [4, 13].

The reaction kinetics are highly dependent on temperature, particularly it has been experimentally demonstrated that temperature dependance of time constants τ_C and τ_L matching the Arrhenius equation:

$$\tau_C\left(\theta\right)=\tau_C\left(\theta_0\right)exp\left[U_C\left(1/\theta-1/\theta_0\right)\right] \tag{8}$$

$$\tau_L\left(\theta\right)=\tau_L\left(\theta_0\right)exp\left[U_L\left(1/\theta-1/\theta_0\right)\right] \tag{9}$$

θ_0 is the reference temperature of expansion test, U_C and U_L are the activation energy constants which cause the thermo-activation of the characteristic and latent times respectively.

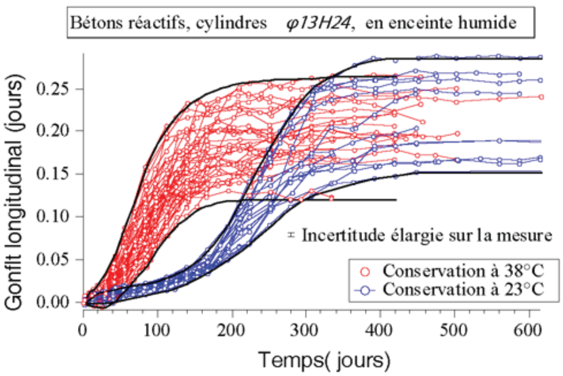

Figure 1 Free expansion from Larive's tests; [1]

2.2.2 Variable moisture conditions

Water plays a dual role in the development of *ASR*: on the one hand, it acts as a carrier for the alkali and hydroxyl ions, allowing the reaction to progress; on the other hand, it is absorbed by the alkali-silica gel which swells, generating the pressure required to crack the concrete [14]. It is widely recognised that below a threshold value of relative humidity (RH = 80-85 %) *ASR* does not occur, [1, 15], and that above this value the expansion increases exponentially, Figure 2.

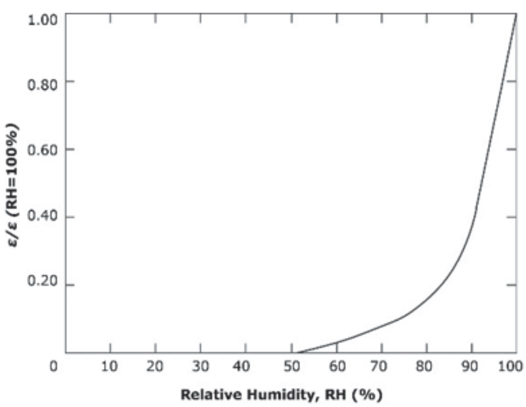

Figure 2 Influence of environmental conditions on chemical expansion: Effect of relative humidity, [16]

Experimental concrete affected by *ASR* also shows a significant dependence between free expansion and variable moisture conditions, [17–21].

In order to simulate the dependence of *ASR* on humidity, and more generally on environmental conditions, mathematical models have been proposed in literature, which take into account the humidity either by reduction functions, [22], or altering the kinetic laws, [20, 21, 23].

Within this framework, an alternative model able to take into account variable humidity conditions is proposed. In order to capture the moisture effect on the chemical evolution, we use the concept of effective time t_{eff}, introduced in [24, 25], such as:

$$\dot{t}_{eff} = \dot{t}_{eff}\left(S_R, t\right) \quad \in \left[0,1\right] \tag{10}$$

Now, if $S_{R,\text{thrs}}$ denotes the degree of saturation for which the reaction occurs, we have that:

$$\begin{cases} \varepsilon^X = 0 & if\ S_R < S_{R,thrs} \\ \dot{\varepsilon}^X > 0 & if\ S_R \geq S_{R,thrs} \end{cases} \tag{11}$$

Where $\dot{\varepsilon}^X$ is the chemical strain due to *ASR*, and in the case of constant or monotonically increasing temperature and humidity can be expressed by Equation (5).

The following is a possible option for embedding humidity dependence in chemical evolution equation:

$$t_{eff} = \int_0^t \left(\frac{\left\langle S_R - S_{R,thrs} \right\rangle_+}{1 - S_{R,thrs}} \right)^m dt \tag{12}$$

where m is a parameter that depends on the degree of saturation and $\langle\ \rangle_+$ denotes the positive part. Furthermore, and besides on the above features, if the final expansion amplitude depends on the level of saturation too, a possible choice to link could be:

$$\varepsilon_\infty\left(S_R\right) = \varepsilon_\infty\left(S_{R,1.0}\right) \cdot \left(\frac{\left\langle S_R - S_{R,thrs} \right\rangle +}{1 - S_{R,thrs}} \right)^{m_\infty} \tag{13}$$

where m_∞ is a material parameter that can be identified from free expansion tests carried out at different degree of saturation.

2.3 Visco-elastic behaviour

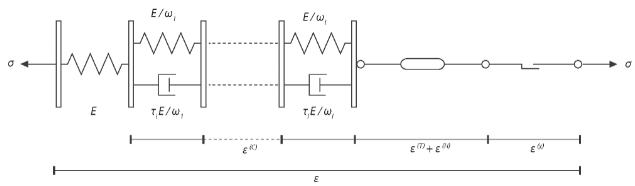

Figure 3 One-dimensional viscoelastic rheological model.

In this framework, creep strain $\varepsilon_{ij}^{(C)}$ is treated as an internal variable, and can be composed of as many contributions as necessary as follows:

$$\varepsilon^{(C)} = \sum_{i=1}^{l} \varepsilon_i^{(C)} \tag{14}$$

Where the $i = 1,\ldots l$ hidden variables $\varepsilon_i^{(C)}$ characterize viscoelastic processes with corresponding relaxation times $\tau_i \in [0,+\infty]$, $i = 1,\ldots l$. The way all these internal variables evolve is motivated by the generalized Kelvin-Voigt rheological model, Figure 3. In this case, the complementary evolution equations that govern the creep strain components are given by (for further information see [26]):

$$\dot{\varepsilon}_i^{(C)} + \frac{1+\omega_i}{\tau_i}\mathbb{N}:\varepsilon_i^{(C)} + \frac{\omega_i}{\tau_i}\sum_{j=1,j\neq i}^{l}\mathbb{N}:\varepsilon_j^{(C)} = \frac{\omega_i}{\tau_i}\mathbb{N}:\left(\varepsilon-\varepsilon^{(T)}-\varepsilon^{(H)}-\varepsilon^{(X)}\right),\ \ i=1,\dots l \tag{15}$$

where ω_i, $i = 1, \dots l$ are material parameters. Here $\mathbb{N}$ is the fourth-order tensor which depends solely on the Poisson's ratio ν. In Voigt engineering notation, it is given by:

$$\mathbb{N} = \frac{1}{(1+\nu)(1-2\nu)}\begin{bmatrix} 1-\nu & \nu & \nu & & & \\ \nu & 1-\nu & \nu & & & \\ \nu & \nu & 1-\nu & & & \\ & & & 1-2\nu & & \\ & & & & 1-2\nu & \\ & & & & & 1-2\nu \end{bmatrix} \tag{16}$$

2.4 Constitutive equations and mechanical equilibrium

In the case of a linear elastic relationship for reversible material behaviour, the constitutive relationship can be expressed as follows:

$$\sigma = C:\left(\varepsilon-\varepsilon^{(T)}-\varepsilon^{(H)}-\varepsilon^{(X)}-\varepsilon^{(C)}-\varepsilon^{(P)}\right) \tag{17}$$

where σ is the stress tensor, $\mathbf{C}$ is the fourth-order elasticity tensor within which a damage mechanism can be introduced as:

$$C = (1-d_X)C_0 \tag{18}$$

where $\mathbf{C}_0$ is the elastic modulus for the undamaged concrete and d_X is a damage variable in the sense of continuum damage mechanics. Indeed, the latter can be related to the chemical expansion explicitly as a function of the quantity $\varepsilon^{(X)}$as follows [7]:

$$d_X = 1-exp\left[-\beta\left\langle\varepsilon^{(X)}-\varepsilon_{thrs}\right\rangle+\right] \tag{19}$$

where ε_{thrs} is the strain-like chemical damage threshold, and $\beta \geq 0$ is a parameter that determines chemical damage occurrence, i.e. for β no swelling damage occurs.

2.5 Outlines of the F.E. approximation

2.5.1 Variational formulation

If we consider the weak form of mechanical equilibrium, without taking into account the effects of creep or plasticity, then we will have at the actual time t_{n+1}:

$$\int_B \nabla^s\delta\mathbf{u}:C_{n+1}:\nabla^s\mathbf{u}_{n+1}\,dV = G_{n+1}^{ext}(\delta\mathbf{u}) + \int_B \nabla^s\delta\mathbf{u}:C_{n+1}:\left(\varepsilon_{n+1}^{T}+\varepsilon_{n+1}^{H}+\varepsilon_{n+1}^{\chi}\right)dV \tag{20}$$

Which must hold for any variation of displacements $\delta\mathbf{u}$, and where ∇^s is the symmetric gradient operator. Here G_{n+1}^{ext} is a shorthand notation for the virtual work of the external loads embedding both of the volumetric forces in the body $\boldsymbol{B}$ and traction forces on part of its boundary $\delta_t\,\boldsymbol{B} \subset \delta\boldsymbol{B}$ applied at time t_{n+1}. Equation (20) is to be solved for the actual displacement field $\mathbf{u}_{n+1}$.

The evaluation of the swelling strain ε_{n+1}^{X} in Equation (20) is carried out through the concept of effective time t_{n+1}^{eff}, which is updated locally at each time step as:

$$t_{n+1}^{eff} = t_n^{eff} + \left(\frac{\left\langle S_{R,n+1}-S_{R,thrs}\right\rangle}{1-S_{R,thrs}}\right)^{m_{n+1}}\Delta t \tag{21}$$

Where $\Delta_t = t_{n+1} - t_n$ is the real time increment, and m_{n+1} is evaluated at the saturation degree value $S_{R,n+1}$. Consequently, the effective time is treated as an internal field variable; $t^{eff} = t^{eff}(\mathbf{x}, t)$, i.e. within the finite element method the storage is performed at the Gauss points level.

2.5.2 Iterative resolution procedure

In order to extend the use of Equation (20) to non-linear phenomena, such as creep, plastic behaviour, damage mechanics, among others, its resolution is based on an iterative resolution. Hence, assuming a known state $\mathbf{u}_{n+1}$ at time t_n, one then solves iteratively the following linearized form for the increment of the displacement field:

$$\int_B \nabla^s\delta\mathbf{u}:\tilde{C}_{n+1}:\nabla^s(\Delta\mathbf{u})\,dV = G_{n+1}^{ext}(\delta\mathbf{u}) - \int_B \nabla^s\delta\mathbf{u}:\sigma_{n+1}^{(i)}\,dV \tag{22}$$

Where, initially for $i=0$, $\sigma_{n+1}^{(0)}=\sigma_n$. The right-hand side in Equation (22) constitutes the residual of the mechanical balance that is used to test the convergence of the iterative process, and $\tilde{C}_{n+1}$ is the tangent modulus, whether algorithmic or continuous, computed as:

$$\tilde{C}_{n+1} = \frac{\sigma_{n+1}^{(i)}}{\partial\varepsilon} \tag{23}$$

Equation (22) is solved together with the appended local evolution equations to update the set of internal variables, i.e. plasticity and/or creep and/or damage. At the end of each global iteration, the displacement field is updated as:

$$\mathbf{u}_{n+1}^{(i+1)} = \mathbf{u}_{n+1}^{(i)} + \Delta\mathbf{u} \tag{24}$$

3 Numerical examples

In this section, two numerical examples are presented within the framework of the finite element method. The first one shows the coupling between creep and expansion of a concrete sample, while the second one shows the structural effects of internal reinforcement.

3.1 Basic creep coupled to *ISR*

It is well known that creep plays a dominant role in the long terms response of concrete structures subjected to constant loads. It is suspected that under swelling due to chemical reaction, the coupling with creep can be more evident. In this first example, we consider cylindrical samples submitted to two levels of axial compressive stress, with uniform relative humidity; one under the swelling threshold where only basic creep takes place, and one at complete saturation where *ISR* is full evolving. More precisely, the following four computations are considered:

i) Axial compressive stress at 10 *MPa*, with and without *ISR*;

ii) Axial compressive stress at 20 *MPa*, with and without *ISR*.

For the concrete, we use E = 20.5 GPa for the Young's modulus, and $\nu = 0.2$ for the Poisson's ratio. For the chemical expansion we choose the parameters:

$$\varepsilon_\infty = 0.4\%,\ \tau_C = 70\ days, \text{ and } \tau_L = 0,$$

And for the basic creep, we use only one mechanism with parameters: $\omega_1 = 1.5$ and $\tau_1 = 150\ days$.

Figure 4 shows the four curves. One can see that, from these computations, the expansion due to *ISR* shows a decrease due to the compressive stress.

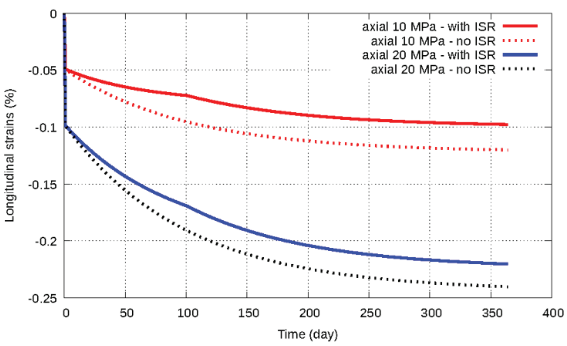

Figure 4 Creep simulations: longitudinal strain evolution for the different compression levels

3.2 Effect of internal reinforcement

This second example is inspired by a JCI-benchmark example carried out on alkali-aggregate expansion experiments, see for example [27]. Here cylindrical specimens have been considered instead of prismatic ones. They have been constrained uniaxially as shown in Figure 5. Rigid plates on the samples' ends are linked by a steel rebar. Three cases are considered in this set of examples:

i) a rebar of diameter 6 mm that corresponds to a reinforcement ratio of 0.22%;

ii) a rebar of diameter 12 mm that corresponds to a reinforcement ratio of 0.88%;

iii) a rebar of diameter 18 mm that corresponds to a reinforcement ratio of 1.99%.

For the sound concrete, we use $E = 25\ GPa$ for the Young's modulus, and $\nu = 0.2$ for the Poisson's ratio. For the chemical expansion we choose the parameters:

$$\varepsilon_\infty = 0.7\%,\ \tau_C = 40\ days, \text{ and } \tau_L = 0.$$

Under fully saturated hydric conditions, the concrete "free" expansion is shown in Figure 5, red curve. Notice that as constant thermo-hydric conditions are considered in all that follows, there is no need to specify the values of the parameters k_T and k_S for the thermo-hydric strains.

For the steel rebars, we consider an elastic-perfectly plastic constitutive relation with the von Mises yield criterion. The parameters we choose are:

$$E_S = 210\ GPa,\ \nu_s = 0.2, \text{ and yield stress } \sigma_y = 550\ MPa.$$

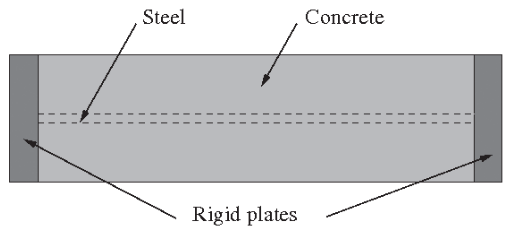

Figure 5 Expansion specimen with a steel rebar

The problem has been discretized by using an axisymmetric analysis. Figure 6 shows the evolution of the mean longitudinal strain within the concrete specimens for the above mentioned reinforcement ratios and for an unreinforced concrete (red curve), which correspond to a free-expansion.

For the measured longitudinal strains on reinforced and unreinforced specimens, it has been observed that for the highest reinforcement ratio (here with 1.99%, green curve), the elastic strain limit is not reached within the steel rebar. This is not the case for the remaining reinforcement ratios (0.88% and 0.22% ratios, respectively, blue and black curves), where, according to the stress-strain relationship considered, the reinforcements are such that plastic yield stress has been reached in the rebars.

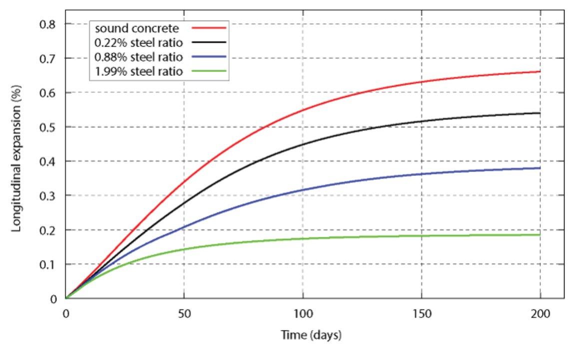

Figure 6 Longitudinal expansions evolutions for the different steel ratios

4 Conclusion and perspectives

In the present study, a numerical tool has been developed for modelling *ISR* under variable environmental conditions.

The swelling development has been formulated within the framework of continuous thermodynamics, which also allows irreversible phenomena to be taken into account. Both temperature and relative humidity play a key role in the development of *ISR*. In the present model, the concept of "effective time" has been introduced into the swelling kinetic law to account for variable humidity, instead, the dependence on past and present temperature are included within the two time constants of the reaction, the characteristic and latency time.

In order to perform efficient structural calculations, the model covers different mechanisms observable in concrete including creep, drying shrinkage, thermal dilatation and plastic behaviour. Viscous phenomena have been modelled through a generalised Kelvin-Voigt rheological model to formulate the whole behaviour. Long-term and short-term relaxation processes can be integrated into the model by means of all necessary viscoelastic processes.

The effectiveness of this model has been demonstrated in two numerical examples. The first focuses on the analysis of coupling between creep and *ISR*, while the second example investigates the swelling strain due to *ASR/DEF* over time in reinforced concrete specimens. The numerical results highlighted the relevance of taking into account the interaction between these phenomena when formulating a numerical model to predict the evolution of strain swelling.

Future work will focus on investigating the correlation between visible damage and cracking on the facing and the internal physical and structural state of an affected structure. This will contribute to enhanced structural analysis of existing structures such as bridges, dams, nuclear power plants, affected by ISR.

5 References

[1] Larive, C. (1997) – Apports combinés de l'expérimentation et de la modélisation à la compréhension de l'alcali-réaction et de ses effets mécaniques. Université Paris Est.

[2] Li, K.; Ulm, F.J.; Coussy, O. *et al* (2000) – Chemoelastic modelling of ASR in concrete. In: 11th International conference on alkali aggregate reaction. Québec, pp 989-998.

[3] Ulm, F.J.; Coussy, O.; Li, K.; Larive, C. (2000) – Thermo-chemo-mechanics of ASR expansion in concrete structures. J Eng Mech © ASCE 233-242.

[4] LCPC (1997) – Alcali-réaction du béton Essai d'expansion résiduelle sur béton durci, Projet de. Techniques et méthodes des Laboratoires des Ponts et Chaussées.

[5] Multon, S.; Seignol, J.F.; Toutlemonde, F.; (2005) – Structural behavior of concrete beams affected by alkali-silica reaction. ACI Mater. J. 102:67–-76.

[6] Baghdadi, N.; Seignol, J.; Toutlemonde, F. (2007) – Modélisation du couplage chimico-mécanique pour calculer une structure en béton atteinte de réaction sulfatique interne. In: 18ème Congrès Français de Mécanique, 18ème Congrès Français de Mécanique Grenoble. Grenoble, pp 27-31.

[7] Seignol, J.F.; Baghdadi, N.; Toutlemonde, F. (2009) – A macroscopic chemo-mechanical model aimed at re-assessment of delayed-ettringite-formation affected concrete structures. In: The first international conference on computational Technologies in Concrete Structures (CTCS'09). Jeju, Corea.

[8] Baghdadi, N. (2008) – Modélisation du couplage chimico-mécanique d'un béton atteint d'une réaction sulfatique interne. Ecole Nationale des Ponts et Chaussées.

[9] Coussy, O. (1996) – Mechanics of porous continua. IEEE Electr. Insul. Mag. 12:49.

[10] Brunetaud, X. (2005) – Etude de l'influence de différents paramètres et de leurs interactions sur la cinétique et l'amplitude de la réaction sulfatique interne au béton. Ecole centrale de Paris.

[11] Martin, R.P. (2010) – Analyse sur structures modèles des effets mécaniques de la réaction sulfatique interne du béton. Université Paris Est.

[12] Martin, R.P.; Bazin, C.; Billo, J. *et al* (2012) – Experimental Evidence for Understanding Def Sensitivity To Early-Age Thermal History. CONCRACK 3 – RILEM-JCI Int Work Crack Control Mass Concr Relat Issues Concern Early-Age Concr Struct 1-10.

[13] LCPC (2009) – Réaction sulfatique interne au béton - Essai d'éxpansion résiduelle sur carotte de béton extraite de l'ouvrage, Les collec. Paris.

[14] Sims, I.; Poole, A.B. (2017) – Alkali-aggregate reaction in concrete: A world review. Taylor and Francis.

[15] Larive, C.; Laplaud, A.; Coussy, O. (2000) – The Role of Water in Alkali-Silica Reaction. In: International conference, Alkali-aggregate reaction in concrete; 2000. ICON/CANMET, Quebec City, Canada, pp 61-70.

[16] Poole, A.B. (1992) – The alkali-silica reaction in concrete. Blackie u.a., London u.a.

[17] Multon, S.; Seignol, J.F.; Toutlemonde, F. (2005) – Structural behavior of concrete beams affected by alkali-silica reaction. ACI Mater J 102:67–76. https://doi.org/10.14359/14299.

[18] Multon, S.; Seignol, J.F.; Toutlemonde, F. (2006) – Concrete beams submitted to various moisture environments. Struct Eng Mech 22:71-83. https://doi.org/10.12989/sem.2006.22.1.071.

[19] Multon, S.; Toutlemonde, F. (2010) – Effect of moisture conditions and transfers on alkali silica reaction damaged structures. Cem Concr Res 40:924–934. https://doi.org/10.1016/j.cemconres.2010.01.011.

[20] Poyet, S. (2003) – Etude de la degradation des ouvrages en beton atteints par la reaction alcali-silice - approche experimentale et modelisation numerique des degradations dans un environnement hydro-chemo-mecanique variable. Université de Marne-la-vallé.

[21] Poyet, S.; Sellier, A.; Capra, B. *et al* (2006) – Influence of Water on Alkali-Silica Reaction: Experimental Study and Numerical Simulations. J Mater Civ Eng 18:588–596. https://doi.org/10.1061/(asce)0899-1561(2006)18:4(588).

[22] Capra, B.; Bournazel, J.P. (1998) – Modeling of induced mechanical effects of alkali-aggregate reactions. Cem Concr Res 28:251-260. https://doi.org/10.1016/S0008-8846(97)00261-5.

[23] Li, K. (2002) – Modélisation chimico-mécanique du comportement des béetons affectés par la réeaction d'alcali-silice et expertise numéerique des ouvrages d'art déegradés. PhD Thesis - ENPC 1-219.

[24] Nedjar, B.; Rospars, C.; Martin, R.P.; Toutlemonde, F. (2021) – Benchmark Study Results: IFSTTAR. In: RILEM Technical Committee 259-ISR, Diagnosis & Prognosis of AAR Affected Structures, Ed. V. Sao. Springer Science+Business Media B.V., pp 427-437.

[25] Malbois, M.; Nedjar, B.; Lavaud, S. *et al* (2019) – On DEF expansion modelling in concrete structures under variable hydric conditions. Constr Build Mater 207:396–402. https://doi.org/10.1016/j.conbuildmat.2019.02.142.

[26] Nedjar, B.; Le Roy, R. (2013) – An approach to the modeling of viscoelastic damage. Application to the long-term creep of gypsum rock materials. Int J Numer Anal Methods Geomech 37:1066-1078. https://doi.org/10.1002/nag.1138.

[27] Ishikawa, T.T.; Y. (2017) – Chemical Expansion Effect in Concrete and its Numerical Simulation Based on the Mechanical Energy Conservation Hypothesis. In: JCI-RILEM International Workshop on Control of Mass Concrete and Related Issues Early Age Cracking of Structures (CONCRACK). TOKYO, Japan, pp 161-174.

Structural behavior of Pracana dam 30 years after rehabilitation due to severe ISR-ASR damage

Comportamento estrutural da barragem de Pracana 30 anos após as obras de reabilitação devidas às graves deteriorações provocadas pela RSI-RAS

José Piteira Gomes
Domingos Silva Matos
António Lopes Batista
José Ilídio Ferreira

Abstract

The Pracana dam is a 60 m high buttress structure, completed in 1951, built with a concrete mix including quartzite and granite aggregates. Since the first filling of the reservoir, an abnormal behavior has been observed, characterized by progressive vertical and horizontal displacements and intense cracking, due to RSI-RAS. The evolution of deteriorations and the insufficient capacity of the spillway led to the decision to empty the reservoir in 1980.

Between 1988 and 1992, the dam owner, EDP – Energias de Portugal, carried out major rehabilitation works, which included the waterproofing of the upstream surface with a geomembrane, the regeneration of the concrete, the construction of two alignments of concrete struts connecting the base of the buttress webs and the modernization and reinforcement of the monitoring system.

This paper presents the results of the analysis of the behavior observed since the refilling of the reservoir, in December 1992, which shows the impact of the rehabilitation works on the dam's behavior, namely the very significant decrease in the rate of the reactions development, although of non-uniform shape throughout the structure.

Keywords: Pracana dam / ISR-ASR damage / Rehabilitation / Monitoring / /Structural condition

Resumo

A barragem de Pracana é uma estrutura de contrafortes com 60 m de altura, concluída em 1951, construída com betão de agregados quartzíticos e graníticos. Desde o primeiro enchimento da albufeira observou-se um comportamento anormal, caracterizado por deslocamentos verticais e horizontais progressivos e intensa fendilhação, devidos à RSI-RAS. A evolução das deteriorações e a insuficiente capacidade do descarregador de cheias conduziram à decisão de esvaziar a albufeira em 1980.

Entre 1988 e 1992 foram realizadas, pelo concessionário da barragem, a EDP – Energias de Portugal, obras de reabilitação de grande envergadura, que incluíram a impermeabilização do paramento de montante com uma geomembrana, a regeneração do betão, a construção de dois alinhamentos de escoras de betão ligando a base das almas dos contrafortes e a modernização e o reforço do sistema de observação.

Neste artigo apresentam-se os resultados da análise do comportamento observado desde o reenchimento da albufeira, em dezembro de 1992, que mostram o impacto das obras de reabilitação no comportamento da obra, nomeadamente a diminuição muito significativa da taxa de desenvolvimento das reações, embora de forma não uniforme em toda a estrutura.

Palavras-chave: Barragem de Pracana / Dano RSI-RAS / Reabilitação / / Monitorização / Avaliação estrutural.

José Piteira Gomes

National Laboratory for Civil Engineering (LNEC)
Lisbon, Portugal
pgomes@lnec.pt

Domingos Silva Matos

EDP Gestão da Produção de Energia S.A.
Porto, Portugal
domingossilva.matos@edp.com

António Lopes Batista

National Laboratory for Civil Engineering (LNEC)
Lisbon, Portugal
a.l.batista@lnec.pt

José Ilídio Ferreira

EDP Gestão da Produção de Energia S.A.
Porto, Portugal
ilidio.ferreira@edp.com

GOMES, J. [*et al*.] – Structural behavior of Pracana dam 30 years after rehabilitation due to severe ISR-ASR damage. **Revista Portuguesa de Engenharia de Estruturas**. Ed. LNEC. Série III. n.º 16. ISSN 2183-8488. (março 2021) 85-94.

1 Introduction

Pracana dam is a worldwide well-known case of a successful rehabilitation related with damage due to concrete swelling [1-4]. In fact, an abnormal behavior of the dam was observed since the first filling of its reservoir in 1951, characterized by progressive vertical and axial horizontal displacements (upstream-downstream direction) and extensive cracking, due to an intense ISR-ASR process, which led to empty the reservoir in 1980. The reservoir remained empty for 12 years. During this period several studies were developed, which culminated with the execution of large rehabilitation works of the dam, which take place from 1988 to 1992. This rehabilitation included the waterproofing of the upstream face by a geomembrane, the foundation and concrete dam body treatments by the grouting of cement and epoxy resins, the construction of two alignments of concrete struts to link the buttresses webs at the foundation level, one of them at the downstream toe, and the construction of a new spillway. An update of the monitoring system, including additional devices, was also implemented.

Since the refill of the reservoir in December 1992, the swelling rate declined, although not in an uniform way throughout the structure. It is therefore important to evaluate regularly the swelling evolution, as well as its possible recovery signs in different sections of the structure, and to reassess the structural safety conditions of the dam. In this context, the paper presents the most recent and relevant monitoring results and its statistical treatment, in order to assess the condition of the dam structural elements.

2 Pracana dam history

2.1 Dam's characteristics and history

The Pracana dam is a buttress structure, 60 m high (Figure 1), founded on a rock mass of phyllite and greywacke alternations. It was completed in 1951. Quartzite and granite aggregates were used in the concrete mix. An abnormal behavior was observed since the entry into service of the dam, characterized by progressive vertical and horizontal U-D displacements, and intense cracking. Physical and chemical tests were performed, on samples taken from the dam´s body, which confirmed the existence of ISR-ASR of moderate magnitude. At the end of the eighties of the last century the reservoir remained empty for a long period, to allow large scale rehabilitation works.

Figure 1 Downstream view of Pracana dam in 1992, after the rehabilitation works

The main events related to the dam are the followings:

1948/1951 – Construction of the scheme
Since 1952 – Several anomalies in the dam were detected, which have continuously increased
1971 – Restrictions to operation (limiting the reservoir level)
1972/1973 – Unsuccessful repair works
1977 – The scheme was owned by EDP
1978 – The reservoir was emptied due to insufficient capacity of the spillway and progressive deterioration of the dam's structure (fast decrease of the structural safety factor)
1985 – Conclusion of the rehabilitation studies
1988 – Beginning of the site works
1992 – Conclusion of the civil engineering works and refilling of the reservoir

The reservoir has been empty for 12 years (1980-1992).

2.2 Brief description of the dam's rehabilitation

The rehabilitation investigation and design was concluded in 1985. The site works started in 1988 and have consisted of dam structural rehabilitation and the execution of complementary works, namely the construction of an auxiliary frontal spillway and the updating of the powerhouse, including the construction, in the dam body, of the intake for the new generation unit.

The structural rehabilitation of the dam included the following works: i) general treatment of concrete, to its regeneration; ii) placement of an impermeable membrane on the upstream surface, including the construction of an upstream foundation plinth; ii) construction of two sets of concrete struts for locking the buttress webs at the foundation level, one next to the downstream toe and the other in an intermediate position; and iii) consolidation of the foundation and execution of new waterproofing and drainage curtains, being the last ones executed form the top of a plinth built along the dam upstream toe. The improvement of the monitoring system was also done.

The buttress concrete regeneration was made by: i) the treatment of cracks with an opening greater than 5 mm by injection of cement stabilized grout; and ii) the mass treatment by injection of epoxy resin. The execution and control of these treatments have been supported by direct ultrasonic tests.

The waterproofing system of the upstream surface consists of a non-adherent synthetic membrane in order to prevent the contact of the reservoir water with the concrete and, thus, stop the water supply to the ASR and simultaneously prevent the uplift developing in existent cracks of the buttresses heads (Figure 2). The system selected by EDP is a Carpi patented system consisting of an impervious flexible PVC geomembrane 2.5 mm thick, heat-coupled during extrusion to a non-woven, needle-punched 500 g/m^2 geotextile. The PVC geomembrane, which was applied over a HDPE geonet with drainage purpose, fulfil many requirements, namely: i) low permeability (k ≈ 10^{-12} cm/s); ii) high flexibility, that enables installation also on not smooth faces; iii) resistance to punching, tearing and impact; iv) resistance to high temperature gradients and to freeze-thaw cycles; v) resistance to stresses induced by large relative movements, such as movements induced by earthquakes; and vi) expected long durability.

During the dam rehabilitation the monitoring system was revised to conform with the Portuguese regulations for dam safety, which had been approved in the meantime [5], and also enhanced to better monitor the structural behavior and the swelling process evolution. So, the following instruments have been introduced (Figures 3 and 4): i) multiple rod extensometers installed along the heads of five buttresses (P1, P4, P6, P9 and P12); ii) two rod extensometers on each buttress foundation, one near the head and other at the downstream toe; iii) inverted plumb lines in fife buttresses (P1, P4, P6, P9 and P12), with suspension near the dam crest and anchored into the foundation rock; iv) thermometers located inside two buttresses (P5 and P7); and v) new jointmeters to measure the relative movements of joints. The geodetic monitoring system was also revised and improved.

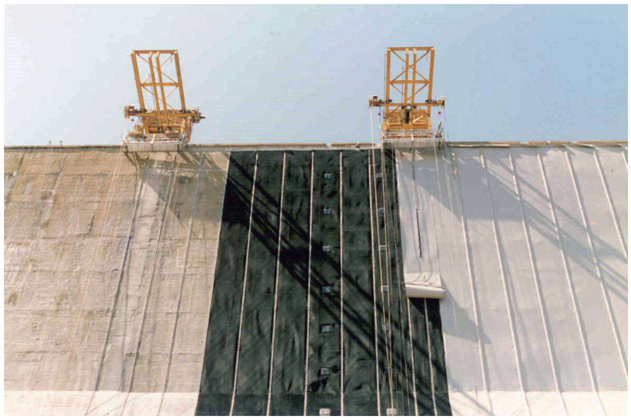

Figure 2 Stage of installation of the upstream impervious membrane

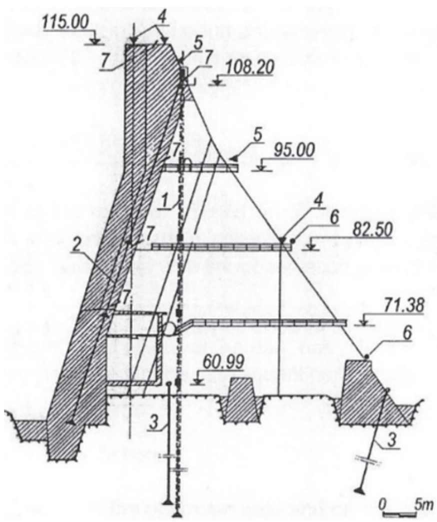

1 Inverted plumb-line
2 Multiple rod extensometer (dam's body)
3 Rod extensometer (foundation)
4 Levelling marks
5 Geodetic targets
6 Angles and distances measurements targets
7 Joint meters

Figure 3 General scheme of the new monitoring instruments installed in 1992 to measure displacements of the dam and its foundation

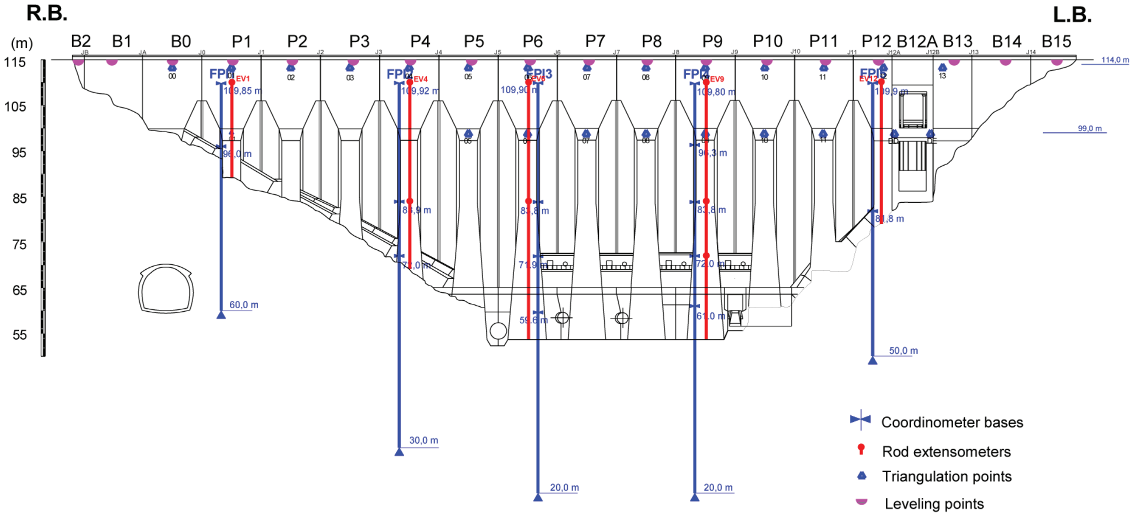

Figure 4 Monitoring instruments to measure horizontal and vertical displacements of the dam's buttresses

When the dam rehabilitation works were carried out, 63 thermometers were installed inside P5 buttress, at five different elevations, and another 63 thermometers were installed inside P7 buttress with equal distribution. These instruments, installed with the purpose of characterizing the structure's response to thermal action, began to be read in May 1986, about six and a half years before the beginning of the refilling of the reservoir and although many are no longer operational, mainly in the P5 buttress, so it is only possible to extract relevant information in the P7 buttress. Thus, the average temperature of the concrete in the P7 buttress, in the period in which the reservoir was empty, was 18.6 ºC, considering the 63 thermometers, and was 17.2 ºC since the refilling (December 1992) until March 2020, considering only the 47 thermometers that continuous operational. In the upper part of the buttresses' head, the differences reach more than 6 ºC.

3 Analysys and interpretation of the observed behavior

3.1 Statistical model adopted

The analysis and interpretation of the observed dam's behaviour was carried out using a statistical model of quantitative interpretation of the displacements measured over time by geodetic methods, rod extensometers and plumb lines. Quantitative interpretation consists of the analysis of a behavior mathematical model by which a functional relationship is established between the quantities or effects observed and the actions that originate them. The principle of superposition is assumed, considering that the actions corresponding to hydrostatic pressures and seasonal variations in temperature cause reversible effects and that the irreversible effects, due to non-elastic phenomena, depend only on time [6]. In the statistical model, a function of the type was adopted,

$$E_{calc}(h,t',t)=\sum_{i=1}^{N} a_i\, h^i + b_1\cos\frac{2\pi t'}{365} + b_2\sin\frac{2\pi t'}{365} + \sum_{j=1}^{M} c_j t^j + d\left(1-e^{-\frac{t_n}{\beta}}\right) + k \quad (1)$$

where E_{calc} represents the calculated response, h is the hydrostatic action usually represented by the upstream water level (when important the downstream level must also be considered), t' is the number of days since the beginning of the year and t is the number of days counted from the initial observation date. The parameters a_i, b_1, b_2, c_j, d and k are calculated by linear regression, performed by the least-squares method. N and M represent the degree of the polynomials used to represent the hydrostatic pressure and time effects, respectively, the terms in sine and cosine are intended to represent the effect of the annual thermal wave, it is considered a polynomial expression to reproduce the time effects and an exponential term is used to represent the effects of expansive action.

The differences between the values observed in the prototype and the values calculated by the statistical model are the residuals r, defined by the expression,

$$r = E_{obs}(h,t',t) - E_{cal}(h,t',t) \quad (2)$$

The coefficient of determination R^2 of a quantitative interpretation, which assesses the significance of the regression, is expressed by the equation,

$$R^2 = 1 - \frac{\sum_{i=1}^{n}\left(E_{cal}(h,t't) - E_{obs}(h,t',t)\right)^2}{\sum_{i=1}^{n}\left(E_{obs}(h,t't) - \overline{E}_{obs}(h,t',t)\right)^2} \quad (3)$$

where n is the number of observations and $\overline{E}_{obs}(h,t',t)$ is the average of the observed values. Closer the value of R^2 is to 1, more the model adjusts to the observed values.

3.2 Structural behavior interpretation during the first period of operation (1952-1980)

The first period of the dam's operation started in October 1951 (first filling of the reservoir) and finished in May 1980. In Figure 5 are represented the water level in the reservoir (a) and the air temperature (b) during this period. It can be seen that after the first

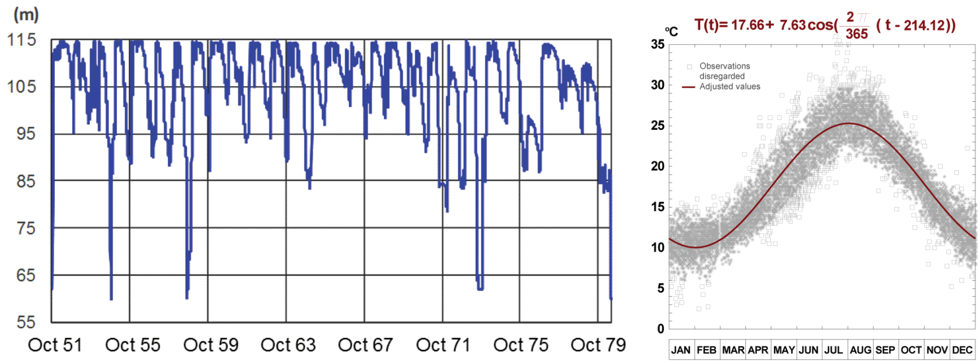

a) Water level in the reservoir b) Air temperature

Figure 5 Main actions in the period 1952-1980: a) water level in the reservoir and b) average daily air temperature observed and harmonic function adjusted

filling the reservoir has been emptied three times (October 1954, September 1958 and October 1973). The values of the average daily air temperature, observed between February 1953 and December 1978, allowed the computation of an annual period harmonic function. The thermal air wave is characterized by the average value of 17.7 ºC, the half-amplitude of 7.6 ºC and by a lag of 214.1 days in relation to the maximum annual value. In this period, the highest maximum and minimum lowest temperatures recorded were 39.0 C and 0.0 C, respectively.

During this period the monitoring system was based mainly on geodetic methods. The results of the monitoring campaigns allowed the detection of irreversible upward displacements and, also, downstream horizontal displacements, on the blocks B0 and B14 and on buttresses P2, P4, P6, P8, P10, P11 and P12. Just before the decision of stopping the operation and emptying the reservoir was taken, the quantitative interpretation results showed that the crest irreversible components of vertical and horizontal displacements, related to the time effect, were, very high, with average rates of 1.0 mm/year and 1.2 mm/year, respectively. Figure 6 shows the results of the statistical model application for vertical displacements measured on P8 buttress, since 1952 to 1980. A value of about 32 mm was computed to the irreversible vertical displacement due to the swelling process.

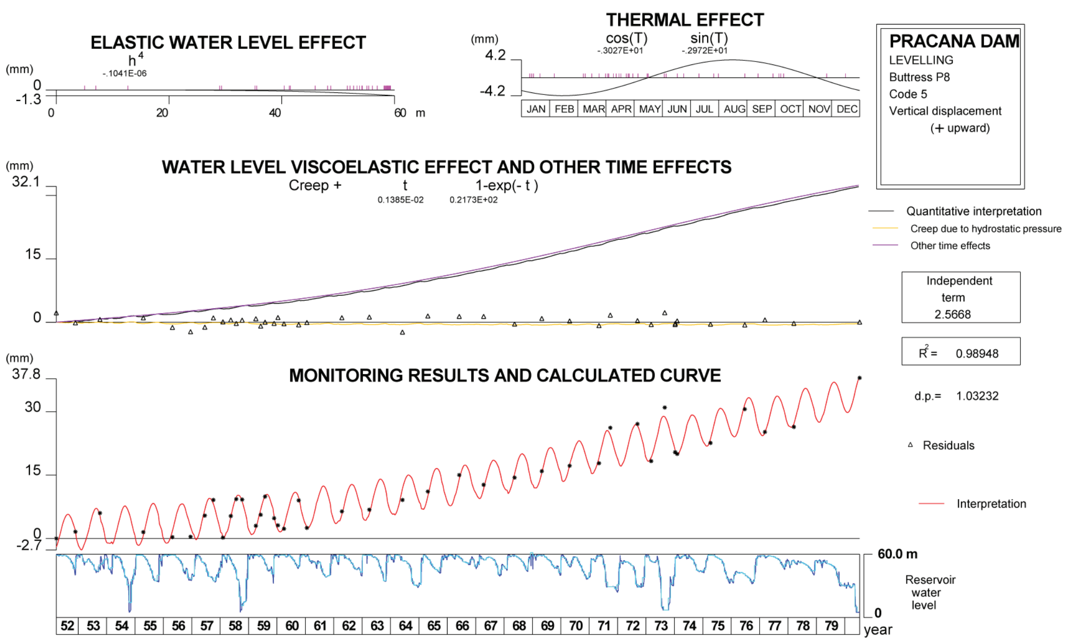

Figure 6 Results of statistical model application for vertical displacements measured on the top of P8 buttress since 1952 to 1980

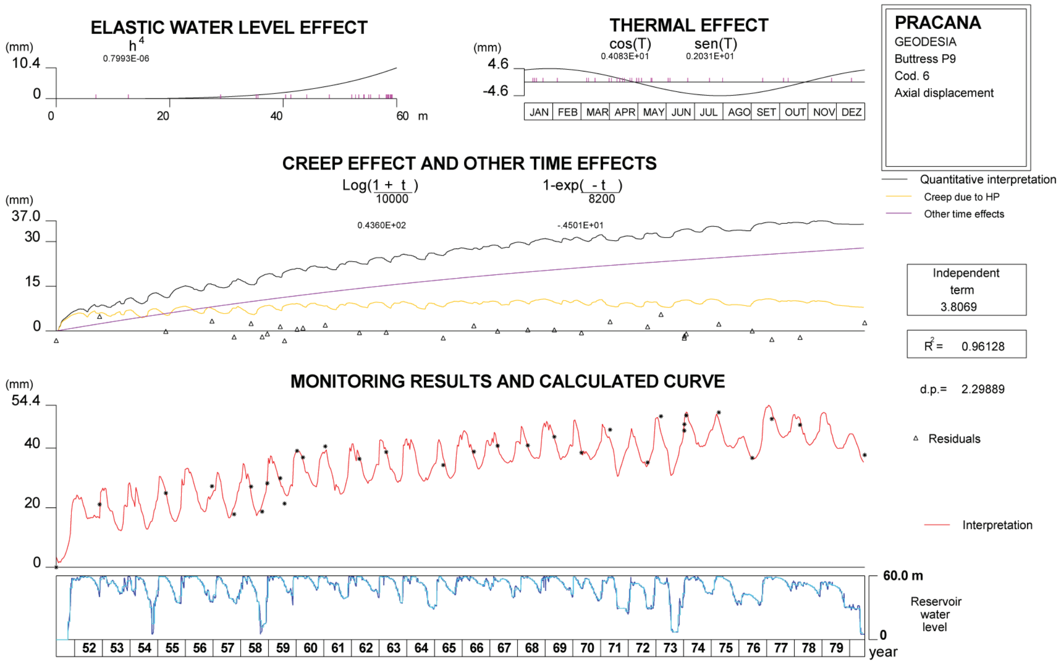

Figure 7 Results of statistical model application for horizontal (U-D) displacements measured on the top of P9 buttress since 1952 to 1980

In Figure 7 the results of statistical model application for horizontal upstream-downstream (U-D) displacements measured on the top of P9 buttress, since 1952 to 1980, are presented. Large irreversible displacements were computed in the downstream direction due to creep and swelling.

The magnitude of the computed vertical and horizontal displacements due to the swelling effects are compatible with the cracking patterns observed at that time.

3.3 Structural behavior interpretation during the operation period after the rehabilitation works (1992-2020)

The second period of dam's operation began in December 1992, after 12 years in which the reservoir has been empty. During these 12 years several studies were carried out, the dam rehabilitation project was developed, and all the rehabilitation works were executed.

In Figure 8a) the water reservoir level over time is presented. After the initial refilling, which occurred in December 1992, the reservoir was emptied in July 1994 and again refilled in September 1994. Since then the water level in the reservoir has varied, almost always, between elevation 95 m and the normal water level 114.0 m. Figure 8b) represents the values of the average daily air temperature, observed between December 1992 and January 2020, and the annual period harmonic function adjusted to the monitored data. The thermal air wave is characterized by the average value of 16.2 ºC, the half-amplitude of 7.6 ºC and by a lag of 207.1 days in relation to the maximum annual value. In this period, the highest maximum and the minimum lowest temperatures recorded were 45.0 C and – 5.0 C, respectively.

The application of the statistical model to the horizontal displacements measured on the upper coordinometer basis of the plumb lines, considering 970 records, shows that the axial components (upstream-downstream direction) due to water level variations and temperature changes are compatible with these actions, and reveals the occurrence of irreversible displacements towards upstream, reaching, at the end of this 28 years' period, the maximum of 4.6 mm at the top of buttress P9. Regarding the transversal displacements, measured in the same coordinometer basis, the quantitative interpretation model shows a very small component due to water level variations, a component due to temperature changes compatible with the thermal action, and reveals, in the plumb lines closer to the abutments, the occurrence of irreversible displacements, 2.3 mm towards the right bank at buttress P1 and 1.8 mm towards the left bank at buttress P12. In Table 1 the results of the quantitative interpretation model applied to horizontal displacements are presented.

The statistical analysis of vertical displacements for all points of the upstream and downstream precise levelling lines located at crest, which data was acquired in the 33 campaigns performed between December 1992 and January 2019, shows components due to water level variations and temperature changes compatible with these actions and reveals irreversible displacements upwards. These irreversible displacements are higher on the downstream line, with values, in the central zone of the dam, between buttresses P2 and P11, ranging from 4 mm and 8 mm and on the upstream line displacements ranging from 2 mm and 5 mm. It can also be seen

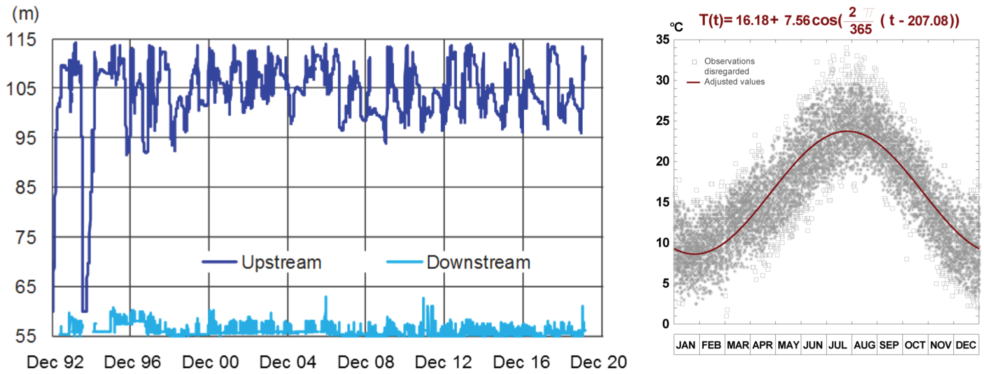

a) Water level in the reservoir

b) Air temperature

Figure 8 Main actions in the period 1992-2020: a) water level in the reservoir and b) average daily air temperature observed and harmonic function adjusted

Table 1 Main results of the quantitative interpretation model applied to horizontal displacements measured on plumb lines

	Axial displacements (mm)			Transversal displacements (mm)		
Buttress	Water effects	Temperature effects	Effects over time	Water effects	Temperature effects	Effects over time
P1	2,2	1,0	– 4,3	0,6	1,5	– 2,3
P4	4,9	3,3	– 4,1	0,3	0,8	– 0,9
P6	5,2	4,5	– 3,8	0,0	0,1	– 0,6
P9	5,0	4,8	– 4,6	– 0,1	0,8	1,1
P12	2,3	2,4	– 3,0	– 0,5	1,5	1,8

Axial displacements toward downstream are positive.
Transversal displacements toward left bank are positive.

that in the side blocks B1 and B0 on the right bank and B14 and B15 on the left bank the displacements are very significant. The corresponding calculated irreversible displacements correspond to vertical strain, accumulated during 27 years, that are small in the central zone of the dam, with average values below 100x10-6 and high deformations in the side blocks, mainly on the two blocks close to the left bank, as can be seen in Figure 9.

The application of the statistical model to the displacements measured by the simple and multiple rod extensometers installed in the heads of buttresses P1, P4, P6, P9 and P12, parallel to the

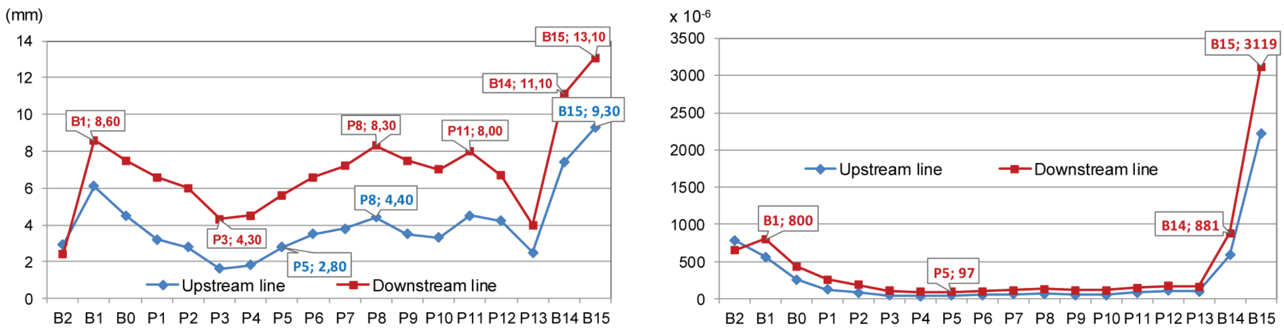

a)

b)

Figure 9 a) Irreversible vertical displacements on levelling marks at crest and b) accumulated vertical strains on the buttresses and side blocks

Table 2 Main results of the quantitative interpretation model applied to displacements measured on rod extensometers

Buttress	Rod extensometers				Levelling accumulated strains ($\times 10^{-6}$)
	Anchor elevation (m)	Rod length (m)	Accumulated displacements (mm)	Accumulated strains	
P1	84	27,4	5,6	204	127-263
P4	84	27,4	3,8	139	-
P4	64	48,5	4,5	93	38-95
P6	84	27,4	5,5	201	-
P6	54	59,0	5,3	90	56-105
P9	84	27,4	5,8	212	-
P9	72	39,5	4,9	124	-
P9	54	59,0	7,0	119	56-120
P12	79	32,6	6,2	190	109-174

The shading cells corresponds to rod extensometer showing malfunction.

upstream face and about 4 m from that surface, with the heads of the instruments on the downstream surface of the buttresses at 110 m elevation and anchors near the foundation, show results compatible with those obtained by levelling. During this period 957 campaigns were carried out. Table 2 shows results related to the irreversible components of the displacements and respective strains, where the last column shows results obtained from levelling analysis.

The quantitative interpretation model has revealed progressive displacements for all the observed rods, showing that the swelling process has continued with upwards crest movements, registering however a small attenuation. For longer rod extensometers the time effect results are compatible to those obtained by levelling. It can also be observed that the shorter rod extensometers have higher accumulated strains.

3.4 Swelling developed before and after the dam rehabilitation

In Table 3, the results of quantitative interpretation of vertical displacements, obtained from the crest levelling before and after the dam rehabilitation, are compared. These two periods have similar duration and the results clearly show that the accumulated swelling and the expansion average annual rates are significantly lower in the second period, with exception of block B1. In all buttresses with monitored results in both periods there were reductions between 5 and 8 times and in block B14, on the left bank, there was a reduction of 2.5 times. However, in block B1, on the right bank, there was an increase of about 40% in the annual swelling rate.

Block B15, on the left bank, is the one with the greatest irreversible deformations (it was not monitored in the first period of the dam's life).

3.5 Waterproofing geomembrane behavior

The drainage system, installed between the waterproofing system and the upstream concrete face of the dam, is divided into eight main independent compartments, as shown in Figure 10. The water collected in each compartment is conducted to drains located at the upstream face, immediately above the plinth surface, which are equipped with downstream outlets to enable the measurement of the respective discharges.

Figure 11 shows the discharges evolution in the different geomembrane drainage compartments. As can be seen, in the compartments 1 and 4, where several membrane ruptures have occurred, the discharges were higher. In compartment 1, where the most significant ruptures occurred in 2011, 2018 and very recently (December 2019), the discharges have reached maximum values of about 75 l/min. The discharges from compartment 4 had a first increase between 2000 and 2003, with maximum values of about 65 l/min, but since 2011 to 2016 the increase was higher, reaching a maximum value of 209 l/min in April 2016. In November 2016 there was a geomembrane repair intervention that drastically

Table 3 Average swelling accumulated and average annual rates, during the first and second periods, obtained through the analysis of the crest vertical displacements (levelling)

Buttress	Height (m)	First period (October 1952 to May 1980)			Second period (December 1992 to January 2019)		
		Accumulated vertical displacements (mm)	Accumulated vertical strain ($\times 10^{-6}$)	Annual swelling rate ($\times 10^{-6}$)	Accumulated vertical displacements (mm)	Accumulated vertical strain ($\times 10^{-6}$)	Annual swelling rate ($\times 10^{-6}$)
B2	3.7	–	–	–	2.7	716	27.4
B1	10.8	5.6	521	18.4	7.4	684	26.2
B0	17.2	–	–	–	6.0	349	13.4
P1	25.1	–	–	–	4.9	195	7.5
P2	32.1	33.1	1050	37.1	4.4	137	5.3
P3	38.6	–	–	–	3.0	76	2.9
P4	47.3	29.0	607	21.5	3.2	67	2.6
P5	57.8	–	–	–	4.2	73	2.8
P6	63.0	31.8	550	19.4	5.1	80	3.1
P7	62.3	–	–	–	5.5	88	3.4
P8	62.3	32.1	535	18.9	6.4	102	3.9
P9	62.3	–	–	–	5.5	88	3.4
P10	60.9	26.8	466	16.5	5.2	85	3.2
P11	53.4	33.1	685	24.2	6.3	117	4.5
P12	38.4	30.6	836	29.5	5.5	142	5.4
B13	24.2	–	–	–	3.3	134	5.1
B14	12.6	25.5	2024	71.5	9.3	734	28.1
B15	4.2	–	–	–	11.2	2667	102.2

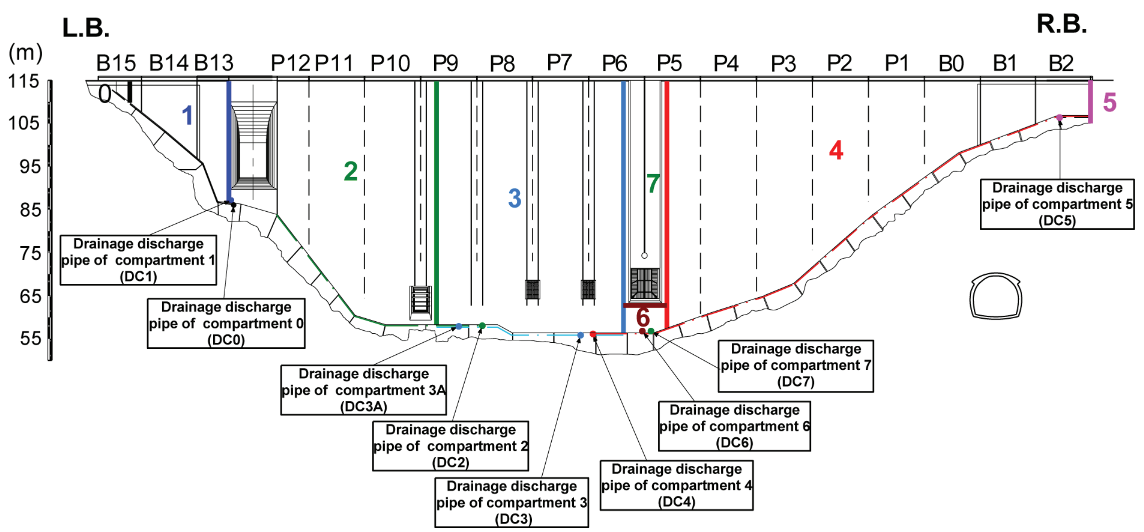

Figure 10 Drainage system of geomembrane from the eight independent compartments, with location of the drainage discharge pipes of each compartment

reduced those discharges. However, in 2019 new rips appear to have occurred.

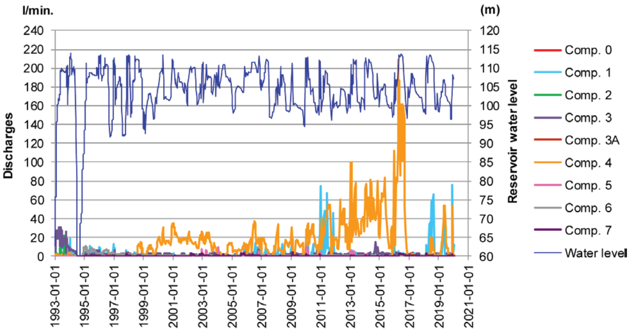

Figure 11 Discharges evolution in the different geomembrane compartments

It should be noted that the measured values of the water level in the compartments have been systematically zero, which indicates there is no accumulated water between the geomembrane and the upstream surface of the dam, and that the compartment drains have an appropriate discharge capacity. Nevertheless, preventive actions must be taken to remove the solid material that floats in the reservoir, particularly in flooding periods, to avoid its impact on the geomembrane, which has been the cause of the rips that have occurred.

4 Conclusion

The monitoring system installed in Pracana dam indicates progressive upstream horizontal displacements and vertical upwards crest displacements. Interpretation of levelling, plumb lines and rod extensometers displacements by statistical models has shown that the swelling process, although still present, has a significant lower rate in relation to the first period of dam's operation, before the execution of the rehabilitation works.

In the first period of operation, the average vertical accumulated strain in the central seven monitored buttresses was 680×10^{-6}, corresponding to an annual swelling rate of 24×10^{-6}/year. In the second period of dam's operation the average vertical accumulated strain in the central twelve monitored buttresses was 105×10^{-6}, with an annual swelling rate of 4×10^{-6}/year. A swelling rate significant reduction of about six times was achieved with the rehabilitation works.

The results for the side blocks B2, B1 and B0, located on the right bank, are similar in the two periods of dam's operation. In the first period the vertical accumulated strain of block B1 was 520×10^{-6}, with an annual swelling rate of 18×10^{-6}/year, and in the second period the corresponding values for the three blocks were 580×10^{-6} and 22×10^{-6}/year, respectively. However, this last value is five times higher than the correspondent value computed for the central zone.

Regarding the left bank, the comparison is made considering only the block B14 because it is the only one that was monitored in both periods and also because the results obtained in the three blocks B13, B14 and B15 are very different. Thus, in the first period vertical accumulated strain of block B14 was 2020×10^{-6}, with an annual swelling rate of 72×10^{-6}/year, and in the second period the average vertical accumulated strain in the same block was 730×10^{-6}, with an annual swelling rate of 28×10^{-6}/year. However, vertical accumulated strain of block B15 during the second period was 2670×10^{-6}, with an annual swelling rate of 100×10^{-6}/year. This value is about 25 times higher than the expansions in the central zone, which require further investigation and, if necessary, a medium-term intervention.

Mitigation of the swelling process proportionate by the rehabilitation works is undoubtedly a positive result to which the geomembrane installation on the upstream surface has given an important contribution. However, the long period with the reservoir emptied and the dam weather conditions, relatively warm and dry, may have also contributed to reduce the speed of the swelling process. In view of the results obtained, it is considered that the geomembrane continues to exhibit a good performance and functionality, preventing the upstream water access to the dam body. After 28 years of natural exposure, the evaluation of its physical condition must be checked frequently, which is done by carrying out visual inspections, in order to detect rips usually caused by floating woody material, especially after the occurrence of important floods. These rips are usually repaired in the following dry season.

Finally, it must be recognized that the rehabilitation of the Pracana dam is a successful case, because since that time it has been operating without limitations. However, in addition to the implemented observation plan, which includes the analysis of the monitoring data and of the visual inspections, it is advisable to perform laboratorial tests for assessing the current situation of the swelling process and to predict its evolution, in order to ensure the safety of the dam.

References

[1] Silva Matos, D.; Silva, H.; Pinho, J.; Camelo, A. (1995) – Deterioration of Pracana dam due to ASR. Main features and repair works. 2nd International Conference on Alkali Aggregate Reactions in Hydroelectric Plants and Dams, Chattanooga, Tennessee, USA, October 1995, pp 311-321.

[2] Work Group of the Portuguese National Commission on Large Dams (2003) – Ageing Process and Rehabilitation of Pracana Dam. ICOLD XXI Congress, Q. 82, R 8, Montreal, Canada, June 2003, 18 p.

[3] Work Group of the Portuguese National Commission on Large Dams (2003) – Observed Behavior and Deterioration Assessment of Pracana Dam. ICOLD XXI Congress, Q. 82, R 8, Montreal, Canada, June 2003, 21 p.

[4] Silva Matos, D.; Ferreira, I.; Camelo, A.; Piteira Gomes, J.; Scuero, A.; Vaschetti, G.; Vale, J.M. (2013) – Pracana dam 20 years after rehabilitation – Observed behaviour of the dam and its exposed geomembrane. 81st ICOLD Annual Meeting. International Symposium, Seattle, Washington, USA, August 2013, 10 p.

[5] RSB (1991) – Portuguese Regulation for Safety of Dams. Lisbon.

[6] Batista, A.L.; Mora Ramos, J.; Oliveira, S.B.; Piteira Gomes, J. (2002) – Models for safety control of concrete dams. 3th International Conference on Dam Engineering, Singapore, March 2002, 8 p

Reinforcement and replacement interventions in some bridges located on Aguieira dam road network

Intervenções de reforço e substituição das pontes inseridas na rede rodoviária da barragem da Aguieira

Tiago Rodrigues
Ana Rita Pereira
André Martinez Costa

Abstract

After an underwater inspections campaign, carried out by IP, S.A. on Aguieira dam road network, it was detected the existence of generalized deteriorations related with the effects of swelling reactions in the concrete, mainly on the submerged elements of 7 bridges.

These bridges, designed by Prof. Edgar Cardoso and built on the 70´s, have prestressed concrete girder decks, with total length between 180 m and 340 m, with longitudinal and transverse prestress beams. All bridges have piers founded on the rock mass foundations under the dam reservoir.

In order to define the reinforcement solution to be performed in each of the bridges, IP, S.A. promoted their structural assessment and monitoring, culminating in the replacement of one bridge and the structural reinforcement of the others.

This paper intends to describe the interventions carried out in these structures, considering the challenge of intervening in deep infrastructures in a dam reservoir, with no traffic restrictions.

Resumo

Na sequência de uma campanha de inspeções subaquáticas promovida pela IP, S.A nas obras de arte inseridas na albufeira da barragem da Aguieira, constatou-se a existência de anomalias generalizadas, principalmente nos elementos submersos de 7 pontes, associadas a reações expansivas no betão.

As pontes, projetadas pelo Prof. Edgar Cardoso e construídas nos anos 70, são em betão armado, com comprimentos totais entre 180 e 340m, com pré-esforço longitudinal e transversal nos tabuleiros. Todas as pontes são fundadas na albufeira da barragem.

No sentido de definir as soluções de reforço em cada uma das pontes, a IP, S.A promoveu a realização dos projetos de intervenção e a monitorização estrutural das obras, culminando no reforço de 6 pontes e na substituição da Ponte Foz Dão.

Este artigo pretende descrever as várias intervenções realizadas nas estruturas, considerando o desafio de intervir em elementos localizados dentro da albufeira, sem restrições de tráfego.

Keywords: Aguieira bridges / Swelling reactions of concrete / Rehabilitation / / Reinforcement

Palavras-chave: Pontes da Aguieira / Reações expansivas / Reabilitação / Reforço

Tiago Rodrigues

Diretor Departamento de Estruturas Especiais
Direção de Engenharia e Ambiente, Infraestruturas de Portugal
Almada, Portugal
tiago.rodrigues@infraestruturasdeportugal.pt

Ana Rita Pereira

Departamento de Estruturas Especiais
Direção de Engenharia e Ambiente
Almada, Portugal
ana.spereira@infraestruturasdeportugal.pt

André Martinez Costa

Departamento de Estruturas Especiais
Direção de Engenharia e Ambiente
Almada, Portugal
andre.costa@infraestruturasdeportugal.pt

RODRIGUES, T. [*et al.*] – Reinforcement and replacement interventions in some bridges located on Aguieira dam road network. **Revista Portuguesa de Engenharia de Estruturas**. Ed. LNEC. Série III. n.º 15. ISSN 2183-8488. (março 2020) 95-106.

1 Introduction

The Aguieira dam road network, located in the center of Portugal, was built in the late 1970s, and includes several bridges located in its reservoir.

Within the preparation of a project for the rehabilitation of those bridges, an inspection and testing campaign was carried out, where a set of serious deteriorations were identified in the bridge piers, caused by swelling reactions in the concrete.

According to this situation, Infraestruturas de Portugal, S.A. (National Authority for Road and Rail Infrastructure) decided to define a phased interventions plan, as follows:

- 1st phase – Deck and abutments rehabilitation and structural reinforcement, in order to repair existing anomalies and the structural deteriorations;
- 2nd phase – Piers and foundations rehabilitation and structural reinforcement, since the deteriorations detected, caused by the concrete swelling reactions, required a convenient evaluation of residual expansion, in order to correctly define the scope of the intervention.

Therefore, with the collaboration of the LNEC (National Laboratory for Civil Engineering), it was decided to implement monitoring systems on the bridge piers and to perform a set of complementary tests, in order to evaluate the concrete residual expansion and to evaluate the structural safety conditions.

This paper intends to summarise the various stages of a complex process that culminated with the replacement of Foz do Dão Bridge, and with the rehabilitation works of the remaining bridges.

Thus, it will be described the deterioration found on the bridge piers during the several inspections that were carried out and from the concrete laboratory tests results. It will also be briefly described the structural monitoring system and the dynamic tests performed, in order to guarantee the structural and the users safety, while the bridges were not intervened.

The assumptions and conditionings considered in the rehabilitation, structural reinforcement and replacement projects will also be addressed, as well as described the implemented solutions.

2 Bridges general description

The bridges are located in the reservoirs of Aguieira and Raiva dam, in the following roads:

- IP3, between Cunhedo and Santa Comba Dão, in Viseu district:
  - Cunhedo Bridge over Mondego River
  - Mortágua Bridge over Mortágua River
  - Foz do Dão Bridge over Dão River
  - Santa Comba Dão Bridge over Dão River
- EN234, between Mortágua and Santa Comba Dão, in Viseu district:
  - Criz I Bridge over Breda River;
  - Criz II Bridge over Criz River
- EN234-6, between Vimieiro and Tábua, in Coimbra district:
  - São João de Areias Bridge over Mondego River

Figure 1 Lower view of Cunhedo Bridge [1]

Figure 2 General view of Mortágua Bridge [1]

Figure 3 General view of Foz do Dão Bridge [2]

Figure 4 General view of Santa Comba Dão Bridge [3]

Figure 5 General view of Criz I Bridge [4]

Figure 6 General view of Criz II Bridge [4]

Figure 7 Lower view of São João de Areias Bridge [5]

These girder bridges, made of reinforced concrete, with longitudinal and transverse prestressing, were designed in 1975 by Prof. Edgar Cardoso, and were built between 1976 and 1979.

The bridges have multiple spans, with 30 m length end spans and 40 m length middle spans. The decks are 15,20 m wide, with 4 longitudinal girders with variable height, from 2,00 m up to 2,50 m, and cross girders on the first 2/3 of the span, and above the piers and abutments.

The piers have solid cylindrical shape or hollow diamond shape cross-section, with hammer head in the top, which support the deck through structural bearings.

The abutments are U-abutments type, composed by front walls and wing walls, of the harmonium type, provided by counterforts and supported on footings.

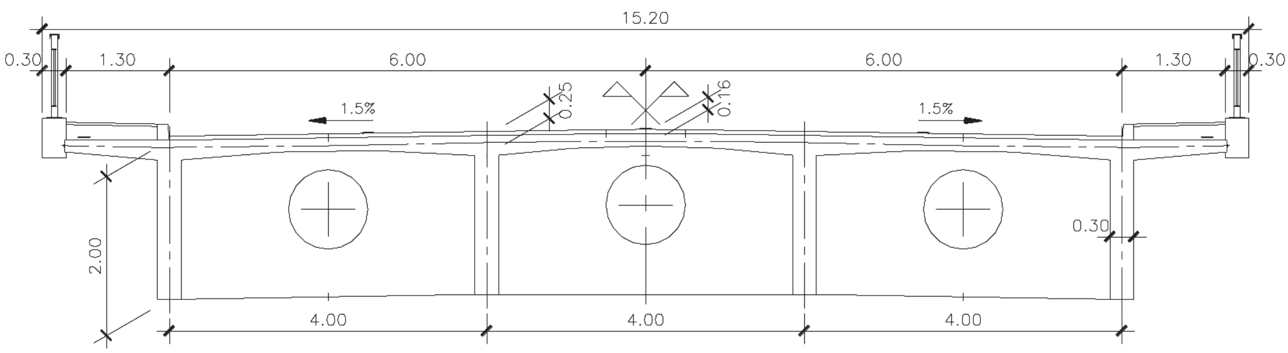

Figure 8 Deck cross section [1]

Table 1 Number of spans, total length and highest pier of each bridge

Bridge	Cunhedo	Mortágua	Foz do Dão	Santa Comba Dão	Criz I	Criz II	São João de Areias
Number of spans	9	5	9	5	5	8	7
Total length [m]	340	180	340	180	180	300	260
Highest pier [m]	25	29	85	31	39	69	51

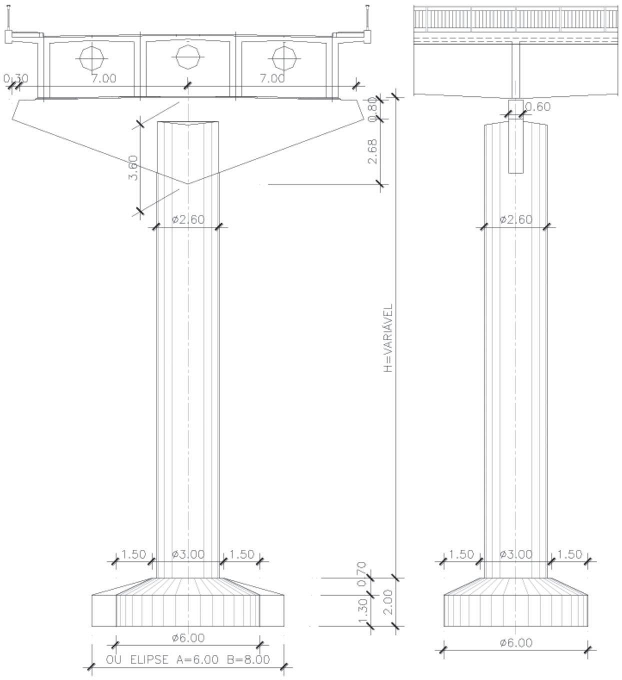

Figure 9 Cunhedo, Mortágua and Santa Comba Dão Bridge piers [1]

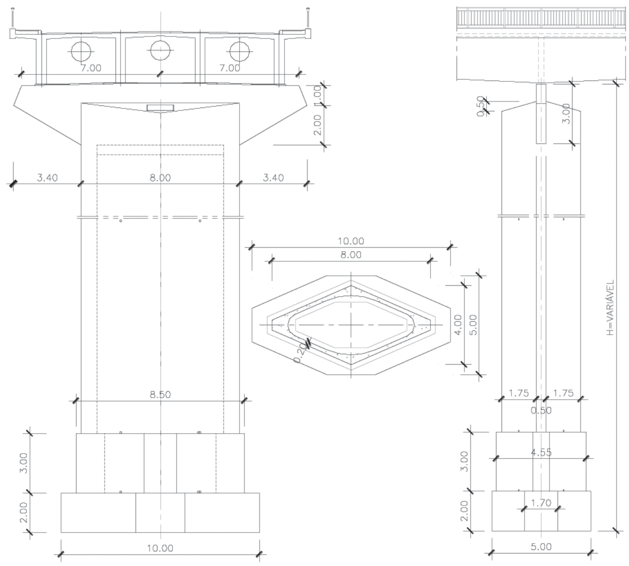

Figure 10 Foz do Dão, Criz I, Criz II and São João de Areias Bridge piers [1]

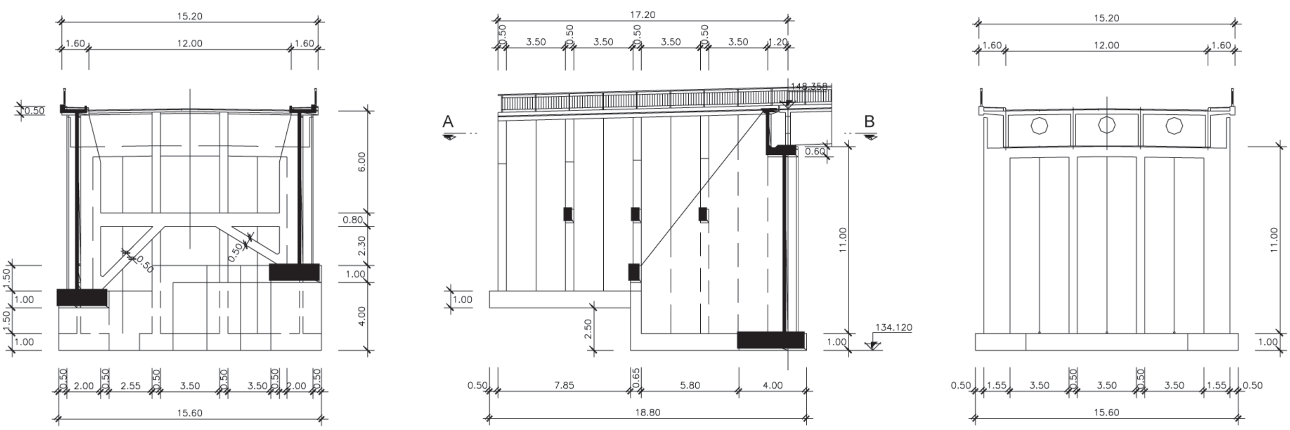

a) b) c)

Figure 11 Abutments vertical cross section a), longitudinal section b) and frontal elevation c) [1]

3 Detected deteriorations

3.1 Underwater inspections

Through the underwater inspections carried out on the bridges, a set of several deteriorations were observed, as follows:

- Several cracks in piers foundation, particularly at the basement level, with random orientation, typical of swelling reactions;
- Vertical cracking, mainly in the pier/basement connection, over all the piers perimeter, with uniform spacing;
- Vertical cracking in the piers shaft, with some spot zones with steel corrosion and deficient concrete joints.

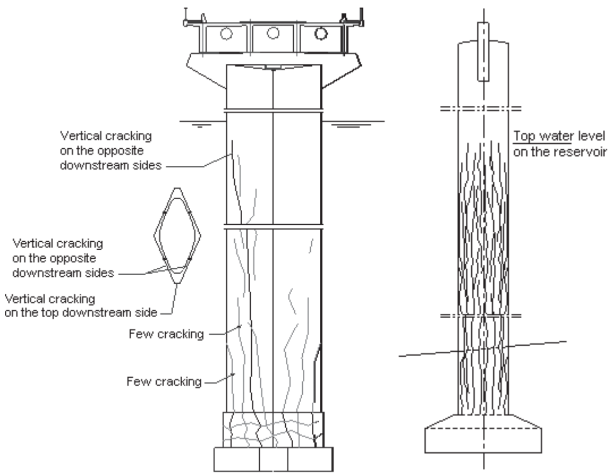

Figure 12 Cracking observed on Foz Dão Bridge piers [1]

3.2 Tests

To better understand the damage process that occurs on the bridges and the potential evolution of the deteriorations that were found, a set of laboratory and "in situ" measurements and tests were carried out, which allowed IP, S.A to promote some corrective measures and define structural rehabilitation and reinforcement strategies.

3.2.1 Assessment of concrete degradation

To characterize the concrete condition, some laboratory tests were carried out on the structural elements of the bridges, in order to assess the causes of concrete deterioration and to evaluate the potential of evolution in a near future, namely:

- Mineralogical analysis by X-ray diffractometry;
- Petrographic characterization;
- Determination of soluble alkalis content;
- Determination of cement content;
- Determination of sulfate content;
- Potential residual expansion due to ASR;
- Potential residual expansion due to DEF;
- Microstructural analysis by SEM (electronic scanning microscopy);
- Evaluation of compressive strength;
- Evaluation of the elasticity modulus;
- Determination of stiffness degradation.

The results of the studies developed by LNEC on these bridges have concluded the presence of internal swelling reactions, namely alkali-silica reaction (ASR) and internal sulphate reaction (DEF). These reactions were manifested through the cracking and deterioration of the superficial layer of the concrete, with more expression in the structural elements in contact with permanent water or water-flow.

The cracking that occurred in some sections of the pier shafts immersed on the reservoir, was predominantly oriented along the vertical direction. This situation was related to the confinement effect in this direction provided by the axial compression to which they are subjected. The development of cracking was in all submerged pier height, sometimes increasing their expression in depth.

The cracking process was more expressive in the pier basements and particularly in areas where tensile stresses or low compressive stresses occur for structural reasons.

According to the LNEC results, the swelling process that occurred was classified as moderate to high, regarding the remaining potential of alkalis (P6 pier of the Criz II Bridge), and low, regarding the internal sulfates, which conducted into a reduction of the concrete elasticity modulus (with greater relevance in P6 pier of Criz II Bridge, P2 and P3 piers on Foz Dão Bridge, P1 and P3 piers on Santa Comba Dão Bridge), being therefore expected the concrete deterioration to worsen over time.

The results of the tests performed by LNEC showed that the deterioration mechanism, due to swelling reactions, led to a significant change in the concrete mechanical properties, particularly the elasticity modulus, which conducted to the structural rehabilitation and reinforcement of 6 bridges and the replacement of Foz do Dão Bridge.

3.2.2 Precision levelling

Several precision levelling surveys were carried out on the bridges deck, with the main objective of detecting possible vertical displacements in the piers, as consequence of the pathologies that were found. The survey results were satisfactory.

3.2.3 Dynamic characterization tests

Dynamic tests were carried out periodically in some bridges in order to identify changes in the dynamic characteristics of the structure, namely the natural frequencies and damping coefficients of their main vibration modes. Since the dynamic characteristics depend on the stiffness and bridge mass, any change in these parameters could indicate an evolution of the structural damage.

The results of these tests allowed to complement the assessment of the structural conditions of the bridges, leading to the implementation of traffic constraints (vehicle weight and speed) in Criz I, Criz II, Foz do Dão and São João de Areias Bridges.

3.3 Structural monitoring

As a complement to visual and underwater inspections that were carried out periodically, a set of monitoring campaigns was also implemented, which allowed assessing the structural behaviour of bridges in the period between the project development and the rehabilitation works.

3.3.1 Before rehabilitation works

For the Criz I and II, Foz do Dão and S. João de Areias Bridges, a structural health monitoring system was implemented, which consisted in the installation of the following equipment:

- Inclinometers, for measuring rotations at the top of the piers;
- LVDT transducers, to measure the movements of the expansion joints;
- Thermometers, to measure the temperature of the deck, bridge piers and air.

This system was operating until the end of rehabilitation works in the structures and the replacement of the Foz do Dão Bridge.

3.3.2 Post-rehabilitation works

During the piers and foundations rehabilitation works on Criz II and S. João de Areias Bridges, it was installed a monitoring system to evaluate its structural integrity, which allows to collect information related to the performance and durability of the rehabilitation and reinforcement systems that were implemented.

The concrete deterioration that resulted from the development of swelling reactions will origin a loss of stiffness in the structures that, according to the structural system that was designed and implemented, will result in a load transfer to the reinforced structural elements.

The structural health monitoring system installed by LNEC [6] comprises the following equipment:

- Extensometers, to measure strains inside the foundations concrete, particularly in the reinforcement elements (piles), as well as on the piers shafts concrete surface, in the lower section of the pile cap;
- Strain-gauges, to measure strains in the jacketing, in the higher section of the pile cap, in order to detect the eventual contribution of this concrete to support the loads;
- Moisture sensors, to measure the original piers shaft permeability, in order to monitoring the possible water access to the original concrete, now covered by the jacketing, finishing mortar and coating applied in the intervention;
- Moisture sensors, inside the piers jacketing concrete, in order to monitoring the evolution of the water conductive conditions to develop rebar corrosion;
- Thermometers, to measure the concrete temperature, inside and on the surfaces.

4 Interventions

4.1 First phase: deck and abutments

The first structural reinforcement and rehabilitation works were carried out on the decks and abutments of all bridges, apart from Foz do Dão Bridge, in order to repair the anomalies and to suppress the structural deteriorations.

4.1.1 Main anomalies

The most common anomalies detected on the decks and abutments were generically of the following types:

- Excessive deflection of the deck, easily observable, with values greater than 5 cm;
- Areas with concrete poorly vibrated or with poor connection between different age concrete at construction joints, with honeycombs;
- Vertical cracks on the longitudinal girders, associated with bending, resulting from the reduced compression introduced by the applied prestress;
- Some transversal cracks on the deck slabs, next to the transversal girders located above the piers;
- Concrete degradation, such as delamination and rebar corrosion, associated to carbonatation effects;
- Crushed or damaged lead bearings;
- Cracks on the transversal girders located above the piers, next to the external longitudinal girders;
- Cracks on the abutments, due to the swelling reactions, and structural defects.

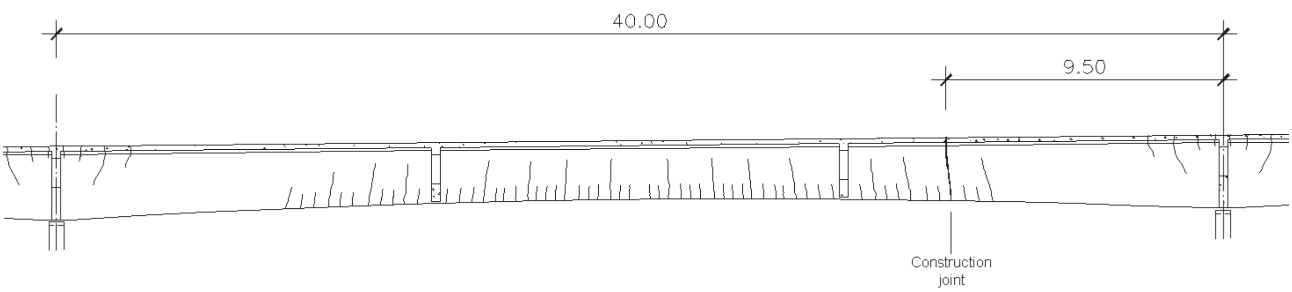

Figure 13 Cracks distribution on the girders [1]

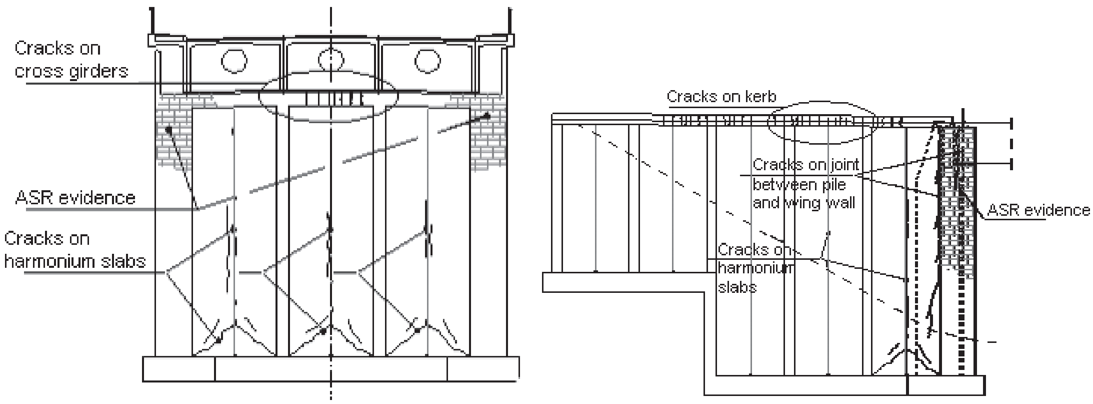

Figure 14 Anomalies detected on the front walls and wing walls of abutments [1]

4.1.2 Structural evaluation

From the limit state verification for the current regulations, resulted de following main conclusions:

- Non-verification of the serviceability limit state (SLS) (deflection and cracking) on the decks and piers shaft, and safety factors for the ultimate limit state (ULS) lower than the prescribed on the regulations;
- Insufficient shear rebar;
- Lack of resistance in some of the piers when subjected to the seismic action.

4.1.3 General description of rehabilitation and reinforcement works

Considering the poor performance of the existing prestress, the deck was reinforced through external prestressing in the four longitudinal girders of the deck. This measure improved the service behaviour of these elements, resulting in an important increase in their performance.

In addition to this measure, the following interventions were also implemented, to reinforce the deck and abutments:

- Abutments reinforcement, through the placing of a slab on the wing walls and counterforts of the existing wing walls and on an alignment of piles built along the road axis;
- Removal of the abutments interior fill until the ground level, in order to reduce the soil pressure;
- Reinforcement of the abutment bearing beams, piers and abutments transversal girders, through jacketing with new elements of reinforced concrete and prestressing application;
- Piers cap beam reinforcement through the adoption of prestressing and jacketing, in order to allow the load transfer from the bearings to the piers;
- Concrete rehabilitation and cracks injection, including coating;
- Expansion joints replacement;
- Structural bearings replacement;
- Drainage systems repair and relocation.

4.2 Second phase: bridge piers and foundations

The second phase corresponded to the rehabilitation and reinforcement works on the piers and foundations, which were carried out in order to repair and correct the deteriorations, after assessing the concrete degradation and residual swelling.

4.2.1 Conditionings

The proposed solutions were conditioned by a set of several aspects that required a sophisticated, highly conceptual and technical reinforcement solutions, as follows:

- Bridges location in the Aguieira dam reservoir, with a level variation around 10 m. The piers shaft have a variable immersed length, about 20 to 30 m, and more than 60 m in the maximum zone;
- Several difficulties on access to the piers shaft and footings;
- The repair process of the piers shaft was not enough to solve the existing deterioration, since the swelling reactions that were observed would be expected on spread footings;
- Proximity of the existing foundation elements (footings and piers basement) to the reinforcement elements;
- Repair works had to be carried out without road traffic interdiction;
- In the case of the Foz Dão Bridge, there are very steep slopes, forming a "V" shape.

4.2.2 General description of rehabilitation and reinforcement works

4.2.2.1 Cunhedo, Mortágua and Santa Comba Dão Bridges

The rehabilitation solution designed for these bridges consisted on the execution of a single shaft, on each pier, keeping the existing cap beam. The shaft cross-section geometry is a ring, which involves the existing one, founded with micro piles. The new shaft walls have a thickness of 0,30 m and an outer diameter of 3,40 m, ensuring a

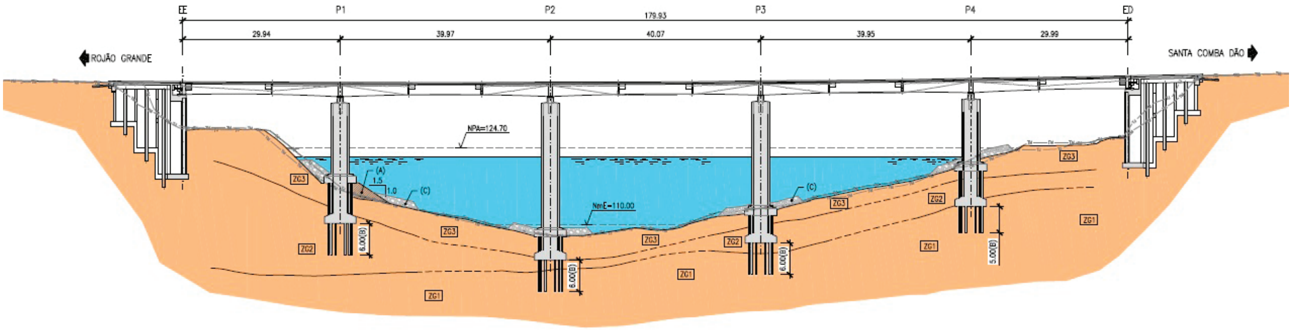

Figure 15 Intervention solution in the foundations of Santa Comba Dão Bridge [3]

clearance of 0,10 m throughout the perimeter of the existing piers, in order to allow its expansion without restrictions, due to the swelling reactions that will continue to take place.

The foundation consists in a set of twelve micro piles with high load capacity, headed by a circle pile cap with an outer diameter of 6,20 m, built, as the shaft, around the existing pier. The micro piles were built from the surface, intersecting the existing footings. At the top (cap beam), the new shaft is connected to the existing one through bolts, throughout the perimeter of the shaft and at a height of about 2,0 m.

It was generally preserved the structural equipment as bearings, expansion joints and oil-dynamic devices, installed during the deck rehabilitation and reinforcement, except in the P7 pier of the Cunhedo Bridge, where it was necessary to change the bearings, from the fixed type to the longitudinal free guided type.

4.2.2.2 Criz I and Criz II Bridges

Structural solutions

The structural solution designed for these bridges consisted of the deactivation of existing foundations and shaft pier sections that are immersed in the reservoir, through the execution of a set of several piles with ϕ1,50 m, headed by a prestressed pile cap in reinforced concrete, transferring the load from the shafts to the new foundation.

The main difficulty of these solutions was related to the execution of the piles and their caps with the use of aquatic and underwater resources, in order to ensure the perfect embedding on the bed rock. To minimize the identified difficulties, during the construction phase a system to guide and fix pile tubes was performed near the bottom, around the shaft and pier basement which also served as pier base confinement.

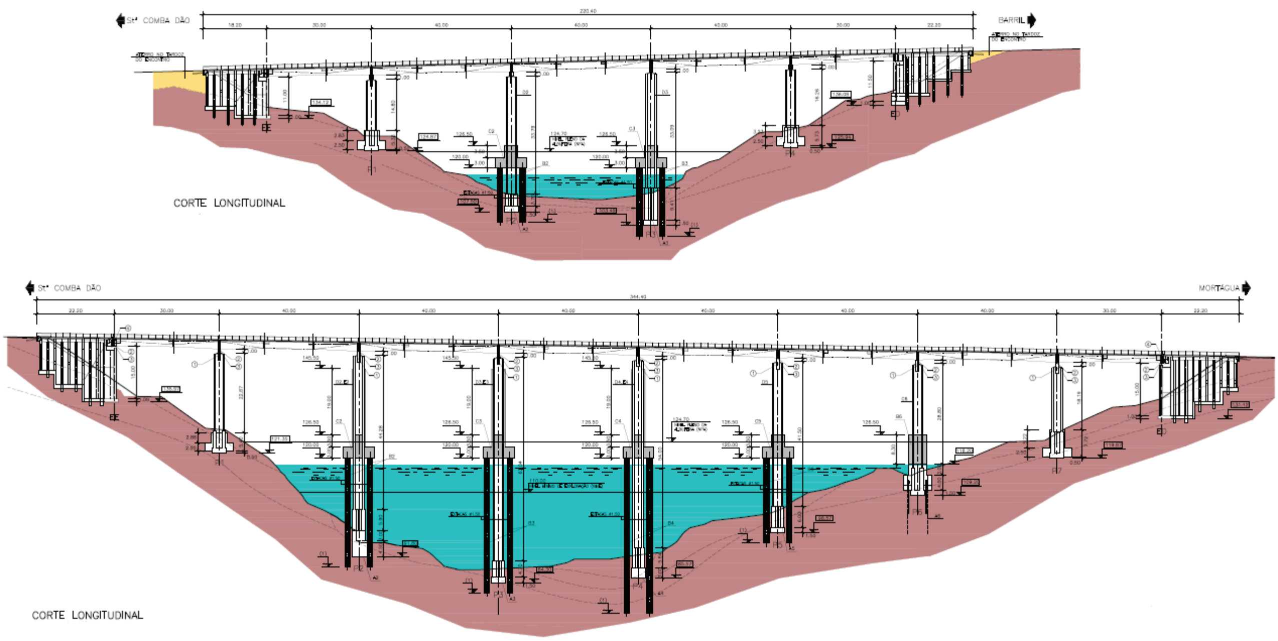

Figure 16 Intervention solution in the foundations of Criz I and Criz II Bridges [4]

Additionally, in P2, P3 and P4 piers of the Criz II Bridge, it was designed the strengthening of the shaft through jacketing with reinforced concrete, above the top of the pile cap. This reinforcement was necessary due to the high stresses in the existing shaft, resulting from local vibration modes associated with the high mass of the pier and water, which exceed their resistant capacity.

The reinforcement of pier basements located outside the reservoir was designed through external and internal jacketing with reinforced concrete, in order to protect these elements against water, and through prestress to confine and to able the load transfer between the pier and the new concrete element.

After finishing the new foundations and the piers jacketing, a set of works were foreseen to repair and reinforce the piers shafts and beam caps, including coating and an application of water-leaking impregnation.

Finally, was also designed the replacement of Criz II Bridge bearings, which included the construction of a new concrete element on the pier cap beams to support the deck during this work.

All solutions presented above allowed to preserve the abutments and deck rehabilitation and reinforcement solutions that were implemented in the first phase, presented in 4.1.

Monitoring during the works

Due the proximity execution of the new piles to the existing pier basements and foundations, and degradation of these elements, LNEC [7] developed a vibration monitoring system to reduce the dynamic impact of works on the piers and foundations, as also to prevent possible dynamic resonance phenomena resulting from the core drill works.

Thus, the implemented procedures above distinguished, allowed to conduct the structural reinforcement of the bridge piers, with a reliable degree of assurance to guarantee the safety of the workers, the road users as also the structures performance.

The monitoring procedure that was developed to assess the dynamic impact of the foundations and bridge piers structural reinforcement, had the following specific objectives:

- Establishing the vibration level limits induced by rock drilling equipment in order to mitigate the risk of increasing the bridge piers deterioration, based on dynamic response simulation models of the structures;
- Definition of procedures to demonstrate the equipment suitability to those vibration limits requirements;
- Assessment and implementation of construction process monitoring measures, as preliminary tests to evaluate the drilling process system, vibrations induced in the structures and observation of the cracking process development.

4.2.2.3 São João de Areias Bridge

The solution designed in this bridge is similar to the one developed to the Criz I and Criz II Bridges. The structural intervention was planned in the submerged areas of the piers below the reservoir top operation level.

This solution has been designed in order to create a redundant system that ensures the structural stability and good performance in service, if the internal swelling reactions continue to occur in the original concrete elements.

The P2 to P4 piers reinforcement consisted on the execution of a

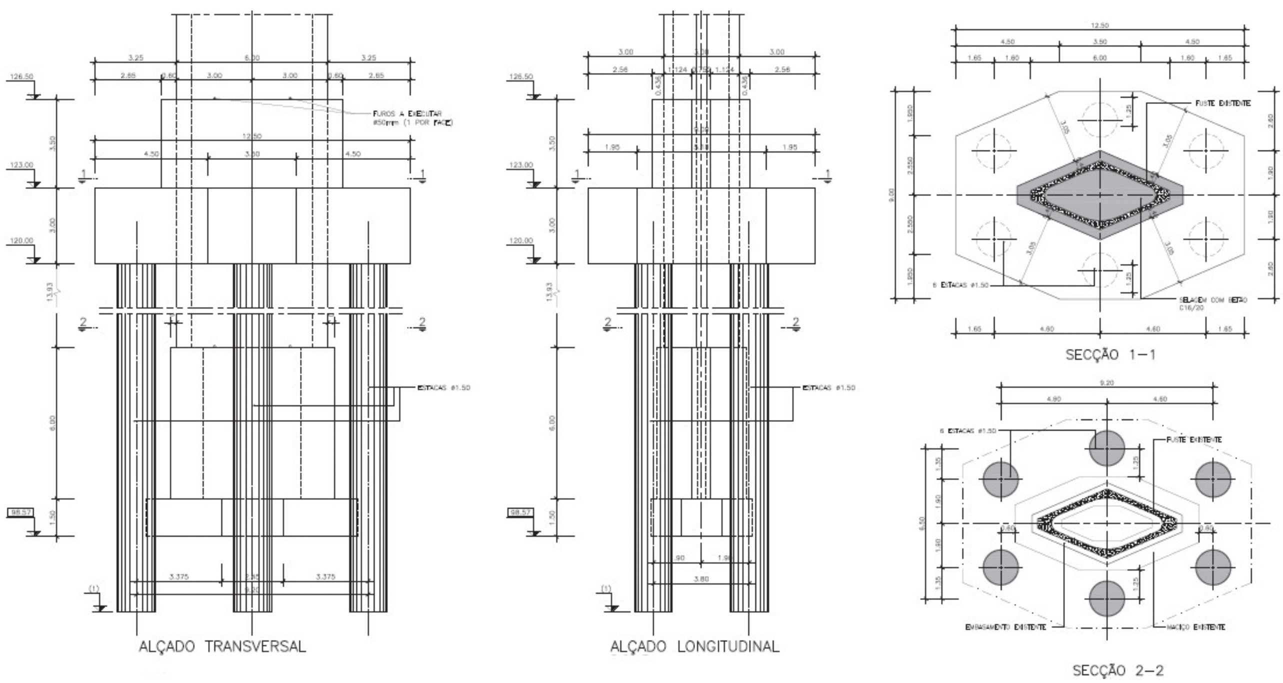

Figure 17 Solution type for the piers in the reservoir [4]

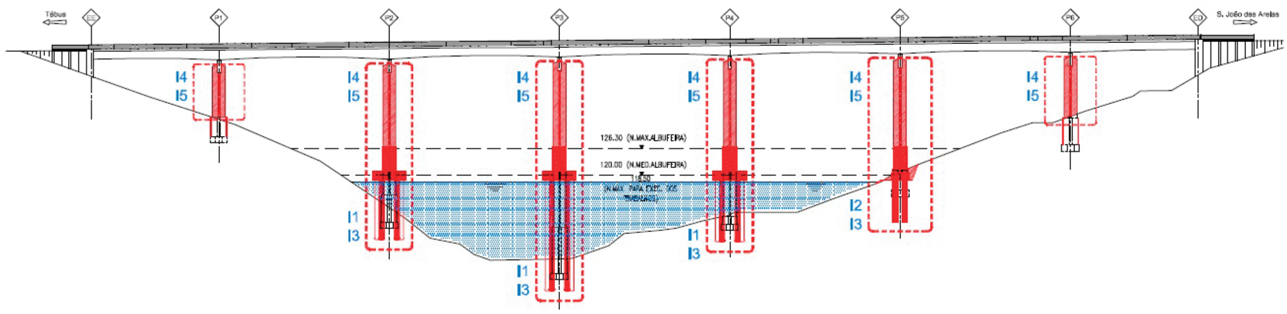

Figure 18 Intervention solution in the foundations of São João de Areias Bridge [5]

set of 6 piles, with ϕ1,20 m, embedding on the bed rock, around the piers, linked to it through a prestressed pile cap in reinforced concrete, where the load will be transferred from the pier shaft to the new foundation in case of deterioration of the existing ones.

In the case of P5 pier, near the river bank, the reinforcement solution was carried out with micropiles around the pier, linked to it through a prestressed pile cap in reinforced concrete with 1,50 m thickness, built at the same height as the others pile cap.

Thereby, it was carried out an external jacketing solution with reinforced concrete around the pier shaft between the upper face of the prestressed pile cap and the maximum level of the reservoir, plus 0,50 m, in order to protect these elements against water and to confine them as well.

Regarding P1 and P6 piers, a reinforcement concrete jacketing of 0,14 m thickness was applied on the outer perimeter of the basement, in order to avoid the contact of the concrete with the underground water.

After finishing the new foundations and the piers jacketing, a set of works were foreseen to repair and reinforce the piers shafts and cap beams, including coating and an application of water-leaking impregnation.

As in Criz II Bridge, due the proximity execution of the new piles to the existing pier basements and foundations, a vibration monitoring system was implemented.

4.2.2.4 Foz do Dão Bridge

The Foz do Dão Bridge piers reinforce and rehabilitation was found to be unfeasible during the intervention design development.

Currently, 3 of the 8 piers that support the deck structure have a permanently submerged height of more than 50 m (the P5 pier is 60 m height), making it very difficult to work at these depths. It is important to underline that the elements with more evident deteriorations, caused by the swelling reactions, are the pier basements, the elements at the bottom of the piers where the shaft becomes larger. Therefore, it wasn't possible to make any reinforcement solution along the piers height (like the ones of Cunhedo, Mortágua and Santa Comba Dão Bridges), once it wasn't possible to use technical and human means to execute correctly these kind of works at the mentioned depths. Another solution would be to execute the reinforcement by jacketing in half of each pier height, supported by a reinforced concrete pile cap located at the medium height of the reservoir, which in turn would be supported by a set of piles, executed with a tube, that would work like piers. This solution was also implemented on the Criz I, Criz II and São João de Areias bridge piers, and showed to be adequate where the reinforcement by jacketing along all the pier height is costly and complex because of the piers submerge height. However, given some of Foz do Rio Dão bridge foundations were very deep, it wasn't possible to guarantee the piles verticality, which makes this solution extremely complex and extremely difficult to perform.

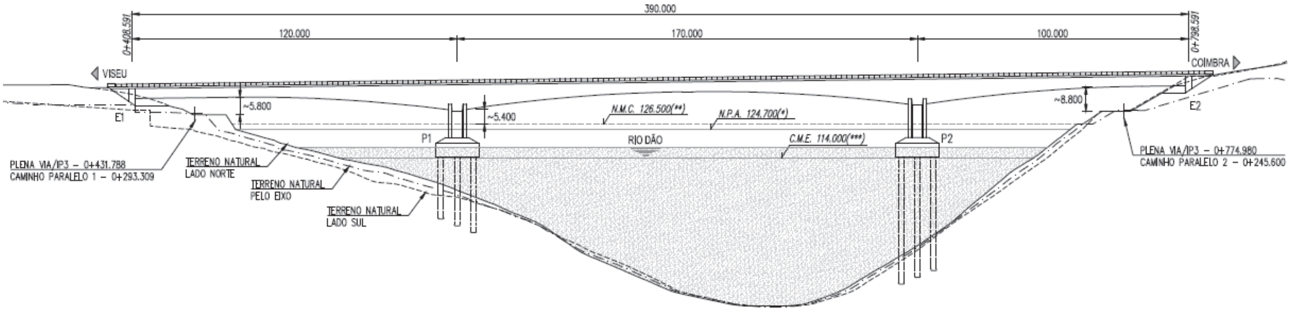

Figure 19 New Foz do Dão Bridge [8]

Thus, the studied solutions included the piers replacement or the full bridge replacement. At the end, the full bridge replacement was proved to be the better solution.

The new bridge deck has a 15 m wide platform, with 3 spans of 120 m + 170 m + 100 m length, performing a 390 m total bridge length.

The deck consists of a monocellular box girder with variable height cross-section, made of prestressed and reinforced concrete. It was cast-in-place using the balanced cantilever method.

The deck/piers connection is monolithic, while the deck is supported on the abutments through bearings.

The piers are made of prestressed reinforced concrete, which cross-section consisting of two parallel walls of constant geometry, with 5,80 m x 1,40 m envelope dimensions.

The pile cap heads a set of 9 piles, with 2 m diameter each, executed using a lost metallic tube, fixed in the bed rock.

Both abutments are made of reinforced concrete and consists on a bearing beam supported on footings, placed on top of jet-grouting columns.

Due to the necessity of using a guide metallic tube to execute the piles, their execution was particularly difficult because of the reservoir depth (30-40 m submerged) and the significant river bank slope. It´s also important to highlight that this was the first time in Portugal where submerged piles were executed at this depth.

5 Final considerations

The results of the inspections and tests performed on this set of bridges confirmed the existence of degradation process resulting from swelling reactions of the ASR and the DEF type. Given the implications on the resistant capacity of the structural elements, mainly piers and foundations, proven by the low value of the concrete compressive strength and elasticity modulus, Infraestruturas de Portugal, S.A., with the support of LNEC, outlined a strategy to rehabilitate and strengthening these bridges.

The design of piers and foundations strengthening was based on the assumption that was possible to maintain the decks, and that this approach was more competitive, in economic terms, than the integral replacement of the bridges. Indeed, during the project development was verified that the applied methodology was appropriate for 6 bridges. Only for the Foz do Dão Bridge was verified to be more advantageous, in technical and economic terms, the integral bridge replacement solution.

The intervention in these bridges consisted of a set of processes that allowed to maintain the bridges safety during the projects development until the structural safety levels reestablishment. For this purpose, specific emergency interventions were adopted over the years, which were not addressed in this paper, but allowed to maintain temporary structural safety levels for the most damaged elements, until the global intervention.

Despite specific evidence in some bridges throughout the country, whose punctual repair/reinforcement and monitoring has been effective, the intervention in the bridges of Aguieira's road network, due to its size, scope and cost, represented the first major challenge to Infraestruturas de Portugal, S.A. regarding to swelling reactions in concrete.

The total investment cost in these bridges, including studies, design, monitoring and execution, was about 33 M€.

References

[1] TRIEDE, 2010 – IP3 – Obras de Arte Inseridas na Rede Viária da Aguieira – Projeto de Reabilitação e Reforço Estrutural, Projeto de Execução

[2] PROFICO, 2011 – IP3 – Ponte sobre a Foz do Rio Dão – Substituição da Obra de Arte. Projeto de Execução

[3] PCA, 2011 – IP3 - Ponte sobre o Rio Mondego em Cunhedo - km 69+257 / Ponte sobre a Ribeira de Mortágua km 71+180 / Ponte sobre o Rio Dão em Santa Comba Dão km 84+400 - Reabilitação/ Substituição dos pilares das Obras de Arte. Projeto de Execução

[4] TRIEDE, 2014 – EN 234 – Pontes sobre o Rio Criz (I e II) – Reforço Estrutural de Pilares e Fundações, Projeto de Execução

[5] A2P, 2014 – Reabilitação dos Pilares da Ponte de S. João de Areias sobre o Rio Mondego, na EN234-6. Projeto de Execução

[6] Santos L, Xu M, Silva A (2021), Monitoring of ASR/ISR structural effects in Aguieira bridges. 16th International Conference on Alkali Aggregate Reaction in Concrete, Lisboa

[7] Costa A, Candeias P, Lemos J, Catarino M (2018), Análise da segurança de pontes sujeitas a ações dinâmicas em empreitadas de reabilitação dos pilares. RPEE Série III nº 8

[8] ARMANDO RITO, 2015 – IP3 – Ponte sobre a Foz do Rio Dão – Substituição da Obra de Arte. Projeto Variante – Projeto de Execução

Cimentar o Futuro

Roteiro da Indústria Cimenteira para a Neutralidade Carbónica 2050

O evento “Cimentar o Futuro” realiza-se no próximo dia 29 de março, das 10h00 às 12h00, em formato digital, devido às restrições causadas pela pandemia.

Aproveite esta oportunidade para conhecer o compromisso e alinhamento do Roteiro da Indústria Cimenteira para a Neutralidade Carbónica 2050 com as metas nacionais estabelecidas no RNC2050 e os princípios do Pacto Ecológico Europeu.

Organizada pela ATIC em conjunto com as suas Associadas, CIMPOR e SECIL, e em parceria mediática com o Expresso/SIC Notícias, a conferência conta com a presença de S. Ex.ª o Ministro de Estado, da Economia e da Transição Digital, de S. Ex.ª o Ministro do Ambiente e da Ação Climática, Deputados ao Parlamento Europeu, personalidades de renome e com experiência incontornável nestas matérias e executivos seniores da indústria do cimento.

Junte-se a nós rumo a um futuro sustentável.
Saiba mais em www.atic.pt

IABSE

International Association for
Bridge and Structural Engineering

IABSE Webinars

A IABSE promove em abril de 2021 dois Webminars, cuja inscrição é gratuita mas obrigatória.

Parametric Structural Design with Isogeometric Analysis
9 April 2021, 14-15 hrs (CET).
Speaker: Anna Bauer, structural engineer at Mayr Ludescher Partner.

Ultra-High-Performance-Concrete (UHPC)
30 April 2021, 14-15 hrs (CET).
Speaker: Lukas Vrablik, Associated professor CTU in Prague, Head of Department of Concrete and Masonry Structures; Technical director Valbek;

Informações e inscrições em:
https://iabse.org/Events/Calendar-of-Events/IABSE-Webinars

https://iabse.org/ghent2021

O Congresso da IABSE de 2021 terá lugar em Ghent, Bélgica, nos dias 22 a 24 de setembro de 2021, sendo uma organização conjunta dos Grupos belga e holandês da IABSE, em cooperação com a Universidade de Ghent.
O tema do Congresso é "Structural Engineering for Future Societal Needs", incluindo a construção e manutenção de edifícios e infra-estruturas seguras e fiáveis sob os efeitos das alterações climáticas num mundo com recursos mais escassos e com a ambição de reduzir a pegada de CO2 da Humanidade. As futuras necessidades societais podem ser divididas em duas partes, "Segurança estrutural e fiabilidade no que respeita às alterações climáticas" e "Circularidade, reutilização e sustentabilidade das estruturas". A maioria das apresentações do congresso irá cobrir estes dois subtemas em sessões normais de apresentação, sessões de posters, sessões de discussão, uma sessão Pecha Kucha e sessões especiais.
Foram submetidas cerca de 250 comunicações, atualmente em apreciação pela Comissão Científica deste evento.

fib Symposium 2021

The *fib* Symposium 2021 will be held online, from the 14th to the 16th of June 2021, gathering together professionals, researchers and students from all over the world to discuss 'Concrete Structures: New Trends for Eco-Efficiency and Performance'.

On the day before the symposium, there will be a keynote lecture addressing the maintenance of Vasco da Gama bridge by Julio Appleton and followed by a virtual technical visit to the structure. During the event, key-note speakers will address the three most relevant topics: *fib* Model Code 2020 by Stuart Matthews, sustainable concrete (recycled aggregates concrete) by Jorge de Brito, and high-performance structures (1 km tall Jeddah Tower) by Robert Sinn. Furthermore, the latest scientific and technological innovations and the most impressive projects in structural concrete will be presented.

The *fib* YMG is organizing an innovative session and group meetings. A students' competition will take place, addressing the double challenge of optimizing concrete's carbon footprint and performance for a specific structural application. The most relevant companies from the concrete construction industry will exhibit their products at symposium's online platform.

Lisbon is a breath-taking city with thousands of years of history and was considered the Worlds' Leading City Break Destination in 2019. Moreover, it is surrounded by astonishing magical places nearby, such as Cascais and Sintra. The symposium will have socializing moments where this atmosphere will be felt through music and image.

Main Topics:

Topic 1
Trend-setting projects
Topic 2
Materials – eco-efficiency and performance
Topic 3
Structural behaviour – new on-site and precast solutions
Topic 4
Analysis and Design – advanced methods and innovative approaches

Important Dates and Deadlines

Submission of abstracts
CLOSED
Notification of abstract acceptance
CLOSED
Submission of full paper
CLOSED
Notification of paper acceptance
31st March 2021
***fib* Symposium**
14th-16th June 2021

Program and Registration

More detailed information can be found on the symposium website:
www.fiblisbon2021.pt

Venue

The conference will take place at LNEC – National Laboratory for Civil Engineering.
www.lnec.pt

Symposium Secretariat

Av. do Brasil, 101, 1700-066 Lisboa – PORTUGAL
E-mail: info@fiblisbon2021.pt
www.fiblisbon2021.pt

A SPES

A SPES, é uma associação de carácter cultural e científico de pessoas individuais e colectivas, com os seguintes objectivos:

a) Fomentar, em Portugal, o desenvolvimento da Engenharia Sísmica, Sismologia e Prevenção e Defesa contra os Sismos, promovendo a divulgação da informação, o intercâmbio científico e técnico entre os seus associados e a organização de reuniões, colóquios e conferências ou outras iniciativas de carácter análogo.

b) Assegurar a representação Portuguesa nas Associações Europeia e Internacional de Engenharia Sísmica (EAEE e IAEE).

INICIATIVAS 2016 - 2018

- Prémio Carlos Sousa Oliveira, destinado a premiar o melhor trabalho na área da Sismologia e Engenharia Sísmica
- Realização do 11º Congresso Nacional de Sismologia e Engenharia Sísmica, Lisboa, 2018
- Candidatura à organização da 17º Conferência Europeia de Engenharia Sísmica
- Estudo de procedimentos com vista à futura certificação sísmica de edifícios existentes
- Estudo relativo à análise das Zonas Sísmicas e respetivos parâmetros, para Portugal Continental: comparação das várias propostas e implicações para a perigosidade sísmica
- Realização dos seminários de verão SPES, em parceria com Pretensa e LNEC
- Realização de workshops em parceria com a ordem dos Arquitetos, ordem dos Engenheiros e LNEC

HISTÓRIA

A Engenharia Sísmica teve o seu início, em Portugal, após o sismo de 1 de Novembro de 1755, uma vez que na reconstrução da cidade de Lisboa foram utilizados sistemas estruturais e construtivos que garantiam segurança acrescida em relação às acções sísmicas (edifícios pombalinos).

O desenvolvimento, em Portugal, da Engenharia Sísmica moderna, com base em critérios científicos, remonta à década de 50, impulsionado pelo Eng. Júlio Ferry Borges que, em 1958, e após a realização do Simpósio sobre os Efeitos dos Sismos e a sua Consideração no Dimensionamento das Construções, participou na redacção do primeiro código de construção anti sísmica em Portugal, o Regulamento de Segurança das Construções Contra os Sismos.

A Sociedade Portuguesa de Engenharia Sísmica, SPES, foi criada em 1973 com o apoio do Laboratório Nacional de Engenharia Civil, LNEC, e do Instituto Nacional de Meteorologia e Geofísica, na continuidade do Grupo Português de Engenharia Sísmica que já cumpria, embora informalmente, os objectivos estatutários da SPES.

Hoje a SPES acolhe todos os que, das diferentes áreas do conhecimento, se preocupam com a tarefa de minimização do risco sísmico, colocando a ciência e a técnica ao serviço desse objectivo ético.

SER SÓCIO SPES

- Usufruir de descontos no valor da inscrição em eventos organizados pela SPES
- Receber as newsletters da SPES por correio electrónico
- Aceder a biblioteca de recursos privilegiados na área da Sismologia e da Engenharia Sísmica
- Concorrer ao Prémio Carlos Sousa Oliveira
- Participar em fóruns de discussão de assuntos de interesse nacional na área da Sismologia e da Engenharia Sísmica

SOCIEDADE PORTUGUESA DE ENGENHARIA SÍSMICA

Av. do Brasil, 101
1700-066 Lisboa • Portugal
Tel. (+351) 21 844 32 91
spes@lnec.pt
http://spes-sismica.pt/


SISTEMA DE
REPARAÇÃO DE BETÃO
GEOACTIVE
TOP B 525
VANTAGENS
• Fibrorreforçado
• Tixotrópico
• Resistente aos sulfatos
• Retração compensada
• Excelente resistência mecânica
GEOACTIVE
TOP B 525
FASSA
BORTOLO
FASSA
BORTOLO
QUALIDADE PARA CONSTRUÇÃO

COM O APOIO DE:

apfac
associação portuguesa
dos fabricantes de argamassas e etics

ARMANDO RITO
ENGENHARIA

ATIC
ASSOCIAÇÃO TÉCNICA DA
INDÚSTRIA DE CIMENTO

Betar
CONSULTORES

CACAO
CIVIL ENGINEERING

FASSA
BORTOLO
QUALIDADE PARA CONSTRUÇÃO

HILTI

INSTITUTO DA
CONSTRUÇÃO

PRETENSA

http://rpee.lnec.pt/

ISSN 2183-8488
9 772183 848007 30015

AV DO BRASIL 101 • 1700-066 LISBOA • PORTUGAL
tel. (+351) 21 844 30 00 • fax (+351) 21 844 30 11
lnec@lnec.pt www.lnec.pt